PSFC/RR-03-3 **DOE-ET-54512-346**

Experimental Investigation of Toroidal Rotation Profiles in the Alcator C-Mod Tokamak

W. Davis Lee

April 2003

Plasma Science and Fusion Center
Massachusetts Institute of Technology
Cambridge, MA 02139 USA

This work was supported by the U.S. Department of Energy, Cooperative Grant No. DE-FC02-99ER54512. Reproduction, translation, publication, use and disposal, in whole or in part, by or for the United States government is permitted.

Experimental Investigation of Toroidal Rotation Profiles in the Alcator C-Mod Tokamak

by

William Davis Lee

B.S. Physics, Mathematics, Mary Washington College (1998)
M.S. Applied Physics, Johns Hopkins University (2002)

Submitted to the Department of Nuclear Engineering in
Partial Fulfillment of the Requirements of the Degree of

Doctor of Philosophy in Nuclear Science and Engineering

at the

Massachusetts Institute of Technology

14 April 2003

Author: _____

W. D. Lee
Department of Nuclear Engineering

Certified by: _____

Dr. J. E. Rice
Thesis Supervisor

Approved by: _____

Prof. I. H. Hutchinson
Thesis Reader

Accepted by: _____

Prof. J. A. Coderre
Chairman of Graduate Committee

Experimental Investigation of Toroidal Rotation Profiles in the Alcator C-Mod Tokamak

by

William Davis Lee

Submitted to the Department of Nuclear Engineering
on 14 April 2003, in partial fulfillment of the
requirements for the degree of
Doctor of Philosophy in Nuclear Science and Engineering

Abstract

A multi-chord, tangentially viewing, vertically displaced, high resolution x–ray spectrometer array has been adapted to the Alcator C–Mod tokamak for the purpose of measuring the impurity rotation profile, in momentum source free plasmas. The 3 spectrometers have used Doppler shifted x–rays to measure the toroidal rotation velocity. Data taken during Ohmic discharges indicate flat rotation profiles, in both L–mode and H–mode; with velocities of $\sim -10\ km/s$ in L–mode and $\sim 35\ km/s$ in H–mode. The source of this momentum is at the plasma edge, with momentum diffusion causing the center to rotate. By solving a simple diffusion equation, and fitting the implied profiles to the data, diffusion coefficients ($D_{\phi,H} \sim 0.100\ m^2/s$, $D_{\phi,L} \sim 0.250\ m^2/s$) and momentum time scales ($\tau_{\phi,H} \sim 0.080\ s$, $\tau_{\phi,L} \sim 0.030\ s \simeq \tau_E$) have been simulated. Data taken during ICRF discharges have shown many different co–current profile shapes. Flat, co–current rotation profiles have been measured and linked to EDA H–modes and momentum diffusion. The confinement times and momentum diffusion coefficients have been found to be similar to those of both the Ohmic case and for impurity particles. Peaked rotation profiles have been measured and linked to ELM free H–modes and to diffusion and inward convection of momentum. The confinement times ($\tau_{\phi,H} \sim 0.070\ s$), momentum diffusion coefficients ($D_{\phi,H} \sim 0.400\ m^2/s$) and convection velocities ($v_c \sim 12\ m/s$), have been simulated with another simple model. Data taken during ITB discharges have shown rotation profiles that evolve from flat co–current to hollow, with rotation slightly counter–current inside the barrier foot. Radial electric field profiles have been infered using neoclassical theory; these profiles are found to be highly sheared around the barrier foot. A lower limit to the gradient of the radial electric field ($\partial E_r/\partial r$) of $\sim 183\ \mathrm{kV/m^2}$ has been set, and a lower limit on the shearing frequency has been approximated as $\omega_E \simeq 38\ krad/s$.

Acknowledgments

This work would not have been possible were it not for the help and assistance of quite a few people. First and foremost, I would like to thank Dr. John Rice for his supervision throughout this endeavor. His effort in helping me to do this work and produce this document has been nothing short of heroic. He has been patient, persistent, diligent, speedy, kind and always available for any reason, in any matter. Moreover, he has been my friend overflowing with encouragement and support, without him I would be alone in a metaphorical dinghy, adrift at dawn.

I have to thank Prof. Ian Hutchinson for his advice and council throughout my years here at MIT, and specifically for reading my thesis. I wish to express my appreciation to Prof. Miklos Porkolab for his input and direction on quite a few projects. I would like to thank Dr. Earl Marmar for sitting on my thesis commitee, for his help, advice and general good cheer, and for many interesting and stimulating conversations. I would like to express my gratitude to the other members of my thesis committee: Prof. Ron Parker and Prof. Jeff Friedberg. I would like to acknowledge the faculty of the department of Nuclear Engineering, for giving me the opportunity to do this research. I would like to thank Dr. Steve Wukitch, with whom I started my graduate career, for all his help, support and patience.

I also need to recognize all the engineers, technicians and research scientists that have helped me build, design, draw, machine, weld, test, measure, prepare, revise, compute, order... In no particular order: Paul Bonoli, Jim Terry, John Goetz, Jim Irby, Ed Fitzgerald, Amanda Hubbard, Steve Wolfe, Bill Beck, Rui Vieira, Bob Childs, Clare Egan, Dave Arsenault, Ned Eisner, Tim Davis, Dragana Zubčevič, Martin Greenwald, Henry Bergler, Steve Tambini, Dexter Beals, Rich Danforth, Sergey Andreyev, Brian Labombard, Charlie Cauley, Joe Bosco, Tom Fredian, Yuri Rokhman, Bob Sylvia, Mark London, Eric Anderson, Mark Iverson, Sam Pierson, Ambrogio Fasoli, Bill Cochran, Catherine Fiore, Andy Pfeifer, Dimitri Mossessian, Robert Granetz, Maria Silveira, Gerd Shilling, Kelly Johnson, Wanda Pina, Willy Burke, Liz Parmelee, Stuart Sherman, Dave Belloffato, Rick Murray, Ron Rosati,

Jerry Gerolamo, Henry Savelli, Josh Stillerman, Don Nelson, Jack Nickerson, Valerie Censabella and Rejean Boivin. Last, but certainly not least Tom Toland, to whom I shall always be in debt, for help, favors and advice far above and beyond the call of duty.

I must thank Frank Silva and Jim Rosati, both of whom indulged most of my whims and fancies, regardless of how seemingly absurd.

My fellow graduate students, many of whom have already gone on to great things: Jim Reardon, Thomas Pedersen, Alex Mazurenko, Eric Nelson-Melby, Jerry Hughes, Natalia Krasheninnikova, Jagdishwar Sirigiri, Dave Schmitdiel, Ken Marr, Tim Graves, Taekyun Chung, Steve Korbly, Yijun Lin, Mark Hess, Howard Yuh, Chris Boswell, Alex Parisot, Tom Jennings, Justin Sarlesse, Vincent Chang, John Liptac, Brian Youngblood, and finally Rob Nachtrieb and Sanjay Gangadhara who together convinced me to come to MIT in the first place.

Finally, I owe a great deal to my Madeleine who has always been supportive, and patient, with my unorthodox hours and often obsessive work schedule. And, of course, my family; my parents and my grandmother who have given me just about every opportunity a person could hope for; my sister and brother who have been supportive enthusiasts throughout this and most other experiences I have had.

"If life hands you lemons, make lemonade.
If life hands you limes, make a gimlet."

Contents

List of Figures

List of Tables

Chapter 1

Introduction

Alcator C–Mod[1] is a compact high density, high field tokamak, operating at the Massachusetts Institute of Technology's Plasma Science and Fusion Center, generously funded by the United States Department of Energy. C–Mod is one of the world's premier fusion experiments.

1.1 Background

1.1.1 Confinement

Fusion engineers' ability to confine reactor grade plasmas adequately is the single most important goal of present fusion research. Reduction of the underlying transport processes which cause energy and particle losses is a major thrust in the tokamak research. Thus, the formation and sustainment of transport barriers is a topic of great interest.

Transport barriers generally lead to steep gradients in density, temperature or pressure. Presently the two most common types of transport barriers are the high confinement mode (H–mode) edge barriers and internal transport barriers (ITBs). The H–mode is essentially an edge phenomenon that reduces both outward particle and energy transport, leading to a very steep pressure gradient just inside the separatrix, or last closed flux surface (LCFS). The ITB is a similar reduction in particle

and energy transport at a location in the core of the plasma[2, 3]. These transport barriers represent improved confinement modes of plasma operation, and thus are of great interest to the fusion community.

1.1.2 Rotation and Radial Electric Field

Improved plasma confinement in either the H–mode or the ITB regime is linked to plasma rotation and the radial electric field. In fact confinement and transport of energy, particles and momentum are all related. Thus, to understand rotation and momentum more completely leads to a better understanding of improved plasma confinement.

Toroidal rotation and the radial electric field are inextricably linked, (some theories are presented in Chapter 2). The question of whether the rotation is required to induce the electric field, or the electric field induces the rotation has not and arguably can not be answered[1]. The presence of one requires the other as a consequence of the radial force balance.

The ability to measure the rotation velocity directly, and comparative inability to measure the radial electric field directly[2] makes the rotation velocity the natural quantity to pursue.

1.1.3 Source Free Measurements

Machines heated with neutral beam injection (NBI), use beams of high energy neutralized atoms (generally H or some isotope thereof) to heat (and fuel) the plasma. A consequence of this heating is the introduction of momentum into the plasma. That is, the beams, generally orders of magnitude higher energy than the bulk plasma, represent a tremendous momentum source.

While interesting to measure, the rotation induced by the heating beams can

[1] A more pedestrian way of seeing this would be to analogize this question to that of the chicken and the egg. Which came first...

[2] The radial electric field can be measured directly with heavy ion beam probes, which C–Mod does not have.

possibly obscure the underlying physics of rotation in magnetically confined plasmas. On many machines the required conditions for improved confinement operation, a regime of great interest, include heating beams. It is therefore highly desirable to find a method of measuring plasma rotation in a source–free, improved confinement mode of operation, in an effort to understand the underlying physics.

Attempts to measure purely plasma rotation effects in beam heated tokamaks fall in three categories: balanced beam operation, perpendicular beam operation and the removal of beam effects via data reduction, (previous results are presented in Chapter 3). All three of these techniques present difficulties. Balanced beam operation heats the plasma with "equal" amounts of beam power injected in each direction. This leads to large uncertainties, and due to the high energy of the beams, very small misalignments or differences in launched beam power could lead to large momentum inputs. Similar problems are encountered with perpendicular beams. Moreover, perpendicular beams can lead to a radial electric field and thereby a toroidal rotation velocity. Removal of beam effects via data reduction has a different set of problems. This technique requires that the precise values of the beam power and flux, the neutral density profile, and the plasma temperature and density be well known. Uncertainties associated with these quantities leave the results of this method sketchy. Moreover, measurements of this type and their associated calculations don't allow for the possibility of some spontaneous plasma rotation. This creates a problem because H–mode plasmas *do* spontaneously rotate and generally in a non-negligible fashion[3].

Source free measurements can be made in beam heated plasmas, by running the NBI then shutting it off and measuring the rotation decay time. When the beams are turned off, the plasma goes back to L–mode and the L–mode momentum confinement time, ($\tau_{\phi L}$), is measured. However, this method does not allow the H–mode momentum confinement time, ($\tau_{\phi H}$), to be measured with good accuracy or high precision. In C–Mod, due to the high densities, the x–ray photon counting rates are generally high enough to measure both the rise time and the decay time, in and out of H–mode, even during Ohmic plasmas.

[3]L–mode plasmas also rotate, but generally much less.

1.1.4 Motivation

C–Mod is a momentum–source–free tokamak. The option to use NBI is not available. High confinement modes can be achieved either through Ohmic methods or by Ion Cyclotron Resonance Heating (ICRH).

Previous measurements of the toroidal rotation profile in C–Mod were performed with spectrometers having very small toroidal view angles. The small angle of view meant the toroidal rotation velocity profile had high uncertainty at best. The uncertainty in these measurements has left the radial electric field profile in the plasma highly uncertain as well.

In other machines with neutral beams, and neutral beam based diagnostics, measuring the profiles of plasma parameters, is technologically simpler. Rotation measurements made with beams use impurity line radiation generally in the visible region of the spectrum; a great deal of technology has been developed to facilitate measurements in this range of wavelengths. C–Mod does not have high current beams and the associated beam based diagnostics[4]. Therefore, obtaining profiles of plasma parameters must be done by other means.

Although the measurements may be less complete without all the beam based diagnostics, C–Mod is an ideal tokamak on which to perform rotation and momentum experiments. High density correlates to improved x-ray signal strength; and by using only radio frequency and Ohmic heating methods, the machine is momentum–source–free.

1.2 Goals

There are two main goals in this investigation: first, to contribute to understanding why H–mode plasmas in C–Mod rotate at all. Second, to generally characterize momentum transport, (χ_ϕ and $v_{c,\phi}$,) the momentum diffusivity and the momentum convection velocity. Specifically, to understand χ_ϕ the momentum transport coefficient,

[4]In any case, the very high densities in C–Mod prohibit great depth of beam penetration, thus some other means of diagnosis is required.

and its apparent relation to χ_i, the heat transport coefficient and D the particle diffusion coefficient. This work represents a new measurement in a momentum–source–free tokamak, namely profile measurements of both the rise and decay times of toroidal rotation, following the H–mode transition.

1.3 Outline

This thesis is presented in eight chapters and four appendices. Chapter 1 is the introduction. Chapter 2 outlines some of the current theories that are either used in this thesis or relevant to toroidal rotation measurements and momentum confinement. Chapter 3 gives an account of previous measurements of toroidal rotation on C–Mod and other tokamaks. The previous results are divided into categories based on the type of diagnostic and the machine on which it was made. Chapter 4 describes the experimental setup, the spectrometer, its components and the associated physics. Chapter 5 presents some of the data taken with the spectrometer during Ohmic discharges, and some theory to interpret the measurements. Chapter 6 presents data taken during ICRF heated discharges and some interpretation of these data. Chapter 7 concerns data taken during ITB discharges, and presents some modeling of these data. In the last chapter, Chapter 8, conclusions are drawn and possible directions of future work are discussed. Appendix A is a detailed calculation of the expected line intensities of He–like Ar. Appendix B is a calculation of rate coefficients for the dominant line population mechanisms. Appendix C is a calculation of the fractional abundance of argon charge states in coronal equilibrium. Finally, Appendix D has some calculations of x–ray attenuation in air and beryllium.

1.4 The Alcator C–Mod Tokamak

Alcator C–Mod, the machine, is a compact high field, high density tokamak[5], that has been in operation since 1993[1]. Figure 1-1 is a cross–section of C–Mod; many of

[5]For much more information on tokamaks in general see ref. [4–7]

the important components have been labeled. Table 1.1 has some of the important parameters relevant for Alcator C–Mod. Alcator C–Mod usually runs with a deuterium majority plasma therefore the fusion reactions of interest are the D (D T) p reaction (Eq. 1.1), and the D (D ^{3}He) n reaction (Eq. 1.2).

$$^2D +^2 D \rightarrow^3 T +^1 H + 4.03MeV \tag{1.1}$$

$$^2D +^2 D \rightarrow^3 He +^1 n + 3.27MeV \tag{1.2}$$

C–Mod is run with a minority species, generally H, (although sometimes ^{3}He). This minority is used generally to allow the Ion Cyclotron Range of Frequencies (ICRF) auxiliary heating.

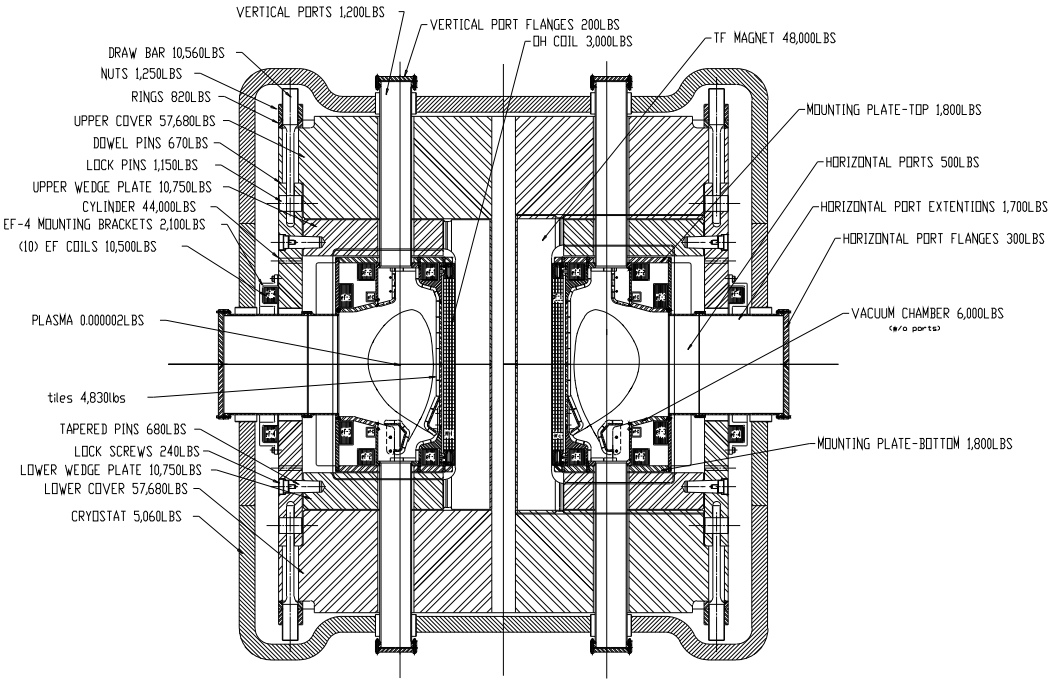

Figure 1-1: A cross–section of the Alcator C–Mod tokamak, from the original plans. Many components have been labeled and their weights listed.

What separates C–Mod from most tokamaks is its extremely high particle densities, magnetic fields and RF power densities, (see Table 1.1). Further, C-Mod currently has exclusively ICRF auxiliary heating power. By late 2003 C–Mod will

Parameter	Symbol	Range or Value	Units
Toroidal Magnetic Field	B_T	3.0 – 8.0	Tesla (T)
Plasma Current	I_P	0.4 – 2.0	Mega-Amps (MA)
Major Radius	R	0.68	meters (m)
Minor Radius	a	0.22	meters (m)
Central Density	n_e	0.5×10^{20} – 2.0×10^{21}	per cubic meter (m^{-3})
Central Temperature	T_e	0.5 – 5.0	kilo-electron Volts (keV)
Elongation	κ	0.9 – 1.8	
Triangularity	δ	$\sim$ 0.1 – 0.85	
RF Power	P_{RF}	0 – 6	Mega-Watts (MW)
Plasma Volume		$\sim$ 1.0	m^3
Operating Period		1993 –	Year of our Lord (AD)

Table 1.1: Some of the relevant parameters for the Alcator C–Mod tokamak.

start to add Lower Hybrid wave launchers for current drive and plasma heating.

C–Mod has host of diagnostics summarized in Table 1.2. The table has been set up to display the various plasma parameters and then list the diagnostics that make those measurements. For more thorough coverage of the details of these and other diagnostics, see the following sources [4, 7–13]

1.5 Units

Unless specifically noted otherwise all units in this thesis are in the *System International*, SI or MKS. There will be a few places where CGS units are used, and a few places where the ghastly English units are used, these should be obvious.

Measurement	Symbol	Diagnostic	region
Electron Density	n_e	Edge Thompson Scattering	edge
		Core Thompson Scattering	core
		Reflectometer	edge
		Langmuir Probes	SOL
		Plunging Probes	SOL
		TCI	core
		High Resolution Z - Meter	core & edge
Density Fluctuations	$\tilde{n}_e$	PCI	edge
		BES	edge
		Reflectometer	edge
Impurity Density	n_I	HIREX	core
		Chromex	edge
		MCP	core & edge
Distribution Function	$f(\mathbf{x}, \mathbf{v}, t)$	Langmuir Probes	SOL
		ECE	core
		NPA	core
Electron Temperature	T_e	Edge Thompson Scattering	edge
		Core Thompson Scattering	core
		HIREX	core
		GPC	core & edge
		Langmuir Probes	SOL
		Plunging Probes	SOL
Ion Temperature	T_i	HIREX	core
		Neutrons	central only
		CXRS	edge
Toroidal Plasma Rotation	V_ϕ	THIREX	core
		Edge Magnetics	$q = 1$ Surf.
		CXRS	edge
		Edge Plumes	edge & SOL
Poloidal Plasma Rotation	V_θ	HIREX	core
		Edge Magnetics	edge
		CXRS	edge
H to D ratio	H/D	H_α and D_α spectroscopy	edge
		NPA	core

Measurement	Symbol	Diagnostic	region
q – profile	$q(r)$	MSE Li Pellet Injection	edge edge & core
Effective Charge	Z_{eff}	Z – meter	edge & core
Plasma Current	I_p	Rogowski Coils	
Toroidal Magnetic Field	B_T	Magnetic Coils	
Poloidal Magnetic Field	B_P	E-FIT	
Magnetic Fluctuations	$\hat{B}$	Loops Loop Probe	edge
Loop Voltage	V_ℓ	Voltage Loops	
Total Radiated Power	P_{rad} P_{rad} (2-D)	2-π Bolometer Bolo Arrays	 core & edge

Table 1.2: This is a comprehensive list of the diagnostics on C–Mod sorted by the measurement they make, (continued from page 26).

(This page intentionally left blank.)

Chapter 2

Rotation Theory

In this chapter some of the theories of plasma rotation will be discussed. It has six main parts: neoclassical theory, revisited neoclassical theory, subneoclassical theory, ICRF induced rotation, spontaneous rotation and finally, a brief discussion of the theory of internal transport barriers (ITBs). Due to the number and magnitude of the theories presented in this chapter, only the most salient points will be discussed. The most effort has been given to neoclassical theory, because it is the most well established, and the most fundamental of all the theories presented here. The other theories discussed here are relevant in the sense that they attempt to explain observations under conditions where neoclassical theory is not valid. A final goal of this chapter is to simply present some of the many theories and approaches that exist to explain or attempt to explain plasma rotation. Comparison between some of these theories and data will be presented in later chapters, (Chapters 5 & 6). One looking for more detail is encouraged to investigate the many references cited in this chapter[14–48].

In a source free tokamak, the plasma can start to rotate in essentially one (or a combination) of four ways. First and foremost, by design, a tokamak induces a current that is carried by the electrons and generates the poloidal Magnetic field. Conservation of momentum requires the ions to balance the electrons momentum by rotating in the opposite direction. Second, rotation can be generated by a pressure gradient as will be shown by neoclassical theory. Thirdly, an electric field can be set

up in the plasma, again more will be said about this in the discussion of neoclassical theory. Finally, momentum can originate outside the plasma and be diffused or convected inward.

2.1 Neoclassical Theory

The two standard presentations of neoclassical theory are the kinetic approach by Hinton and Hazeltine[14] and the moment approach by Hirshman and Sigmar[15]. In this thesis the presentation of neoclassical theory will follow the moment approach, as presented by S. P. Hirshman and D. J. Sigmar[15]. In this section this theory, and its relevance to the situation in Alcator and impurity rotation, will be reviewed, following Hirshman and Sigmar[15] and Kim, Diamond and Groebner[16].

2.1.1 Moment Approach

The expressions for the neoclassical poloidal and toroidal rotation velocities are found from the equilibrium parallel momentum and heat flow balance equations, for one majority ion and one impurity ion species. Starting with the Vlasov Fokker–Planck equation, relations for various transport coefficients are derived from the moment equations that arise from the the first two odd moments, $\int \vec{v} f(\vec{v}) dv$ the force balance equation and $\int v^2 \vec{v} f(\vec{v}) dv$ the heat flow balance equation. This has been done in rigorous detail in Hirshman and Sigmar[15].

2.1.2 Rotation Velocities

If the effects of ion orbit shifts and the individual charge states are neglected, as in Eqs. (33), (34), (56) and (57) of Ref. [16] (equivalently in Ref. [17]), it is found:

$$V_\phi^I = \frac{1}{B_\theta}\left[E_r + \frac{(K_1 + \frac{3}{2}K_2 - 1)}{e}\frac{\partial}{\partial r}T_i - \frac{T_i}{e n_i}\frac{\partial}{\partial r}n_i\right] \tag{2.1}$$

$$V_\phi^i = \frac{1}{B_\theta}\left[E_r + \frac{(K_1 - 1)}{e}\frac{\partial}{\partial r}T_i - \frac{T_i}{e n_i}\frac{\partial}{\partial r}n_i\right] \tag{2.2}$$

$$V_\theta^I = \frac{1}{B_\phi}\left[\frac{(K_1 + \frac{3}{2}K_2 - 1)}{e}\frac{\partial}{\partial r}T_i - \frac{T_i}{en_i}\frac{\partial}{\partial r}n_i + \frac{T_i}{Z_I e n_I}\frac{\partial}{\partial r}n_I\right] \tag{2.3}$$

$$V_\theta^i = \frac{1}{B_\phi}\frac{K_1}{e}\frac{\partial T_i}{\partial r} \tag{2.4}$$

where: B_ϕ is the toroidal magnetic field, B_θ is the poloidal magnetic field, T_k is the temperature for ion k, n_k is the density for ion k, $k = I$, i denote the impurity ion and the majority ion species respectively, e is the charge of the electron, Z_k is the charge of the ion k, E_r is the radial component of the electric field and K_1 and K_2 are viscosity matrix coefficients, (given by Eqs. 2.5 and 2.6 respectively). These four equations are the neoclassical poloidal and toroidal rotation velocities for both the majority ion and the impurity ion species.

2.1.3 Viscosity Matrix Coefficients

Through the moment approach the matrix solution leads to the coefficients K_i ($i =$ 1, 2). These are required to calculate the toroidal and poloidal rotation velocities. A full derivation of these K_i's can be found in Ref. [16]. The coefficients K_i are given by:

$$K_1 \equiv D^{-1}\mu_{01}^i(\sqrt{2} + \alpha - \alpha\beta) \tag{2.5}$$

$$K_2 \equiv D^{-1}[\mu_{00}^i\mu_{11}^i - (\mu_{01}^i)^2] \tag{2.6}$$

where:

$$D \equiv \mu_{00}^i(\mu_{11}^i + \sqrt{2} + \alpha - \alpha\beta) - (\mu_{01}^i)^2 \tag{2.7}$$

$$\alpha \equiv \frac{n_I Z_I^2}{n_i Z_i^2} \tag{2.8}$$

$$\beta \equiv \left(\frac{27}{4}\right)^2 \left(\frac{m_i}{m_I}\right)^2 \left(\frac{15}{2} + \sqrt{2\alpha}\frac{v_{T_i}}{v_{T_I}}\right)^{-1} \tag{2.9}$$

where: m_k is the mass of ion k, eZ_k is the charge of the ion k and v_{T_k} is the thermal velocity of ion k, ($k = I$, i). A general relation for these μ_{ij}^a's, valid over a wide range of regimes, is given in Ref. [16]. For μ_{00} and μ_{11}:

$$\mu_{ii} = \frac{g\hat{\mu}_{ii}^B}{(1 + 2.92\nu_{*a}\hat{\mu}_{ii}^B/\hat{\mu}_{ii}^P)[1 + \hat{\mu}_{ii}^P/(6\omega_{ta}\tau_{aa}\hat{\mu}_{ii}^{PS})]} \tag{2.10}$$

and for $\mu_{01} = \mu_{10}$:

$$\mu_{01} = \frac{5}{2}\mu_{00} - K_{01} \tag{2.11}$$

where:

$$K_{01} = \frac{g\hat{K}_{01}^B}{(1 + 2.92\nu_{*a}\hat{K}_{01}^B/\hat{K}_{01}^P)[1 + \hat{K}_{01}^P/(6\omega_{ta}\tau_{aa}\hat{K}_{01}^{PS})]} \tag{2.12}$$

and:

$$\nu_{*a} = \frac{g}{1.46}\frac{\omega_{ta}}{v_{T_a}^2\tau_{ta}}\frac{\langle B^2\rangle}{2\langle(\mathbf{b}\cdot\nabla\mathbf{B})^2\rangle} \tag{2.13}$$

$$\omega_{ta} = \frac{v_{T_a}}{R_0 q}. \tag{2.14}$$

$\langle B^2\rangle$ is the average of the square of the magnetic field, $\mathbf{b}$ is the unit vector in the direction of the magnetic field, $\mathbf{B}$ is the vector magnetic field, R_0 is the major radius and q is the safety factor. In Eqs. 2.10 – 2.13 above, τ_{ab} is given by:

$$\frac{1}{\tau_{ab}} = \frac{4}{3\sqrt{\pi}}\frac{4\pi n_b e^4 Z_a^2 Z_b^2 \ln\Lambda}{m_a^2 v_{Ta}^3}. \tag{2.15}$$

The $\hat{\mu}_{ii}^B$, $\hat{\mu}_{ij}^P$, $\hat{K}_{01}^{PS}$, *etc.* are given in Table 1 from Ref. [16], reproduced here as Table 2.1.

Collisionality	Banana Reg.	Plateau Reg.	Pfirsch–Schlüter Reg.
$\hat{\mu}_{00}$	0.53 + Z_{eff}	3.54 / 2	(3.02 + 4.25 Z_{eff}) / C
$\hat{K}_{01}$	0.71 + Z_{eff}	10.63 / 2	(12.43 +20.13 Z_{eff}) / C
$\hat{\mu}_{11}$	1.39 + 13 $Z_{eff}/4$	11.52 / 2	(15.38 + 26.97 Z_{eff}) / C

Table 2.1: The asymptotic dimensionless viscosity coefficients. Here C = 2.23 + 5.23 Z_{eff} + 2.40 Z_{eff}^2. In the the case of the impurity species Z_{eff} should be replaced everywhere with α from Eq. 2.8. This table was reproduced from Table 1 of Ref. [16].

2.1.4 Radial Electric Field

If the poloidal rotation is neoclassical, then there is an equivalence between toroidal rotation and the radial electric field. As can be seen in equations 2.1 and 2.2, the electric field term plays a critical role in the magnitude and even the direction of the toroidal rotation velocity.

Rearranging Eq. 2.1, yields:

$$E_r = V_\phi^I B_\theta - \frac{(K_1 + \frac{3}{2}K_2 - 1)}{e}\frac{\partial}{\partial r}T_i + \frac{T_i}{en_i}\frac{\partial}{\partial r}n_i. \tag{2.16}$$

This then gives a way to infer the radial component of the electric field in the plasma, using exclusively measured quantities.

2.2 Revisited Neoclassical Theory

Revisited neoclassical theory is a step from the more fundamental and better established neoclassical theory (§2.1). The primary difference of revisited neoclassical theory is a more thorough treatment of the high collisionality regimes[18]. Transport barriers, both the high confinement (H–mode) edge barrier and the more recent internal transport barrier (ITB), exhibit gradient scale lengths too short, and too anisotropic to allow some of the assumptions made in the formulation of neoclassical theory[18]. Revisited neoclassical theory attempts to deal with the high collisionality in these regions.

2.2.1 Parallel Flow Velocity

Revisited neoclassical theory gives, among other things, an expression for the parallel flow velocity. The improved theory starts by solving Braginskii's two fluid equations, and reducing them to a set of four coupled, one dimensional equations[18]. After many pages of calculations (detailed in [18]), an approximate expression for the ion flow velocities is given by[1]:

$$U_{\|,i}^{(1)} = -h_\phi B_\phi \frac{cT^{(0)}}{eB_0}\left(\frac{e}{T^{(0)}}\frac{\partial V^{(0)}}{\partial \psi} + (1+\eta)\frac{\partial}{\partial \psi}\ln N^{(0)}\right) \tag{2.17}$$

and:

$$U_{\chi,i}^{(2)} = 0 \tag{2.18}$$

where: $U_{\|,i}^{(1)}$ and $U_{\chi,i}^{(2)}$ are the toroidal and poloidal ion rotation velocities, respectively, h_ϕ is the Jacobian of the transformation $r \rightarrow (\psi, \chi, \phi)$, ψ is the direction of the poloidal flux, χ is the direction of the poloidal magnetic field and ϕ is the toroidal angle. The viscosity coefficient is given by η, and $N^{(0)}$ is the density.

2.2.2 Momentum Evolution Time Scales

Revisited neoclassical theory gives an expression for the expected momentum evolution time scales [18]. There are two orderings that will be considered here, both consequences of the parallel momentum equation, Eq. (41) from Ref. [18], stated here as Eq. 2.19, for completeness[2]:

$$\oint JB\frac{d\chi}{2\pi}\left[\nabla\cdot\pi_i + m_i N_i\left(\frac{\partial}{\partial t} + \mathbf{U_i}\cdot\nabla\right)\mathbf{U_i}\right]\cdot\hat{n} = 0. \tag{2.19}$$

where: J is the current density, π_i is the stress tensor and $\hat{n}$ is the unit vector along the field lines.

[1]Parallel flow velocity, i.e. the toroidal rotation velocity, will be referred to as $U_{\|,i}^{(1)}$; and poloidal rotation velocity as $U_{\chi,i}^{(2)}$. This is done to remain consistent with the notation in the principal reference for this section [18].

[2]Also recast as Eq. (60) in Ref. [18].

The first of these orderings is the viscous relaxation time of parallel flow:

$$(\tau_{U_{\parallel,i}})_{viscous} \sim \epsilon^{-2} \left(\frac{qR\nu_i}{c_i} \right)^2 \tau_i \tag{2.20}$$

where: ϵ is the inverse aspect ratio, q is the safety factor, ν_i is the collision frequency, c_i is the sound speed, and τ_i is the confinement time.

The second is the evolution time scale provided as a consequence of finite ion Larmor radius and ion inertia.

$$(\tau_{U_{\parallel,i}})_{f.l.r.} \sim q^{-2} \frac{L_\psi^2}{a_i^2} \tau_i \tag{2.21}$$

where: $L_\psi = \frac{1}{\psi(r)} \frac{d}{dr} \psi(r)$, and a is the minor radius.

2.3 Subneoclassical Theory

Subneoclassical theory is in some sense more comprehensive than revisited neoclassical theory, in terms of the orderings. Although more complicated, it is also arguably more detailed. Depending on the application one must evaluate whether the increased complication is justified. For completeness this theory will be discussed here; for more detail consult Ref. [19].

Subneoclassical theory is an extension of revisited neoclassical theory, with the inclusion of finite Larmor radius and inertial effects, previously left out of revisited neoclassical theory. Of fundamental importance, is that this theory provides a non-degenerate ambipolarity constraint, and helps to define E_r and V_ϕ[19].

2.3.1 Ambipolarity Constraint

Subneoclassical theory states that the ambipolarity constraint is linked to momentum and momentum confinement through the neutrality constraint. Perpendicular particle diffusion is a random walk process with step size ρ_L, the Larmor radius. The particle's orbit around the field geometry is directly related to the particle's momentum, by the neutrality requirement. Charge separation and associated electric field that is set up

heavily influence the particles momentum. Thus, the particle's momentum is linked to the ambipolarity constraint.

This may seem trivial, but it offers an explanation as to why the momentum confinement time scales and the particle confinement time scales are thought to be similar. Particles carry momentum, thus momentum confinement must be related to that of the particles which carry the momentum.

Reference [18] gives what is called the ambipolarity equation, (Eq. 58, Ref. [18]). Through some substitutions and assuming a circular plasma cross section, it is found that the momentum confinement time scale $\tau_{U_{\parallel,i}}$ is comparable to the neoclassical relaxation time of the temperature:

$$\tau_{U_{\parallel,i}} \sim \tau_{T_i} \sim \left[1 + \frac{Q^2}{S^2}\right] \left(\frac{T_i}{E_r e q a_i}\right)^2 \tau_i \tag{2.22}$$

where:

$$Q = 4\left(\frac{U_{\theta,i} B_\phi}{B}\right) - 5\left[\frac{T}{eB}\frac{\partial}{\partial r}\ln(N\sqrt{T})\right] \tag{2.23}$$

$$S = 2\left(\frac{\chi_{\parallel,i}}{rN}\right)\frac{B_\theta^2}{B^2} \tag{2.24}$$

with $\chi_{\parallel,i}$ being the parallel heat transport coefficient.

2.3.2 Subneoclassical Heat Flux

Subneoclassical theory redefines the neoclassical and revisited neoclassical heat flux. (This derivation and the associated result can be found in Ref. [19].) In both neoclassical and revisited neoclassical theory the ordering of terms yielded expressions that were only valid where the collisionality was high and the spatial gradients of plasma parameters varied slowly, i.e. long scale lengths, $\rho_i \ll L_n$. This requirement is not met in the H–mode plasma edge, nor, necessarily, in the ITB region of the plasma ($\frac{\rho_i}{L_n} \simeq \frac{1}{40}$).

Using the ambipolarity equation (Eq. (58), Ref. [18]), and assuming time inde-

pendent profiles, we can write:

$$\tau_{U_{\|,i}} = -\frac{3.12}{(\hat{u}_1 + \hat{u}_2)} \frac{\tau_i}{q^2 a^2} \left(\frac{1}{T_i} \frac{\partial T_i}{\partial r} \right)^2 \tag{2.25}$$

where:

$$\hat{u}_1 + \hat{u}_2 = F\nu_{cx} + \left[2k - 1.5 - \frac{2}{\eta_i} - \frac{2-z}{p} \right] \tag{2.26}$$

where: $\hat{u}_1$ and $\hat{u}_2$ are N_0, N_i, T_i, $Z_{eff,i}$, $\dot{m}_{\phi,i}$, and J_r profiles[3], ν_{cx} is the charge exchange cross section, k and p are profile parameters, η_i is the viscosity coefficient, and:

$$F(x) = 0.8 \left(\frac{eB}{\partial T / \partial r} \right) \frac{R^2}{r\Lambda_1} \tag{2.27}$$

where: x is the distance from the LCFS: $x \equiv r - r_{lcfs}$

$$\Lambda_1 = 0.19 \frac{\sqrt{A_i}}{B} (Z_{eff} N_{(20),i}) \frac{q^2 R^2}{T_i^{3/2}} \left(\frac{r}{T_i} \frac{\partial T_i}{\partial r} \right)^{-1} \tag{2.28}$$

with: A_i majority ions' atomic mass, B in Tesla, $N_{(20),i}$ is the density in units of 10^{20} m^{-3} and T_i in eV .

This equation (Eq. 2.25) is another momentum confinement time scale, based on the subneoclassical heat flux. It should be noted that $(\hat{u}_1 + \hat{u}_2) > 0$ corresponds to a linear relaxation of the rotation and $(\hat{u}_1 + \hat{u}_2) < 0$ corresponds to a linear acceleration[19].

There now exists a theory that is valid over the entire plasma. The subneoclassical theory attempts to explain transport even in the steep edge gradients, and the steep gradient regions of the ITB.

[3]If the the condition $(\hat{u}_1 + \hat{u}_2)^2 \geq 4\hat{u}_1\hat{u}_2$ is satisfied, this implies profiles where ambipolarity could not be preserved[19].

2.4 ICRF Induced Rotation

In recent years, much work has been done to explain plasma rotation generated by ion cyclotron radio frequency (ICRF) waves. In this section some of the current theories of ICRF driven rotation are outlined.

Ion cyclotron resonance heating (ICRH) can induce nonambipolar minor radial transport of resonant ions. This can lead to charge separation, and hence a modification of the radial electric field profile, this in turn will lead to a toroidal rotation velocity[20].

During simple, collisionless guiding center motion in a torus the orbit excursions inward and outward exactly cancel out leading to no net minor radial transport. This precise balance of particle motion is known as omnigenity. During ICRH this omnigenity rarely holds.

In a plasma with pressure gradients, the symmetry of Coulomb collisions can be broken and a net particle transport can arise. This leads to the well known neoclassical transport (§2.1); it is automatically ambipolar[20].

2.4.1 Perkins' Theory

Perkins' theory of ICRH induced rotation assumes a plasma of two components: a high energy tail and a bulk plasma in thermal equilibrium[21]. The bulk plasma responds to applied torque via angular momentum diffusion. The high energy ions lose energy and redistribute themselves by ion–ion pitch angle scattering and drag collisions. This leads to particle displacements both radially inward and outward, and can result in net particle loss and thus radial currents. Radial currents in the energetic tail must be balanced by radial currents in the bulk plasma, creating a torque density. Energetic particles also directly transfer momentum to the bulk by collisions[21].

Using the Monte Carlo ORBIT code[22, 23] calculations and predictions of the induced rotation were made. It was predicted that as the resonance location moved from the low field side of the plasma to the high field side of the plasma, the induced

torque and hence the rotation velocity should change direction[21]. Experimentally, this has been shown not to occur[24].

2.4.2 RF Orbit Shift Theory

In the RF drive theory presented by Chang [20, 25], rotation is driven by a radial electric field (E_r) generated by an ICRF induced radial current (j_r^{rf}). The large radial dielectric constant of the plasma allows the growth of a plasma return current (j_r^p), which grows until it is equal to $-j_r^{rf}$, thus stopping further growth of the radial electric field[20].

As the currents grow and take shape the bulk plasma will be subject to both $j_r^p \times B_\theta$ and $j_r^p \times B_\phi$ forces, while the resonant ions will be subject to $j_r^{rf} \times B_\theta$ and $j_r^{rf} \times B_\phi$ forces. Different loss rates between the resonant and nonresonant ions, will lead to a net input of toroidal angular momentum[20].

The main differences in loss rates arise from asymmetries in trapped particle orbits, and the growth rates of the inner and outer legs of the orbits, while the currents (j_r^p and j_r^{rf}) are transient. Reference [20] also uses the code ORBIT [22, 23], to make calculations of the guiding center motion of particles and the subsequent j_r^{rf} that arises. The authors then go on to estimate the electric field that will arise and discuss the development of toroidal rotation, specifically for the Tokamak Fusion Test Reactor(TFTR). In a later paper, Chang makes estimates of the growth of toroidal rotation vs. time in C–Mod[25]. It was stated the toroidal rotation would grow like:

$$\langle RV_\phi \rangle = \langle RV_\phi^0 \rangle (1 - e^{-t/\tau_\phi}) \tag{2.29}$$

where $\langle RV_\phi^0 \rangle$ is the terminal toroidal angular speed. More will be said about this in Chapter 6 when some data are compared to various theories.

2.4.3 Rotation Drive Theory: RF Tail

A theory for the generation of rotation and current drive by the asymmetric launching of ICRF power has been proposed by T. Hellsten[26]. A code SELFO, has been

developed. SELFO self consistently calculates the velocity distribution and the power deposition using a quasi–linear theory for wave–particle interactions, (velocity distribution calculated with the Monte Carlo code FIDO[27], wave field calculated with the global wave code LION[28, 29].)

It has been found that waves launched toroidally co–current generate large fast ion tails. However, waves launched counter–current fail to generate tails with as high energies; by similar mechanisms as the RF drive theory (§2.4.2), this leads to toroidal momentum input.

2.5 Spontaneous Plasma Rotation

It has been observed that during Ohmic high confinement modes (Ohmic H–modes), a plasma will start to rotate in the co-current direction. With no auxiliary power input, no neutral beam injection or ICRF power input, the possibility of momentum transfer from either of these sources has been totally removed [30]. The plasma has been seen to rotate, so a theory to explain this is required. One such theory is the so called accretion theory.

2.5.1 Accretion Theory

The H–mode equilibria of a tokamak plasma produce steep density and temperature gradients in the edge of the plasma. These gradients naturally form a steep pressure gradient which is capable of giving rise to various modes that drive plasma rotation[31].

Accretion theory is based on the balance of the inflow velocity of the angular momentum with the outward diffusion from the interior of the plasma column. This being the premise, the momentum flux which includes both diffusion and convection, is given by the equation[31]:

$$\Gamma_J \simeq -m_i n \left(J_0 v_J + D_J \frac{\partial J}{\partial r} \right) \tag{2.30}$$

where $m_i n J$ is the momentum density with $J = R v_\phi$. Eq. 2.30 is to be used in the momentum continuity equation:

$$m_i n \frac{\partial J}{\partial t} + \nabla \cdot \Gamma_J = S_J \tag{2.31}$$

where S_J is a momentum source at the edge of the plasma. Following the example of the particle transport model, the ratio of v_J/D_J is an increasing function of radius, with the specific form:

$$\frac{v_J}{D_J} \simeq 2\frac{r}{a^2}\alpha_J. \tag{2.32}$$

In the numeric solution of Eq. 2.30, α_J is taken to be a free parameter across the minor radius of the plasma. Experimental profiles are then matched by varying α_J to yield a solution, with a constant source term S_J.

Using quasi-linear theory, Coppi shows that electrostatic modes driven by the ion pressure gradient can produce a momentum inflow that lends merit to the momentum flux, Eq. 2.30[31].

Considering electrostatic modes in slab geometry of the form:

$$\hat{\phi} \simeq \tilde{\phi} \exp(-i\omega t + ik_y y + ik_\parallel z) \tag{2.33}$$

that are localized around a surface $x = x_0$, with a Doppler shifted frequency $\bar{\omega} =$ ω - $k_\parallel v_\parallel(x_0)$. If $\bar{\omega} > k_\parallel v_{thi}$ the perturbed parallel momentum conservation equation becomes:

$$m_i n \left(-i\bar{\omega}\tilde{v_\parallel} + \frac{-ik_y\tilde{\phi}}{B}\frac{dv_\parallel}{dx} \right) = -ik_\parallel \tilde{p_i} - ik_\parallel en\tilde{\phi}. \tag{2.34}$$

Considering $(\bar{\omega}/k_\parallel \ \frac{d}{dx}v_\parallel) \sim (\frac{d}{dx}p_i)/(m_i n)$ and $|\frac{d}{dx}p_i|/(eBn) > |\bar{\omega}/k_y|$ then[31]:

$$\tilde{v_\parallel} \simeq -\frac{k_y}{\bar{\omega}}\frac{\tilde{\phi}}{B}\left[\frac{dv_\parallel}{dx} + \frac{k_\parallel}{m_i n\bar{\omega}}\frac{dp_i}{dx}\right]. \tag{2.35}$$

These equations lead to a dispersion relation for the electrostatic modes which

can be found in Ref. [31]. Further, a quasi-linear flux can be stated as:

$$\Gamma_k \simeq -\frac{2\gamma_k}{\bar{\omega_k}^2}\langle|\hat{v}_{E_x}^{(k)}|^2\rangle \left[m_i n\frac{dv_\parallel}{dx} + 2\frac{k_\parallel}{\bar{\omega_k}}\frac{dp_i}{dx}\right] \tag{2.36}$$

here $\gamma_k = Im(\bar{\omega_k})$ is the mode growth rate, $\langle|\hat{v}_{E_x}^{(k)}|^2\rangle$ is the mode amplitude, and $D_k = \frac{2\gamma_k}{\bar{\omega_k}^2}\langle|\hat{v}_{E_x}^{(k)}|^2\rangle$.

Accretion theory offers an explanation of spontaneous plasma rotation based on instabilities of electrostatic modes, driven by ion pressure gradients. This theory offers an explanation why momentum is preferentially transported up the temperature gradient. Further, accretion theory shows similarities between momentum confinement and particle and energy confinement.

2.5.2 Toroidal Momentum Pinch and Flow Reversal

Spontaneous rotation as a result of fluctuation-induced toroidal stress has been proposed by K.C. Shaing[33]. This theory is motivated by the failure of neoclassical toroidal stress to explain observed toroidal momentum confinement[33].

This theory determines the toroidal rotation profile, up to a constant, by balancing the diffusion flux and the pinch-like flux. The constant then turns out to be the $U_{\parallel 0}$ the rotation velocity on the magnetic axis. $U_{\parallel 0}$ is then determined by evaluating the residual stress[33].

Shaing begins his theory from the drift kinetic equation[14], (Eq. (1) from [33]):

$$\frac{\partial f}{\partial t} + (v_\parallel \hat{n} + \boldsymbol{v}_d)\cdot\nabla f + \frac{e}{M}\frac{\partial \Phi}{\partial t}\frac{\partial f}{\partial \epsilon} = C(f) \tag{2.37}$$

where: f is the particle distribution, $v_\parallel$ is the velocity parallel to the magnetic field, $\hat{n} = \boldsymbol{B}\ /\ B$, $\boldsymbol{v}_d$ is the drift velocity, Φ is the electrostatic potential, $\epsilon = \frac{v^2}{2} + \frac{e\Phi}{M}$ is the particle energy and $C(f)$ is the coulomb collision operator.

At this point it is assumed that only the electrostatic fluctuation induced stress is of interest. Only the $\mathbf{E}\times\mathbf{B}$ drift velocity is kept in the linearization process[33].

Under these assumptions Eq. 2.37 reduces to:

$$v_{\|}\hat{n}\cdot\nabla f_0 = C(f_0), \tag{2.38}$$

with the solution:

$$f_0 = \frac{N}{\pi^{3/2}v_t^3}\exp\left(-\frac{v^2}{v_t^2} - \frac{2e\tilde{\Phi}}{Mv_t^2}\right). \tag{2.39}$$

The next order kinetic equation is:

$$\frac{\partial f_1}{\partial t} + (v_{\|}\hat{n} + \boldsymbol{v}_d)\cdot\nabla f_1 + \frac{e}{M}\frac{\partial\hat{\Phi}}{\partial t}\frac{\partial f_1}{\partial\epsilon} + \boldsymbol{v}_d\cdot\nabla f_0 + \frac{e}{M}\frac{\partial\hat{\Phi}}{\partial t}\frac{\partial f_0}{\partial\epsilon} = C(f_1) \tag{2.40}$$

which can be solved with the expansion:

$$f_1 = g + \frac{2v_{\|}U_{\|}}{v_t^2}f_0 + \frac{2v_{\|}^2U_{\|}^2}{v_t^4}f_0 + \cdots \tag{2.41}$$

here g is a localized distribution, $U_{\|}$ is the parallel flow speed.

Shaing argues, Ref. [33], that the steady state rotation velocity profile satisfies the equation:

$$\frac{\partial}{\partial\psi}U_{\|} - \frac{5}{2}\left(\frac{1}{T}\frac{\partial}{\partial r}T\right)U_{\|} = 0 \tag{2.42}$$

with the solution:

$$U_{\|} = U_{\|0}\left(\frac{T}{T_0}\right)^{\frac{5}{2}} \tag{2.43}$$

where 0 denotes quantities on the magnetic axis. To determine the quantities on the magnetic axis, the inhomogeneous equivalent of Eq. 2.42 must be solved, where the right hand side is given by R the residual stress.

$$\frac{\partial}{\partial\psi}U_{\|} - \frac{5}{2}\left(\frac{1}{T}\frac{\partial}{\partial r}T\right)U_{\|} = R \tag{2.44}$$

with the solution:

$$U_{\|} = U_{\|0}\left(\frac{T}{T_0}\right)^{\frac{5}{2}} + \int_0^{\psi} d\psi' R\left[\frac{T(\psi')}{T(\psi)}\right]^{-\frac{5}{2}}. \tag{2.45}$$

The magnitude and sign of $U_{\|0}$ are determined if the boundary conditions are known. If $U_{\|}(\psi_a) = 0$ then:

$$U_{\|0} = -\int_0^{\psi_a} d\psi' R\left[\frac{T(\psi')}{T(\psi)}\right]^{-\frac{5}{2}}. \tag{2.46}$$

This theory offers an explanation for the reversal of plasma rotation during the L $\rightarrow$ H transition during Ohmic discharges.

2.6 ITB Theory

This section will touch on the current "State of the Art" for ITB theory, following Connor, Ref. [34][4].

Current thinking relates the formation of an ITB with the suppression of microturbulence, most likely, through some sort of dynamic bifurcation theory[35–42].

In an ITB the primary transport mechanism has been changed from one of a turbulent nature to a more neoclassical situation. This relative increase in confinement, reduction in transport, leads to an improved operating regime, with added benefits of increased plasma pressure, and a large bootstrap current[43, 44].

The suppression of microturbulence is thought to be achieved through shearing in the $\mathbf{E} \times \mathbf{B}$ flows in the plasma. These $\mathbf{E} \times \mathbf{B}$ flows, around the toroidal and poloidal directions of the plasma, act to break up smaller turbulent cells that are primarily responsible for the anomalous transport. The common expression for the influence of the $\mathbf{E} \times \mathbf{B}$ shear on microturbulence is the shearing frequency[45]:

$$\omega_E = \frac{RB_\theta}{B}\frac{d}{dr}\left(\frac{E_r}{RB_\theta}\right)\cdot\frac{k_\theta}{k_r} \tag{2.47}$$

[4]This work is not yet published, so many other references have been included. Connor's review paper is totally comprehensive, and an excellent source for ITB information, both theory and experiment.

where: R is the major radius, B is magnetic field, E_r is the radial electric field, and k_θ and k_r are poloidal and radial wave numbers, (k_θ / $k_r \sim 1$).

A generally accepted criterion for the $\mathbf{E} \times \mathbf{B}$ shear to suppress turbulence is given as $\omega \geq \gamma$, where γ is the growth rate of the instability causing the turbulence. A common quantitative measure is $\gamma \simeq \frac{c_s}{R}$, where c_s is the sound speed[46, 47].

Low or reversed magnetic shear has also been linked to the reduction in or even suppression of, drift wave instabilities, their radial extent and the transport for which they are responsible[34, 48]. Presently, there are indications that the magnetic field and its profile can also influence the location of the foot of the barrier. Magnetic field and its profile will prove very important in the development of and operation in, ITB regimes.

2.7 Chapter Summary

Neoclassical, Revisited neoclassical, Subneoclassical theory, will all be compared to the results in this thesis. It will be shown that none of these theories adequately explain the results presented here. These theories have been included for the sake of completeness. Perhaps these theories could be revised based on the results in later chapters.

Neoclassical theory is the most fundamental explanation of plasma transport, and it is from this that many other theories stem. Revisited neoclassical theory is a step on the way to a theory that adequately treats all regimes of the plasma. By including effects of regions of high collisionality, the theory properly treats most of the plasma. Two orderings for the momentum confinement time were presented; first for the viscous relaxation time and the second as a consequence of the finite Larmor radius and ion inertia. Subneoclassical theory is a further reordering of neoclassical theory for various regimes, and modes of operation, it is valid over the widest range of plasma regimes and for all relevant gradient scale lengths. This is the most comprehensive because it can be used even in the H–mode pedestal and the ITB region. It is important to note that neoclassical theory is established and in some sense supported

by experiment; while both revisited neoclassical theory and subneoclassical theory are unsubstantiated and unproven by experiment.

ICRF rotation theories explain plasma rotation by generation of currents in the plasma and the loss of particles by through various asymmetric loss rates. Trapped particles play a crucial role in the generation of angular momentum. Wide banana widths can have dramatically different growth rates of their inner and outer orbit legs. This will lead to asymmetries in the radial transport of resonant and nonresonant particles as well as trapped and untrapped particles; the differences in loss rates will lead to a net introduction of angular momentum.

Two theories of spontaneous plasma rotation have been presented here: Coppi's accretion theory, and the theory of toroidal momentum pinch and flow reversal, as given by Shaing. Coppi finds plasma rotation induced by various electrostatic modes arising from pressure gradients. Shaing explains rotation by fluctuation induced toroidal stress.

Finally, the theory of ITBs was discussed, following the work of J. W. Connor[34]. ITBs are believed to be most closely linked to the suppression of microturbulence by $\mathbf{E} \times \mathbf{B}$ shearing. Other important factors include the growth rates of various drift wave instabilities, and the magnetic field and its profile shape.

Chapter 3

Previous Results on Rotation

The tangentially viewing high resolution x–ray spectrometer (THIREX) array on C–Mod was inspired from a single tangentially viewing high resolution x–ray spectrometer on Alcator C, HIREX jr[51]. The experiment was designed to measure (impurity) toroidal rotation on the plasma axis. This chapter will be divided into four sections. The first discusses other high resolution x–ray spectroscopic measurements on C–Mod, while the second details similar rotation measurements on other machines. The third covers other (non-beam based) spectroscopic rotation measurements. Finally, the fourth section details toroidal rotation measurements from beam based diagnostics. The chapter concludes with a brief chapter summary.

3.1 High Resolution X–Ray Spectrometer Measurements on C–Mod

This section will briefly point out and highlight some of the previous rotation measurements made by high resolution x–ray spectroscopy on C–Mod.

3.1.1 High Resolution X–Ray Spectroscopy on C–Mod

The high resolution x–ray (HIREX) spectrometer array on C–Mod was initially employed to measure both toroidal and poloidal rotation, ion temperature profiles, impurity transport, neutral hydrogen densities, impurity density and for atomic physics

studies[52]. Since its inception, it has been used to make many rotation measurements[17, 24, 53]

Figure 3-1 is a top view of the HIREX array at B–port. The HIREX array had five spectrometers (presently 3) with views into the plasma at various angles, these views could be swept through a range of poloidal angles to make measurements with different poloidal/radial components. However, the toroidal angle of the measurement is fixed. The spectrometers are all scanable in wavelength, on a shot to shot basis.

The five spectrometers all had different views. Of the five, some pairs were symmetric about the mid–plane and/or the radius of the port. By adding and subtracting the signals from these various spectrometers the poloidal and toroidal impurity rotation can be determined. The sixth spectrometer, HIREX jr, not in the array, has a purely tangential view at C–port, (Fig. 3-1).

Figure 3-2 is a view of the HIREX array, in a poloidal cross-section of the machine. The overlap in the different spectrometer views allow the entire plasma to be viewed by the spectrometer array.

Figure 3-3 are some data from previous HIREX rotation measurements. The measurement in the center of the plasma was made with the tangentially viewing spectrometer located in C–port, again see Fig. 3-1; the error associated with this measurement is fairly small. The measurements made radially further out, (Fig. 3-3), were made with the mostly poloidally viewing spectrometers. The error associated with these measurements are quite large, because the the toroidal angle is quite small ($\sim 6^{\circ}$). The contribution to the error because of this angle is proportional to the secant of the toroidal angle of observation. This method of toroidal rotation measurement was also limited by the long integration time required to get sufficient counting statistics.

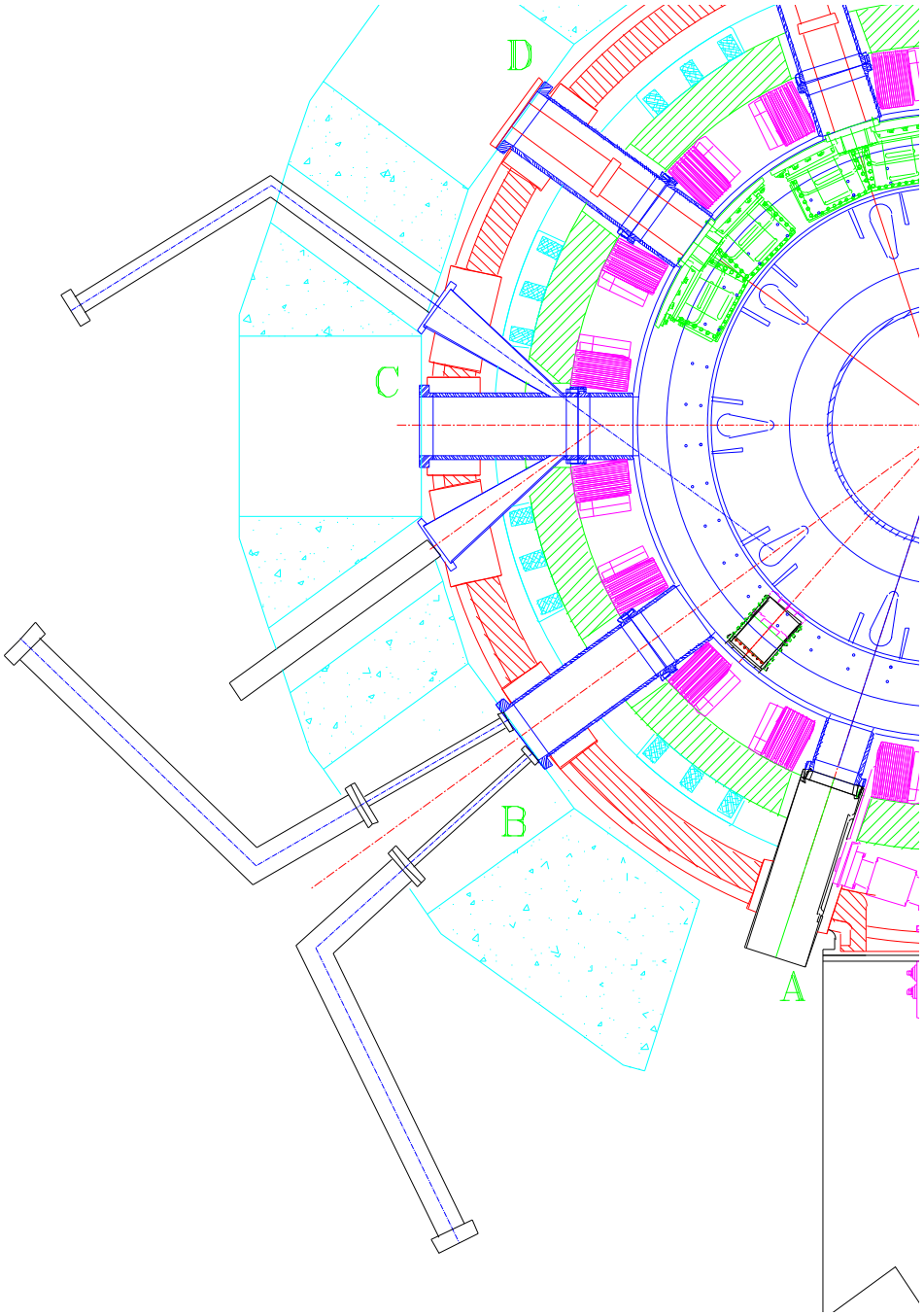

Figure 3-1: A top view of the old HIREX array on B–port. The views of the spectrometers are almost normal to the surface of the plasma. However, each spectrometer has a slight toroidal component ($\sim 6°$) to its view angle. The array had 5 spectrometers, two on top of each other on the left (C–port side), and three stacked on top of each other on the right (A–port side). The spectrometers are vertically scanable, see Fig. 3-2. The original central tangential view can be seen on C–port.

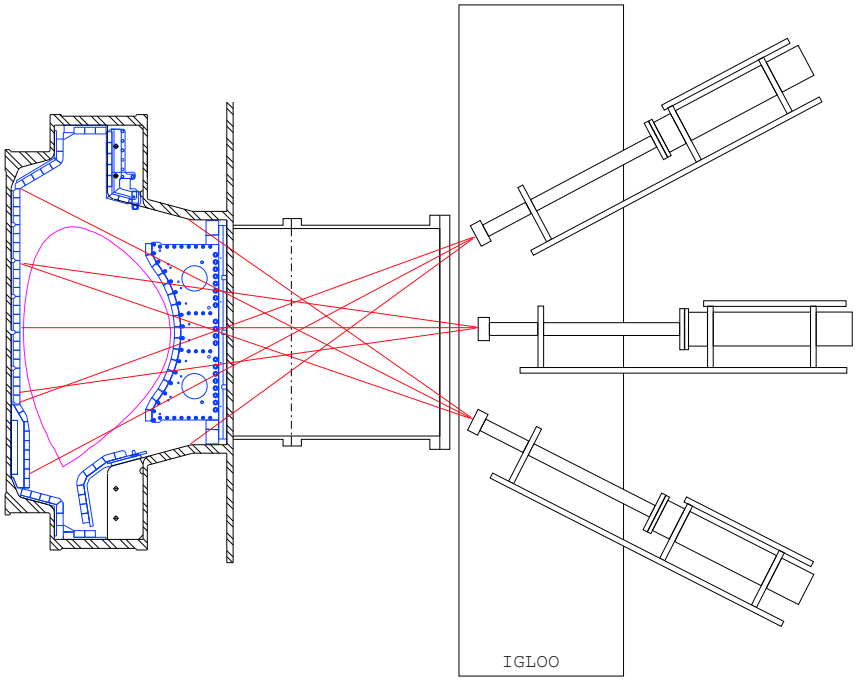

Figure 3-2: A view of the HIREX array, in a poloidal cross-section. The views of the individual spectrometers can be swept through a range of angles allowing for a large area of possible viewing. This is a view of the A–port side of B–port, (*i.e.* through B–port looking towards A–port), also see Fig. 3-1 for orientation.

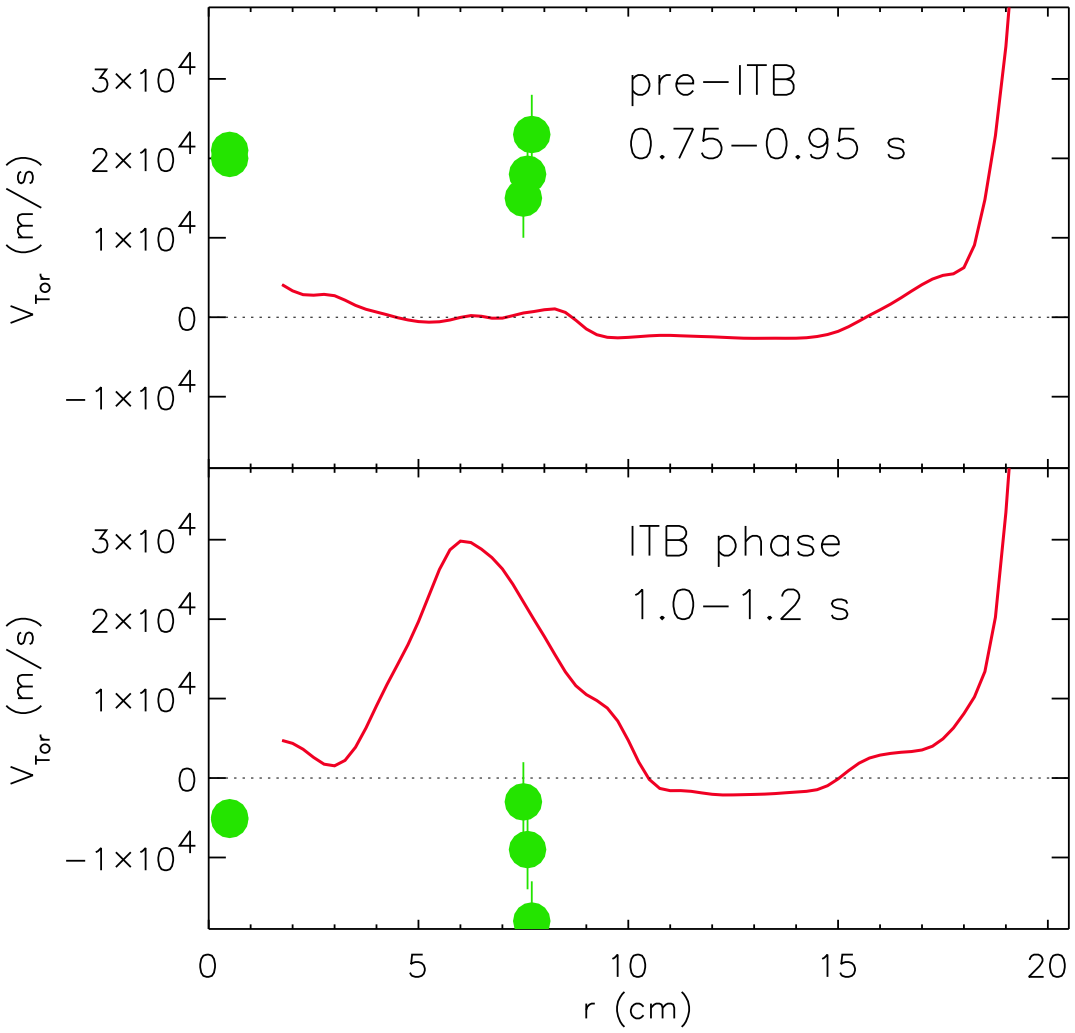

Figure 3-3: Plotted here is toroidal rotation vs. radius, (Green Circles). The upper plot is in H-mode before the ITB phase of a discharge, and the lower plot is during the ITB phase of the discharge. Previous measurements of V_ϕ have been quite limited. Further, the data gleaned from the mostly poloidally viewing HIREX array have large error bars. Plotted over these data, as the solid line, is the rotation profile as calculated from neoclassical transport theory, with $E_r = 0$. This discrepancy between the measured and theoretical prediction for the rotation velocity indicates the presence of a radial electric field. (More on this can be found in Chapter 2: Rotation Theory.)

3.2 High Resolution X–Ray Measurements on Other Machines

C–Mod is not the only machine that has used a high resolution x–ray spectrometer to measure plasma rotation.

3.2.1 High Resolution X–Ray Spectroscopy on DITE

A Johann configuration crystal spectrometer was used on the tokamak DITE to investigate lines of O and Fe. Measurements were made during 2.1 MW of co-current neutral beam injection, the plasma was found to rotate around 150 km/s[54]. Further, this exceeded the rotation velocity in any other mode of operation by nearly an order of magnitude[54]. These measurements were enhanced during H^0 beam injection. Perpendicular momentum diffusivities, (χ), were calculated and found to be about 0.6 m^2/s, at least an order of magnitude above the expected value from classical or neoclassical theory.

3.2.2 High Resolution X–Ray Spectroscopy on PDX

The poloidal divertor experiment (PDX)[55] was one of the first machines to use a bent crystal spectrometer, to measure x–rays emitted from a plasma, for diagnostic purposes. V_ϕ measurements were made using Doppler shifted Ti XXI (x–ray) and Ti XVII (visible) lines. By using both of these lines, V_ϕ at two radial locations was measured, (r/a $\sim$ 0.0 and r/a $\sim$ 0.5). During NBI, V_ϕ was found to reach values near 100 km/s on axis and about 40 km/s at r/a $\sim$ 0.5. The profile was found to be peaked. Toroidal rotation decay times were found to be between $\sim$ 0.080 – 0.180 s, significantly longer than other machines. It was determined that at the time all existing theories were inadequate to describe the damping rate of V_ϕ.

3.2.3 High Resolution X–Ray Spectroscopy on TFTR

High resolution x–ray spectroscopy has been used to measure impurity parameters[56] on the Tokamak Fusion Test Reactor (TFTR). In TFTR these data were taken using a Johann geometry bent crystal spectrometer and lines from He–like titanium, (Ti XXI.) The maximum rotation velocity recorded was 500 km/s, this during a 15 MW deuterium beam injection[1]. This spectrometer was also a very high resolution instrument, $\lambda/\Delta\lambda = 25\ 000$.

In addition to many atomic physics results, experiments from TFTR showed beam heated rotation results consistent with expectations from the calculated input torque. Using the rotation decay after the beams were shut off, an L–mode momentum confinement time ($\tau_{L\phi}$) of about 0.3 s was deduced.

3.2.4 High Resolution X–Ray Spectroscopy on JET

High resolution x–ray spectroscopic measurements have been made on the Joint European Torus (JET) using a bent crystal spectrometer. Using this spectrometer, the JET team is able to measure many different spectral lines[57], see Table 3.1. The spectrometer has very high wavelength resolution $\lambda/\Delta\lambda = 20\ 000$, and time resolution of $\sim 20\ ms$[57]. It is quite difficult to scan the spectrometer in wavelength though.

Since the spectrometer was installed, it has been used to make toroidal rotation measurements, predominantly using He–like Ni, (Ni XXVII)[58, 59]. JET has also made some observations using the spectrometer during the ICRH portion of some discharges. During plasmas heated exclusively by ICRF waves, rotation has been seen to change from the Ohmic case by 30 km/s. No profile information has been taken with this spectrometer, as it is only one single channel.

On JET they have also performed a series of experiments that compared the rotation frequency of C and Ni, $\Omega_{\phi C}$ and $\Omega_{\phi Ni}$, respectively. They found that the two frequencies had almost perfect correlation, for the same value of effective minor

[1] 15 MW of deuterium beam power represents a substantial momentum input.

Ion	Crystal	hlk	λ (Å)	θ_B (°)	$2d$ (Å)	R_i
Cr XXIII	quartz	$20\bar{3}$	2.18	52.45	2.7496	1.80×10^{-5}
Cr XXIII	Ge	400	2.18	50.43	2.8280	4.65×10^{-5}
Ni XXVII	quartz	$22\bar{3}$	1.59	51.57	2.0296	0.41×10^{-5}
Ni XXVII	Ge	440	1.59	52.67	1.9998	2.13×10^{-5}
Ti XXI	quartz	103	2.62	52.15	3.3178	0.77×10^{-5}
Ar XVIII	quartz	110	3.73	49.39	4.9130	1.84×10^{-5}

Table 3.1: Here is a table of some of the characteristics of the spectrometer on the JET tokamak, taken from page 240 of reference [57]. For each: h, l, k the Miller indices of the crystal, λ (Å) the wavelength for which they are computed, θ_B (°) the Bragg angle, $2d$ (Å) the atomic plane spacing and R_i the integrated reflectivity

radius, ($\langle\rho\rangle$)[59]. This indicates that both of the impurities were strongly coupled to the bulk plasma.

The measured timescale for plasma acceleration, has been found to be comparable to Spitzer's slowing down time[58]. This corresponds to the timescale for both tail formation and ICRH induced radial diffusion. In later experiments, a correlation between edge neutral density and both angular rotation frequency and angular momentum density, was shown[59]. It was also determined that the ion pressure gradient was the main driving mechanism for toroidal rotation.

3.3 Other Spectroscopic Rotation Measurements

This section will give quick briefs about rotation measurements made on quite a few other experiments using various spectroscopic means. These should be differentiated from high resolution x–ray spectroscopic measurements, (§3.1 & §3.2) and from the beam based spectroscopic measurements, (§3.4).

The measurements presented here have been made with an intrinsic impurity, and in either the visible or the UV region of the plasma. Measurements of this type could not be made in Alcator, due to the plasma temperature and density.

Some of the first measurements of plasma rotation in tokamaks were made in the LT – 3 tokamak[60]. Measurements were made using Doppler shifted lines of ionized oxygen impurities. The plasma was observed to rotate toroidally with the current,

at about 5 km/s. The oxygen – oxygen collision frequency was determined to be much less than the oxygen – hydrogen collision frequency. This implies the impurity is collisionally coupled to the bulk plasma, parallel to the magnetic field. Thus, the flow velocity of the two ions should be the same. Poloidal rotation was determined to be neoclassical, and toroidal rotation was determined to be anomalous.

In the Princeton Large Torus (PLT) rotation was studied using some lines of H I, C V and Fe XX. Using NBI, peak rotation velocities of $\simeq$ 120 km/s were found[61]. By using the three aforementioned, lines a three point profile was measured, and it was found to be quite peaked. Measurements were made, during Ohmic, H^0 – beam, and D^0 – beam heating. During Ohmic L–mode plasmas, the rotation was found to be in the counter-current direction, with a small value $\sim$ 10 km/s. A beam orbit code was developed and compared with the data; good agreement was found[61]. Momentum diffusivities (χ_ϕ) of $\sim$ 1 – 3 m^2/s were found. Calculations based on neoclassical theory indicate a central potential of about $-$ 1.2 kV, in the absence of neutral beam injection. Finally, momentum diffusivity was modeled and found to be in the range of 1×10^4 – 5×10^4 cm^2/s, about two orders of magnitude above the expected neoclassical value.

Similar measurements were made on the Torus II tokamak using a six channel grating polychromator, looking at the Doppler shift of the He II (4685.75 Å) line[62]. The Torus II team found that the plasma had an average toroidal rotation velocity of 1.6 km/s in the co-current direction. They also measured the damping of the rotation in time. It was found that 10 μs after the heating phase, the plasma rotation had dropped below detectable levels. These experiments also used the measured poloidal velocity to calculate the radial electric field (E_r). Estimates for E_r were made from neoclassical theory; based on data values of 2.5 – 5 kV/m were found. Toroidal rotation decay time scale was found to be very short, ($\tau \sim 10\ \mu s$)

In the JFT-2 tokamak V_ϕ was measured using Doppler shifted lines of Ti XIV , O VII , and C V [63]. These three lines gave a three point toroidal rotation profile with measurements at r/a of 0.2, 0.4 and 0.6, (Ti, O and C, respectively). $V_\phi \sim$ 10 km/s with relatively flat profiles were measured during $\sim$ 1 MW of NBI power.

Interestingly, JFT-2 concluded that rotation was not relevant to transport processes in their tokamak[63].

In the TM–4 tokamak toroidal and poloidal rotation velocity profiles were measured using Doppler shifted lines of C V , C III , O V , and H_β[64]. V_θ profiles were found to be positive and hollow, peaking around r/a $\simeq$ 0.7, at $V_\theta \simeq 2\ km/s$. V_ϕ profiles were also found to be hollow. The profile shape was both positive and negative, peaking at $V_\phi \simeq 4\ km/s$ around r/a $\simeq$ 0.72, with a minimum near the magnetic axis, of $V_\phi \simeq$ -7 km/s. Both poloidal and toroidal rotation velocities were near zero at the edge. Rotation velocities were found to be significantly lower than expected based on neoclassical theory. The toroidal momentum damping time was calculated to be less than 3 ms, $\tau_\phi \equiv \tau_t \leq 0.002\ s$.

3.4 Beam Based Toroidal Rotation Measurements

High resolution x-ray spectroscopy is not the only method of measuring toroidal rotation. When a tokamak is outfitted with a complement of neutral beams, it is fairly easy to make measurements of both the poloidal (V_θ) and toroidal (V_ϕ) plasma rotation. Plasma rotation is often measured using charge exchange recombination spectroscopy (CXRS); it has been well established as a rotation measurement method[54, 65–71].

The neutral beam provides electrons for the impurities to charge exchange with. These recombinations emit characteristic photons that are then collected and interpreted. The charge exchange process[8] has an energy dependent cross-section. The relative velocities of the particles and the beam and the view angle can influence the measurement.

CXRS uses the light emitted from the recombination of the hot plasma impurity ions with the electrons from the neutrals injected by the beam. An intrinsic impurity in the plasma, (C, O, &c) is often used to make CXRS measurements. These impurity ions then exchange charge with the neutrals from the injected beam, and emit at a characteristic wavelength. These spectral lines are then resolved using a spectrometer, conveniently enough, often in the visible or near UV region.

Once the spectra have been gathered and the effects from the view location have to be taken into account, the rotation velocity, impurity density, and impurity temperature can be unfolded from the spectra. Since the charge exchange process is energy dependent, the relative energy between the beam and the background ions is important. Stated differently, ions with velocity components in one direction longitudinally along the beam, will contribute to the spectra differently than ions with velocity components longitudinally in the opposite direction. In general the CXRS spectra shape will not be symmetric, and these asymmtries in line shape need to be accounted for.

From these spectra, one can gather information about the impurity density, the impurity temperature, and the impurity rotation velocity[72, 73]. With certain assumptions these can be generalized to the majority ions. (see Chapter 2: Rotation Theory.)

It is important to note that beam based measurements can be highly perturbative. Beams are more often than not a substantial source of momentum to a plasma.

The alternative to measurements made with heating beams is to use a lower current diagnostic neutral beam (DNB). C-Mod has been fitted with just such a beam. The DNB injects hydrogen neutrals radially into the machine, the light emitted by the ionizing of the beam can then be used for diagnostic purposes. There are three main diagnostics associated with the beam: beam emission spectroscopy (BES)[74, 75], motional stark effect (MSE)[76–78], and charge exchange recombination spectroscopy (CXRS), which has been mentioned above. BES measures density fluctuations by looking at the fluctuations in the power intensity of emitted light. The MSE measures magnetic field orientation (B_T, B_R, B_V), or equivalently, q. It is set up to have multiple view chords, so it is possible to measure a profile of the magnetic field orientation, or a q – profile.

3.4.1 Beam Measurements on DIII-D

Many, many measurements of plasma rotation and rotation profiles have been made on the Doublet III D (DIII-D) tokamak [67, 69, 70, 79–85]. DIII-D uses CXRS mea-

surements made with a 75 keV hydrogen neutral beam to look at O and He impurities. The DIII-D team is and has been able to measure toroidal rotation velocities at six different radial locations both on the high and low field sides of the plasma. Values of angular speed[2] typically between about 0.0 at the edge of the plasma to about 1 $\times$ 10^5 rad/s ($\sim$ 140 km/s) at the magnetic axis have been measured. The profile shapes have generally been peaked, due to the momentum in the beam. The absolute magnitude of the angular speed (likewise V_ϕ) generally about 6 $\times$ 10^4 rad/s – 1 $\times$ 10^5 rad/s. The values found for the momentum confinement time were quite close to the energy confinement times, ($\tau_\phi \sim \tau_E$). Measurements of V_ϕ, V_θ and E_r have been made at the H–mode transition. DIII-D is also credited with being the first experiment to see the ITB.

During L–mode, the rotation profile in DIII-D is slightly peaked from the axis out to about $r/a \sim 0.4$ and mostly flat outside of that, co–current everywhere. During ELMing H–mode discharges, the profile is quite similar, to the L–mode case in both shape and magnitude. During ELM–free discharges, the profile shape is more peaked, out to about $r/a \sim 0.6$, and the magnitude is about twice as large as the L–mode.[85] These discharges all have relatively large amounts of input beam power on axis.

The measurements discused here represent just a fraction of those made on DIII-D. In many respects work done at DIII-D has led the field in rotation research and measurements. Reference [84] is a comprehensive treatment of measurements made over the last ten years. Thousands of discharges have been included in this study. Two of main conclusions from this work are: momentum transport seems anomolous much greater than predicted by neoclassical theory; and that the correlation between toroidal momentum and ion thermal energy transport implies that the same physics governs them both.

[2]Toroidal rotation velocity V_ϕ is the product of angular speed (Ω_ϕ) and major radius (R) or $\Omega_\phi = V_\phi/\mathrm{R}$.

3.4.2 Beam Measurements on JET

The JET team has also made measurements of plasma rotation using CXRS[86]. Using visible light from a C VI transition, the team has been able to measure the ion temperature and the rotation velocity in up to twelve spatial locations and with 100 ms time resolution. Rotation frequencies as high as $1 \times 10^5\ rad/s$ ($\simeq 300\ km/s$) have been measured in plasmas with 20 MW of beam power and 2 MW of ICRF power. Various profile shapes were found, including peaked and fairly flat, depending on the heating method.

3.4.3 Beam Measurements on TFTR

During some of the TFTR "super shots" (extremely good confinement shots) V_ϕ measurements were made using CXRS. TFTR was using up to 15 MW of neutral beam heating ($E_{inj} \simeq 105\ keV$). Observing lines of carbon, 17 point toroidal rotation profiles were measured. The rotation profiles were found to be highly peaked off axis, due to the beam injection. Maximum rotation velocities of up to 500 km/s were found[87]. Finally, momentum diffusivity and effective particle diffusivity were about the same, ($\chi_\phi \sim \chi_{eff}$).

3.4.4 Beam Measurements on ASDEX

In ASDEX toroidal rotation measurements were made via CXRS using O VIII and C VI impurities[88]. Profiles with 5 radial points have been measured, and profiles have been found to be peaked. Maximum rotation frequencies of $1 \times 10^5\ rad/s$ ($V_\phi \simeq 120\ km/s$) have been measured in plasmas with up to 2 MW of input NBI power. Finally, momentum diffusivity and ion diffusivity were about the same, ($\chi_\phi \sim \chi_i$).

3.4.5 Beam Measurements on JT-60 U

Toroidal rotation measurements have been made in the tokamak JT – 60U, in plasmas with high power ($\sim$ 20 MW) tangential and near perpendicular NBI[89]. Measurements are made using a near perpendicular diagnostic beam. Using CXRS, looking

at carbon impurities, they have been able to measure a 15 point profile of the toroidal rotation velocity. Peaked profiles, with maximum rotation velocities of around 250 – 300 km/s have been measured[90]. It was found that plasmas heated only by near perpendicular beams would rotate in the counter–current direction, at a velocity of about 50 km/s. Plasmas that were heated with lower hybrid waves were found to rotate in the co–current direction[89]. ITBs were formed, and measurements of the radial electric field, (E_r) were made. Finally, momentum diffusivity and ion diffusivity were about the same, ($\chi_\phi \sim \chi_i$).

3.4.6 Beam Measurements on Other Machines

Many other devices have also made measurements of plasma rotation using beam based diagnostics. Two of note are: PBX – M [91] and ISX – B [92]. On PBX – M, V_ϕ of 400 km/s was measured with less than 5 MW of neutral beam power. The profile shape was found to be highly dependent on the configuration of the heating beams. Momentum diffusivity and effective particle diffusivity were found to be about the same, ($\chi_\phi \sim \chi_{eff}$). The momentum confinement time, (τ_ϕ), was found to vary between 0.039 and 0.147 s. On ISX – B, the heating beams used were balanced, so in theory there was no net input of momentum. During Ohmic discharges the rotation was found to be between 10 km/s in the co–current direction and 10 km/s in the counter–current direction. During balanced beam configuration the rotation was found to be between $\sim$ 25 km/s in the co–current direction and $\sim$ 25 km/s in the counter–current direction. Momentum confinement times of $\sim$ 0.010 – 0.050 s

3.5 Chapter Summary

Many previous high resolution x–ray spectroscopic and toroidal rotation measurements have been made on C–Mod and on other tokamaks, with varying degrees of success. Some information about measurements on various machines has been summarized in Table 3.2.

High resolution x–ray spectroscopic measurements have been mostly single view systems. C–Mod originally had one tangentially viewing and five radially viewing

Tokamak	Instrument	V_ϕ (km/s)	Profile (# pts.)	Heating	Notes
C-Mod	HIREX	100	3	ICRH	No **p** Input
LT-3	Doppler (UV)	1		Ohmic	Early
TFTR	X–ray Spect.	150	1	NBI	
	CXRS	500	17	NBI	15 MW!
JET	X–ray Spect.	100	1	NBI	
	X–ray Spect.	120	1	NBI & ICRH	
	X–ray Spect.	$\Delta V_\phi = 30$	1	ICRH	
	CXRS	300	≤ 12	NBI & ICRH	20 MW & 2 MW
DIII-D	CXRS	86	6	NBI	
JT – 60U	CXRS	300	15	NBI	
	CXRS	50	15	$\perp$ NBI	Counter-I_P
PBX-M	CXRS	400	20	NBI	

Table 3.2: This table summarizes the most important previous measurements of toroidal rotation made on various machines. They are listed by: tokamak the measurements were made on, the type of diagnostic, maximum rotation velocity, number of points in their profile, the heating scheme and some notes.

spectrometers with slight angles to their views. These angles were so small that they made the error in the points measured with radially viewing spectrometers quite large.

High resolution x–ray spectroscopic measurements have been made on JET, TFTR, PDX and DITE. Some of the very early measurements using bent crystals were made on DITE. The maximum rotation velocity on record was made on TFTR (500 km/s), with 15 MW of NBI. A two point rotation profile using two lines of ionized Ti was measured on PDX.

Some of the earliest rotation measurements were made on tokamaks by other spectroscopic means, specifically LT–3. PLT held the record for the day with $V_\phi \simeq 120\ km/s$. This measurement was made using lines of C and Fe.

Thus far, the most detailed toroidal rotation measurements have been made with neutral beams on TFTR, JET and DIII–D. Multi point profiles have been measured, and in general data have been found to agree with theory quite well. It is important to remember that beam based measurements are highly perturbative in terms of the net input of momentum, even if a balanced beam configuration is used.

(This page intentionally left blank.)

Chapter 4

The Spectrometer

This chapter will detail the experimental setup, including the physics of the measurements and the spectrometer.

4.1 Physics of X–Ray Spectroscopy

4.1.1 Doppler Shift

When a wave source is moving, its velocity has an effect on the wavelength of the emitted oscillation. This is true of all waves: light, sound, &c.

The non–relativistic approximation to the shift in the wavelength is determined by the equation:

$$\frac{\Delta\lambda}{\lambda_0} = \frac{v}{c} \tag{4.1}$$

where $\Delta\lambda$ is the wavelength shift, λ_0 is the rest wavelength, v is the velocity of the source and c is the speed of propagation of the wave. Note: if $v \to 0$, $\Delta\lambda \to 0$, as it should. Also, if $v > 0$ (< 0) then and the shift will be to longer (shorter) wavelength, $\Delta\lambda > 0$ (< 0), which implies the source is moving away from (towards) the observer. Figure 4-1 shows a Doppler shifted spectrum. The shift in the spectrum shown ($\sim$ 0.5 mÅ) corresponds to a source velocity of $\simeq +$ 43 km/s.

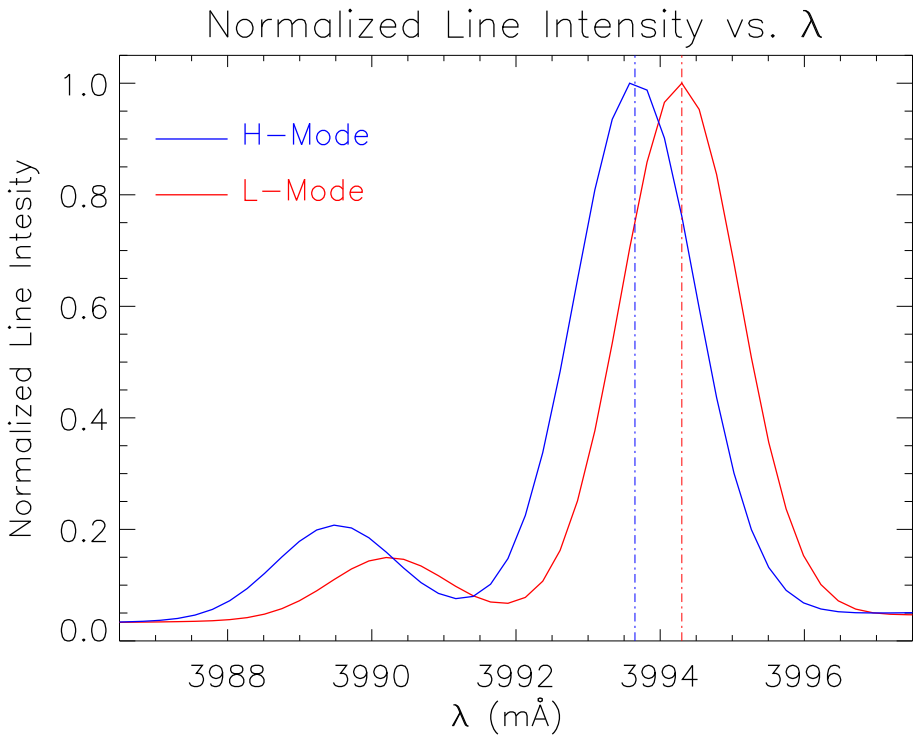

Figure 4-1: A sample spectrum of the Ar^{16+} forbidden line, (**z**) from the HIREX array. During the L–mode phase of plasmas the rotation is minimal, (red curve), during the H–mode portion of a discharge the plasma starts to rotate very quickly, here is a demonstrative Doppler shifted H–mode spectrum (blue curve) over plotted on an L–mode spectrum, to show the approximate magnitude of the shift. This shift corresponded to a rotation velocity of + 43 km/s, blue shifted. Note: the intensities of the two curves have been normalized to the same magnitude. The line intensity in L–mode is significantly lower than that during the H–mode portion of the discharge.

4.1.2 Doppler Broadening

Any gaseous material with a finite temperature has some distribution function ($f(x, v, t)$), i.e. the particles have a distribution of velocities, and thereby thermal speeds; for a Maxwellian distribution it is of the form:

$$f(v) = n\left(\frac{m}{2\pi kT}\right)^{1/2} \cdot \exp(-\frac{1}{2}mv^2/kT) \tag{4.2}$$

where: n is the number density of the particles, m is the particle mass, kT is the temperature, v is the particle velocity.

The Doppler shifts of the line radiated by each of these particles, when looked at as a whole, sum to broaden the line[1]. This is Doppler Broadening. If we now write Eq. 4.1 in terms of the measured wavelength and the rest wavelength, and solve for v we have:

$$\frac{\Delta\lambda}{\lambda_0} + \frac{\lambda_0}{\lambda_0} = \frac{v}{c} + 1 \qquad \Rightarrow \qquad v = \frac{c}{\lambda_0}(\lambda - \lambda_0) \tag{4.3}$$

where: $\lambda = \Delta\lambda + \lambda_0$, is the measured wavelength. We now substitute Eq. 4.3 into Eq. 4.2 and we find:

$$f(\frac{c}{\lambda_0}[\lambda - \lambda_0]) = n\left(\frac{c^2 m}{2\pi\lambda_0^2 kT}\right)^{1/2} \cdot \exp\left[-\left(\lambda - \lambda_0\right)^2 / \left(\frac{2\lambda_0^2 kT}{c^2 m}\right)\right] \tag{4.4}$$

This is the equation for the shape of a spectral line of a material at temperature kT. This derivation is covered quite nicely, in some detail, in chapter 6 of Ref. [8].

4.1.3 Argon Impurity Injection

Argon is the impurity chosen to inject to make these measurements, in the temperature range of interest it radiates in an appropriate range of the x–ray spectrum. The spectrometer on C–port, viewing on the midplane, through the center of the plasma, looks at the Lyman α doublet of hydrogen–like argon ($Ar^{17}+$), see Table 4.1. This spectrum is shown in Fig. 4-2. The spectrometers in F–port and K–port, tangentially viewing at about $r/a \sim 0.3$ and $r/a \sim 0.6$, respectively, look at the **z**(the forbidden) line and the **w** (resonance) line, of helium–like argon. The three spectrometers in B–port, radially viewing, look at the **z**(the forbidden) line and the **w** (resonance) line of He–like argon, see Table 4.1. This spectrum is shown in Fig. 4-3. In fitting the spectra, the satellite lines, (*e.g.* **k**, **q**, **r**, *etc.* of Fig 4-3), need to be accounted for. Generally, a small portion of the measured spectrum will be analyzed with a fit to one line and just one or two satellites.

Expected line intensities for He–like Ar have been calculated in Appendix A.

[1]Of course, the line is made up of a statistically significant collection of photons, from the individual particles, each of which has it's own Doppler shift.

Charge State	line	Transition	λ_0 (mÅ)
Ar^{16+}	**z**	$1s^2\ ^1S_0$ – 1s 2s $^3S_1$	3994.4
Ar^{16+}	**w**	$1s^2\ ^1S_0$ – 1s 2s $^1P_1$	3949.4
Ar^{17+}	Ly α_1	1s $^1S_{\frac{1}{2}}$ – 1s 2p $^2P_{\frac{3}{2}}$	3731.1
Ar^{17+}	Ly α_2	1s $^1S_{\frac{1}{2}}$ – 1s 2p $^2P_{\frac{1}{2}}$	3736.5

Table 4.1: The transitions of interest for these measurements, for H – like and He - like Ar.

To make this calculation requires some detailed information about rate coefficients and and charge state densities, calculations related to these are in Appendix B and Appendix C, respectively. In the core of the plasma the temperature range is such that Ar^{17+} is generally the most abundant. Further out in the plasma the temperature range is generally such that Ar^{16+} is the most abundant.

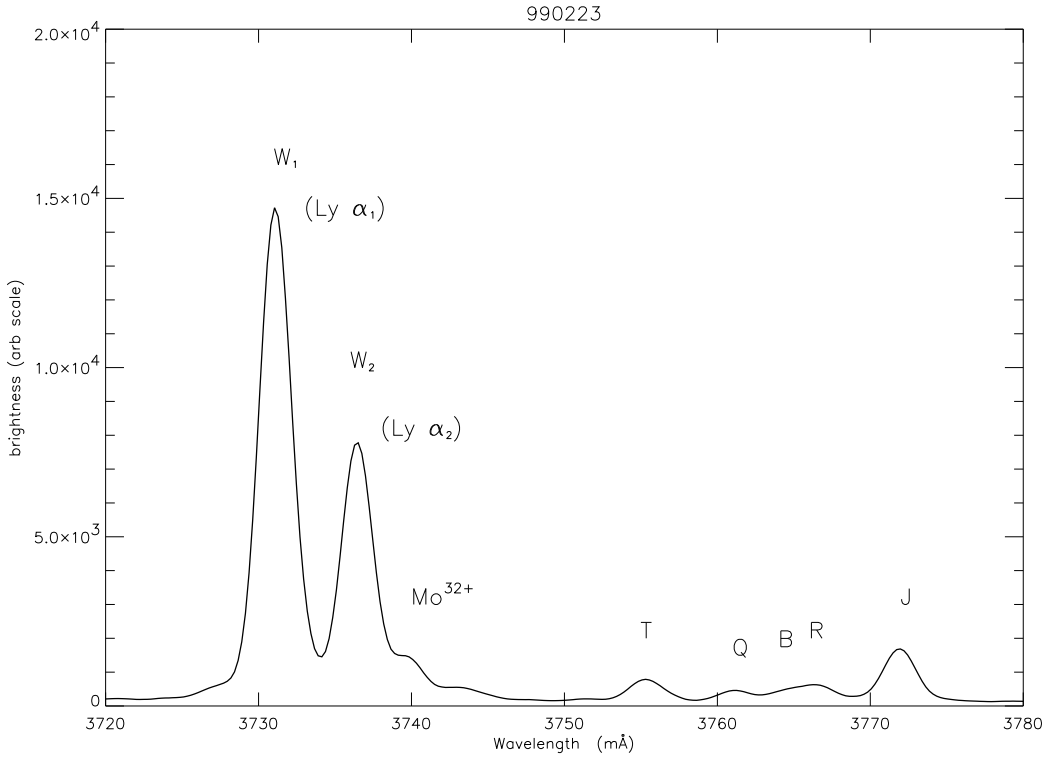

Figure 4-2: A spectrum for H–like Ar, (Ar^{17+}).

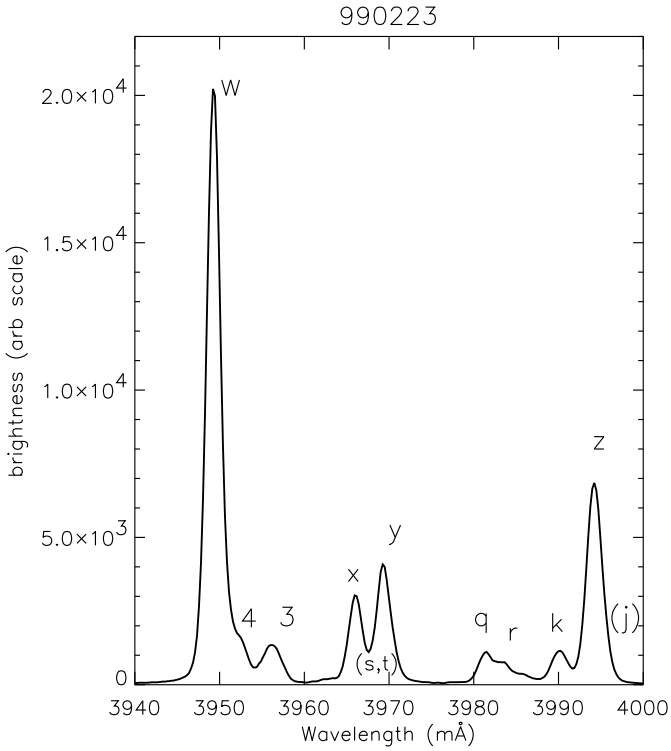

Figure 4-3: A spectrum for He–like Ar, (Ar^{16+}).

4.2 Experimental setup

4.2.1 Bragg Diffraction

Bragg diffraction is the fundamental physical mechanism at work in this spectrometer. Figure 4-4 is a sketch of the process of Bragg diffraction.

The condition for Bragg diffraction is:

$$n\lambda = 2d\sin(\theta) \tag{4.5}$$

where: n is an integer, λ is the wavelength of the light being scattered, d is the spacing between atoms of the crystal lattice, and θ is the angle of incidence, normal to the surface of the diffracting structure[2]. Diffraction requires that d be of order λ,

[2]In this spectrometer, the angle of incidence must still equal the angle of reflection. However, constructive interference will occur only for particular angles as given by the Bragg condition, Eq.

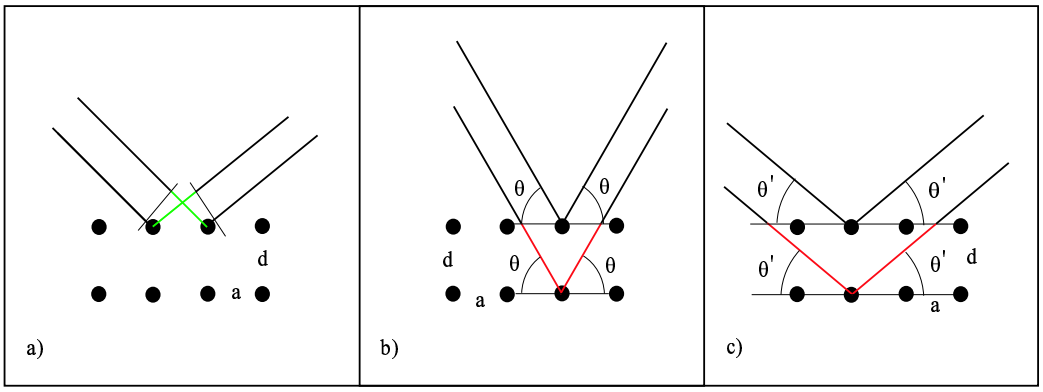

Figure 4-4: A sketch of conditions for Bragg diffraction. When incident light is scattered from two atoms from the same row, separated by distance a (4-4-a) there is no net difference in the path lengths of the radiation, however when the light is scattered from two atoms in different rows of the lattice separated by distance d (4-4-b) and (4-4-c), there is an increase in the length of one path but not the other. This increase is $2d \cdot \sin(\theta)$, and when this equals an integer number of wavelengths, there is constructive interference. Figure 4-4-b is for a shorter wavelength and Figure 4-4-c is for a longer wavelength. (In this figure the angles θ and θ' are grossly exaggerated.)

($\sim$ Å, for x–rays) hence the atomic periodicity of a crystal is used as the diffraction "Grating".

4.2.2 General Description

HIREX is a von Hamos geometry[93] high resolution x-ray spectrometer system. Figure 4-6 is a sketch of the geometry. The incoming x–rays are collimated through a slit, they are then incident upon the crystal. The crystal is cylindrical, (*i.e.* flat in the plane into which the wavelength is separated and bent in the direction perpendicular to this plane,) see Fig. 4-6.) This bending generates a focusing of the incoming x–rays onto the detector, for improved collection. The main advantage of von Hamos geometry is the compact size. Using a quartz[3] crystal as the diffraction element, one is able to perform spectroscopic analysis on the emitted x–ray radiation from C–Mod

4.5. One could imagine that the condition of path length difference being equal to a integer wavelength, could also be met by having different angles of incidence and reflection. This is indeed the case, however it will not be discussed here because it is not the method of crystal diffraction being used here.

[3]See the §4.2.4 for more about the quartz crystal.

[51, 52]. By comparing relative line intensities for the various charge states, one can determine the electron temperature. The widths of very strong lines can be used to determine ion temperature [94]. Further, by looking at the Doppler shift for a given spectral line the relative motion of the impurity that generated that line can be measured.

The HIREX Array was made up of six different spectrometers. Each of these spectrometers has two arms, an entrance arm, and a detector arm, Figs. 4-5 and 4-6. The arms are pumped to pressures in the mTorr range using a mechanical roughing pump[4]. The entrance arm "looks" into the plasma, through a small slit and a beryllium window, (§4.2.3). The detector arm comes off the entrance arm, at an angle determined by the Bragg condition (§4.2.1) of the quartz crystal, (§4.2.4). Located at the intersection of the two arms is the crystal. At the end of the detector arm is a delay line proportional counter detector,(§4.2.5). The signal from the detector is then processed with some electronics,(§4.2.6), and the data are stored and interpreted with a computer.

4.2.3 Beryllium Windows

For various logistical reasons it is neither wise nor necessary to have the spectrometer vacuum system tied into the same vacuum system as the main vacuum chamber. First, the main chamber of the tokamak requires Ultra High Vacuum (UHV), pressure $< 1 \times 10^{-8}$ torr, along with which goes very strict requirements for materials, seals and cleanliness. Second, if for some reason the vacuum is compromised in the spectrometer, the main chamber and the entire experiment would suffer needlessly. Further, the maintenance schedule would be tied to that of the main chamber. As a consequence of this, opportunities to repair and upgrade the spectrometers would be lost. Thus, a window is required.

Very high purity beryllium was chosen for the window. High purity beryllium will allow the passage of x-rays, without significant loss and will still make a very good UHV seal,(See Appendix D).

[4]Calculations of x–ray attenuation vs. energy and pressure can be found in Appendix D.

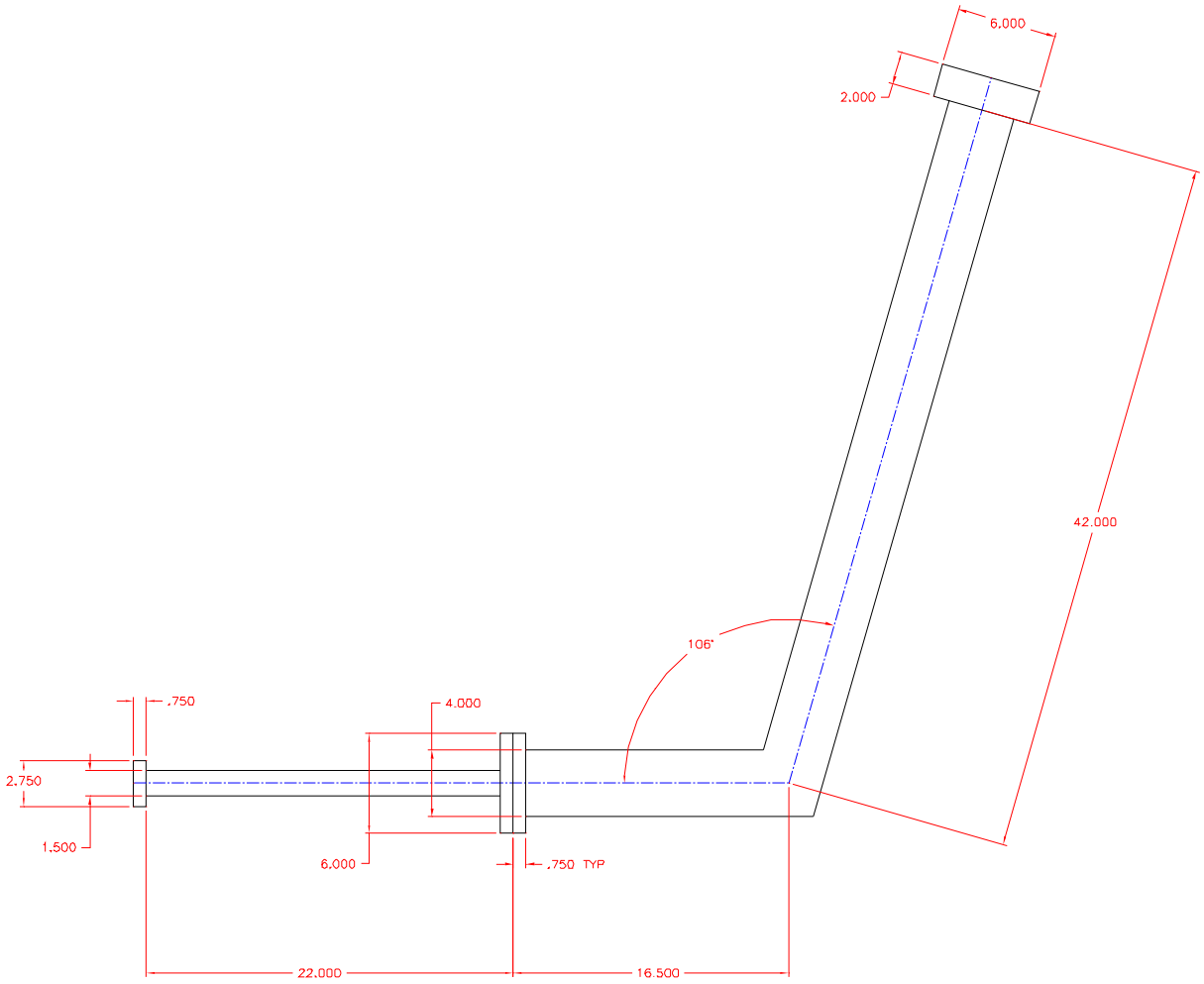

Figure 4-5: The spectrometer geometry, from a top view. Depending on the sense, (i.e. right handed or left handed,) of the spectrometer, its geometry will either look like this, or a mirror image of this. The relative angle of the arms, listed as 106° can be changed to sweep through different wavelengths. The bend in the spectrometer is made of an angled vacuum pipe and a bellows to allow the arm to swing. This arm is controlled by an electronic actuator and the angle is recorded by a position sensitive potentiometer.

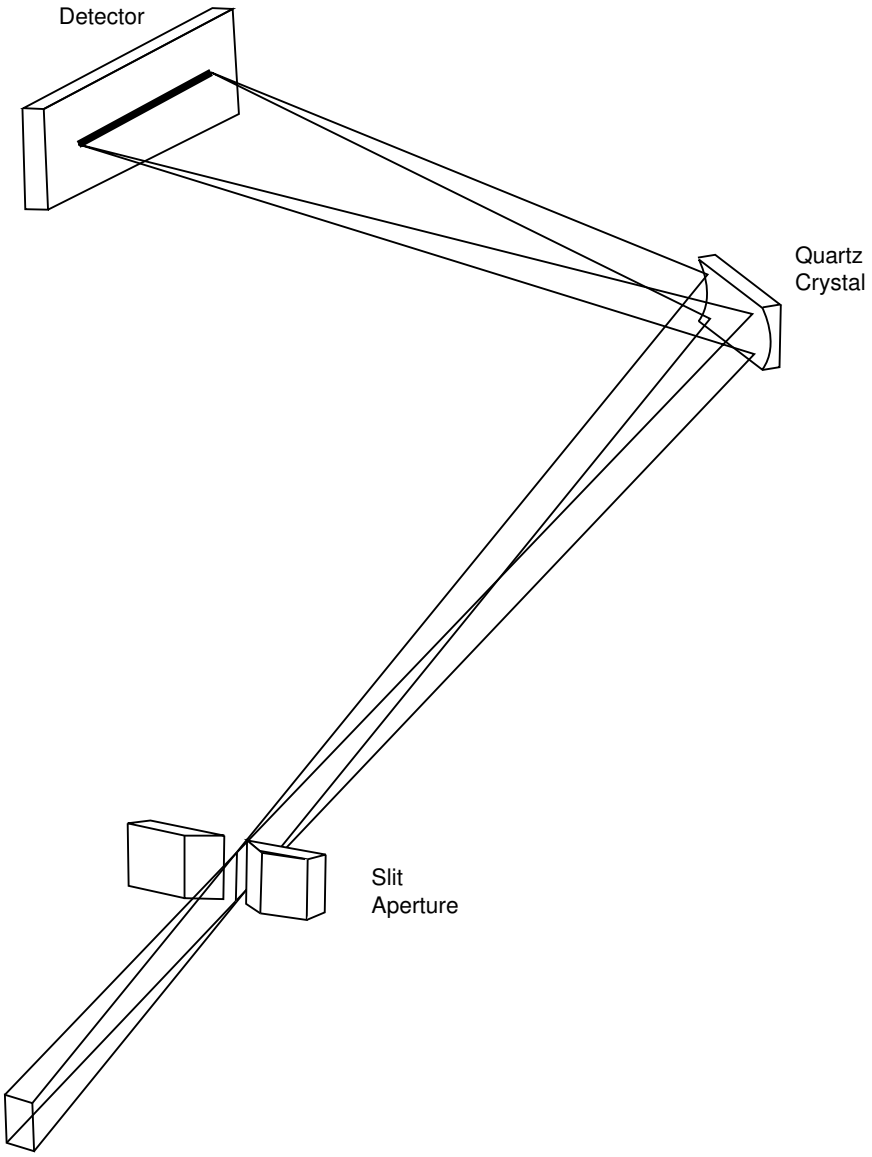

Figure 4-6: Drawing of the von Hamos spectrometer geometry, notice the crystal is curved (grossly exaggerated here), leading to a focusing of the incoming x–rays.

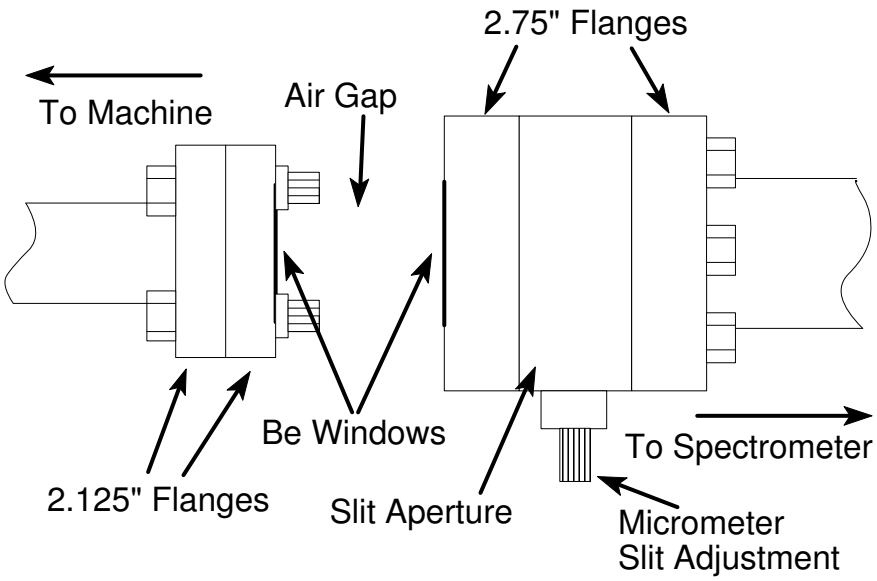

Figure 4-7: The incident x-rays travel out of the machine through a small flange and a Be window. They then cross the air gap, made as small as possible to reduce attenuation, and then into the spectrometer, through a second Be window.

Beryllium has extremely high strength to weight ratio, and very low modulus of elasticity and very good rigidity [95]. Beryllium's material properties allow windows to be made very thin to pass x–rays, yet still withstand 101.4 kPa (760 torr) pressures. Two of these windows each 0.002 inches thick were used for each spectrometer. These windows are epoxied onto a stainless steel flange and then mounted to the main vacuum vessel and to the spectrometer face, see Fig. 4-7. The two flanges are aligned and held separated by a Teflon spacing plug, not pictured in Fig. 4-7, for clarity[5]. This spacer also keeps the spectrometer and the machine electrically isolated.

4.2.4 Quartz Crystal

Quartz was chosen as the crystal for this spectrometer. The spectrometer was designed to cover a wide range of wavelength, (2.8 Å– 4.0 Å). It was desired that the spectrometer arms be kept at an angle in the range (100° – 140°), while the Bragg

[5]Both Be and air attenuate x–ray photons. It turns out that the attenuation is quite small, calculations of attenuation vs. energy have been made in Appendix D for both air and Be.

condition (Eq. 4.5) was to be satisfied, for the relevant Ar transitions. This range of angles would insure the spectrometer is both compact and conveniently shaped to get close to the machine. These conditions then require that the inter-atomic spacing of the crystal, (d), be in the range 3.11 Å$< d <$ 4.09 Å. The $10\bar{1}1$ plane of a quartz crystal has an inter-atomic spacing of 3.3435 Å[96]. Quartz also has excellent resolution, quite good reflectivity and is stable over long time periods. Thus, the quartz crystal was chosen.

4.2.5 Proportional Counter Detector

To measure the spatial location of the incoming x–rays after dispersion by the crystal, and hence the wavelength, a position sensitive proportional counter detector is used[97–100]. The detector is made up of small chamber of pressurized krypton and ethane, another Be window, a multi-wire anode plane, a delay line cathode winding, and the associated electronics, (see §4.2.6).

When an incident x-ray enters the detector chamber, through the Be window, it almost immediately collides with a Kr atom, (Fig. 4-8-a). This collision liberates an electron which is then accelerated towards the anode wire, (Fig. 4-8-b). This accelerated electron causes a cascade of electrons, towards the anode wire, where they are collected. This charge on the anode line capacitively couples to the delay line cathode coil[98]. This image pulse then travels in each direction through the coil to be counted and compared at either side of the detector, (Fig. 4-8-c). The delay line is necessary to slow down the pulse to a time scale appropriate for the time to digital converter (TDC).

4.2.6 Electronics

Figure 4-9 is a rough schematic of the layout of the electronic components used to process the signal out of the detector. This section will follow the path of the signal through the electronics.

Each detector needs high voltage ($\sim 2\ kV$), and four fast amplifiers, two for each

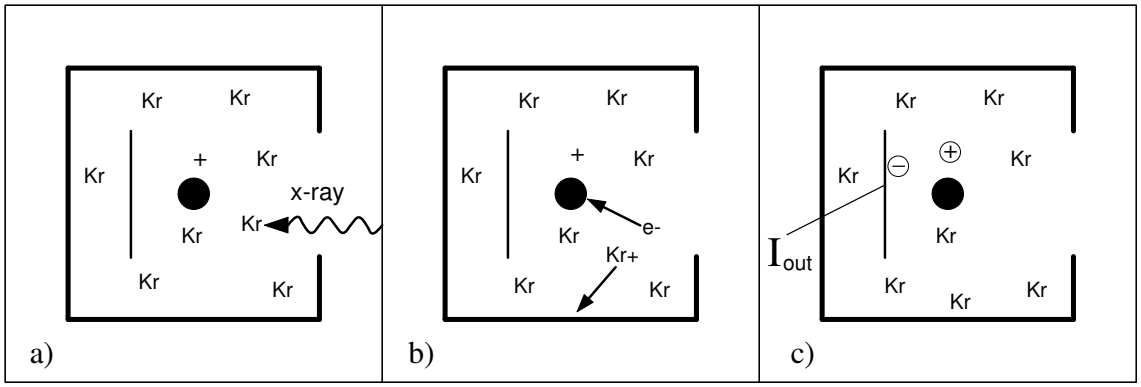

Figure 4-8: Incident x–rays enter the detector (4-8-a) and collide with a Krypton atom. The Kr atom is ionized, (4-8-b) and the electron(s) travels to the anode line(s), which is at high voltage. When the electrons reach the line, they send a small current pulse (4-8-c) in each direction, (via a delay line cathode plane). In this cartoon, the line has been simplified to only a single wire, actually it has many loops.

end of the delay line. The detector has a characteristic impedance of $\sim$ 200 Ω.The electronics all have characteristic impedance of 50 Ω. Thus, each side of the detector has a 200 Ω to 50 Ω transformer, followed immediately by a set of fast amplifiers and attenuators.

Physically, the amplifiers need to be placed as close as possible to the detectors to minimize signal loss and signal distortion. Each signal comes out of the transformer and is amplified by the first fast amplifiers, (fixed gain: $-$ 200). The signal is then inverted and just slightly attenuated[6]. It then passes through the second set of fast amplifiers. The final pulses out of the amplifiers are between $-$ 2 V to $-$ 5 V; they have a $\sim$ 2 ns rise time and a 10 ns decay time. The pulse shapes are determined by the detector itself. To measure the desired wavelengths we use 156 ps time resolution, the fastest setting on our electronics. These pulses then travel from the physical location of the spectrometer, (C–port, F–port, &c.) to the main electronics rack near B–port.

The most important part of the measurement is to measure precisely the delay time

[6]The fast amplifiers are fixed gain, a single amplifier is not enough amplification and two amps are too much. The attenuator solves this problem.

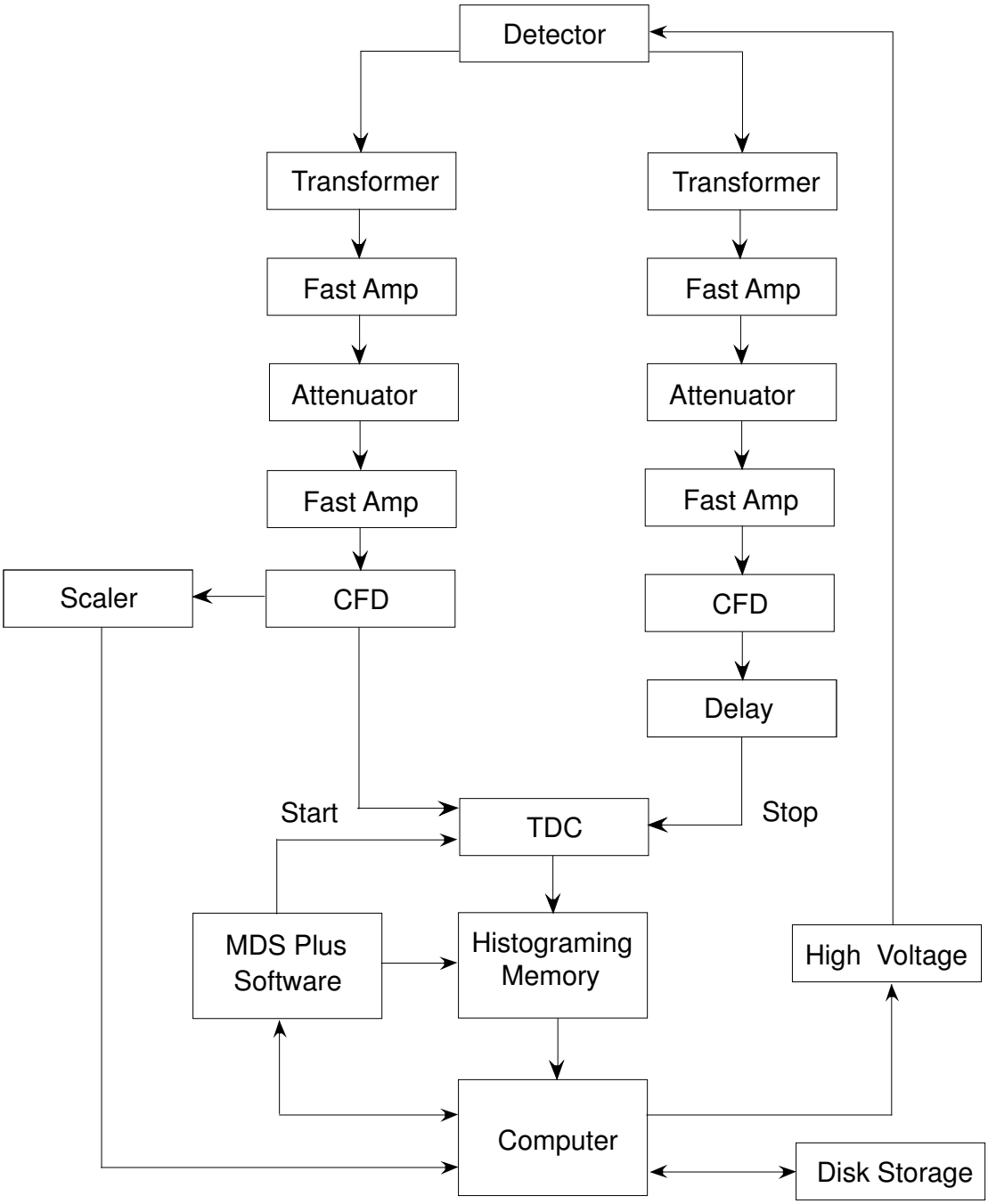

Figure 4-9: Schematic of data acquisition electronics components, for the spectrometers.

between the arrival of the two pulses, one from each end of the detector. However, if the pulses are of different shapes, which is almost certainly the case, we need some way to take this into account properly, and avoid confusion in the arrival times. To solve this problem the pulses are fed into a constant fraction discriminator (CFD). The CFD splits the incoming signal into two parts. One part is delayed and subtracted from a fraction of the undelayed signal. The resulting bipolar constant fraction signal has a baseline crossover that is almost entirely independent of the input signal height and shape[12]. The point of zero crossing is then used to locate precisely the signal in time. These zero crossings are then used to generate logic pulses. The CFD also sends a logic signal to a scaler, to record the time history of the total count rate.

The logic pulses are then sent to a time to digital converter (TDC). One pulse, from the given spectrometer, is used as the start trigger of the TDC, while the other is the stop trigger. The stop trigger passes through a $\sim 100\ ns$ delay line[7] to insure that it will not arrive before the "start" pulse. The time difference between the two signals is then recorded in a histograming memory module. In this manner, 1024 channel spectra are taken every 50 ms for the spectrometers on B–port, F–port and K–port, and 512 channel spectra every 20 ms for the spectrometer on C–port.

Once the data are taken, and processed by the electronics, they are fed into a computer where they are reduced. The reduced data are then stored to disk, where they can be accessed and further processed via MDS Plus software.

One of the greatest difficulties in making these measurements has been keeping out stray RF noise. The ICRF system operates at $\sim 80\ MHz$, ($\sim 2\ ns$ period.). This is precisely the right frequency to seriously distort the pulses out of the detector and amplifier, and hence the line shape. To prevent this, great lengths were gone to, to adequately shield the detectors and the transmission lines used to carry the pulse. Extensive work was also done to limit the amount of RF leakage in the ICRF system.

[7]For a pulse, the travel time along the entire delay line in the detector is just 75 ns.

4.3 Tangential HIREX

The tangential HIREX works on precisely the same design as the radially viewing HIREX spectrometers; the difference is the view of the spectrometers. Figure 4-10 shows the sight lines of all the spectrometers.

4.3.1 Vertical Displacement

The physical size and shape of the horizontal ports on C–Mod limit the range of possible view angles. It is not possible to have a view angle larger than 36° (as measured from a radius), on any horizontal port. A further constraint on the lines of sight for the spectrometers was to keep them from crossing to the high field side of the major radius. This was avoided to simplify the analysis, and to insure that location of measurement was well known. If the line of sight were to cross the major radius, the emissivity profile along the line of sight could have multiple peaks. This would confuse the location and resolution of the measurement, (more on this in Appendix A.)

By vertically displacing the lines of sight, it is insured that the peak in the emissivity of the x–rays corresponds to the desired radial location of view. Vertical displacement also allows different radii to be viewed tangentially, while still meeting the physical requirements for angle of view. To allow the spectrometers to be mounted tangentially, parallel to the midplane and still be vertically displaced, the torsion cylinder (see Fig. 1-1), had to be modified.

Fig. 4-11 shows the locations of the tangency points of the three vertically displaced, tangentially viewing spectrometers. They are labeled with the port from which they view. The radial locations mapped to the mid-plane are also shown. These three views are approximately: in the center of the plasma (C–port, $r/a \simeq 0.0$, 0.68 m), at one third of the minor radius (F–port, $r/a \simeq 0.3$, 0.775 m), and at two thirds of the minor radius (K–port, $r/a \simeq 0.6$, 0.835 m).

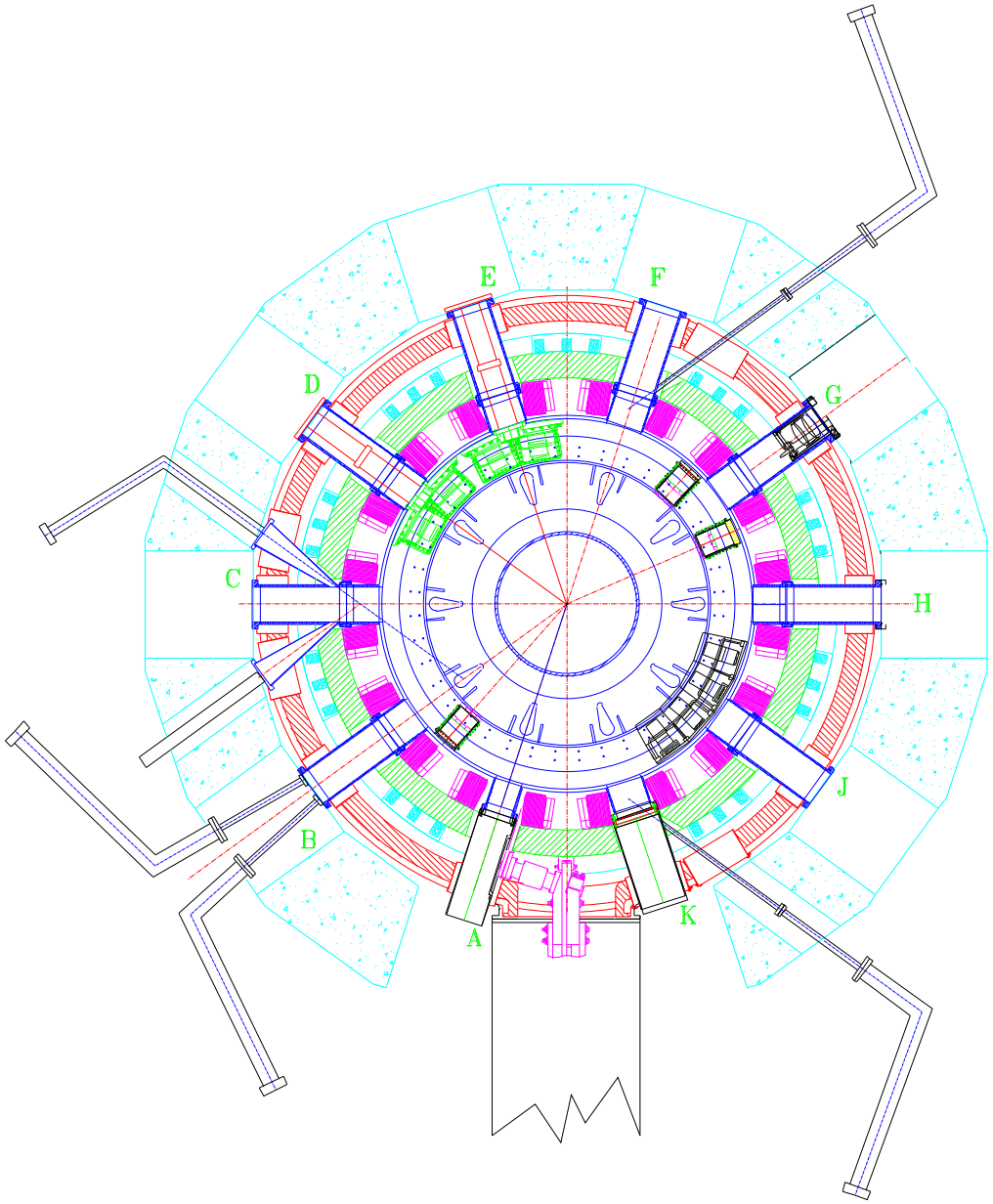

Figure 4-10: Top view of the Alcator C–Mod tokamak. The tangentially viewing spectrometers are on ports C, F, and K. The tangential spectrometers all view at the major radius of the plasma. The K–port and the F–port spectrometers are vertically displaced, viewing above the midplane.

Line	$K\alpha_1$	$K\alpha_2$	$K\alpha''$	$Ly\alpha_1$	$Ly\alpha_2$
λ (mÅ)	3741.296	3744.405	3739.1	3731.105	3736.522

Table 4.2: Potassium ($K\alpha$ doublet) Calibration lines and the argon Lyman α doublet. The $K\alpha$ lines were used for an absolute wavelength calibration for the C–Port spectrometer.

4.3.2 Flux Surface Mapping

The F–port and K–port spectrometers are mounted above the midplane; therefore it is necessary to map the location of the view along flux surfaces down to the midplane. This is done with a relatively simple IDL procedure using flux surfaces from the magnetic equilibrium, as calculated by the EFIT code[101–104]. After each shot, this mapping is made, automatically, for each spectrometer, at each 20 ms time slice throughout the discharge. These radial position data are then stored in the MDS Plus data tree. An example of this mapping can be seen in Fig. 4-11; the positions mapped to the midplane are indicated with $\times$ symbols. It is worth noting that under normal circumstances, the radii remain constant throughout the current flat top of the discharge, and unless the plasma has a very large Shafranov shift, major shaping, or some other peculiarity, the positions are as stated above.

4.3.3 Absolute Wavelength Calibration

Before the run campaign an absolute wavelength calibration was performed, for the C–port spectrometer. The calibration was achieved using three potassium $K\alpha$ lines from a KCl fluorescence source. These lines and the Ar Lyα lines have been tabulated in Table 4.2. The KCl was excited with a primary x–ray beam from a Cu–anode source[105]. The F and K port spectrometers' wavelength calibration was performed by assuming the plasma velocity profile to be flat during L–mode. This calibration using the plasma was necessary because no line source was avalible in the aicinity of the He–like lines used, (see Table 4.1)

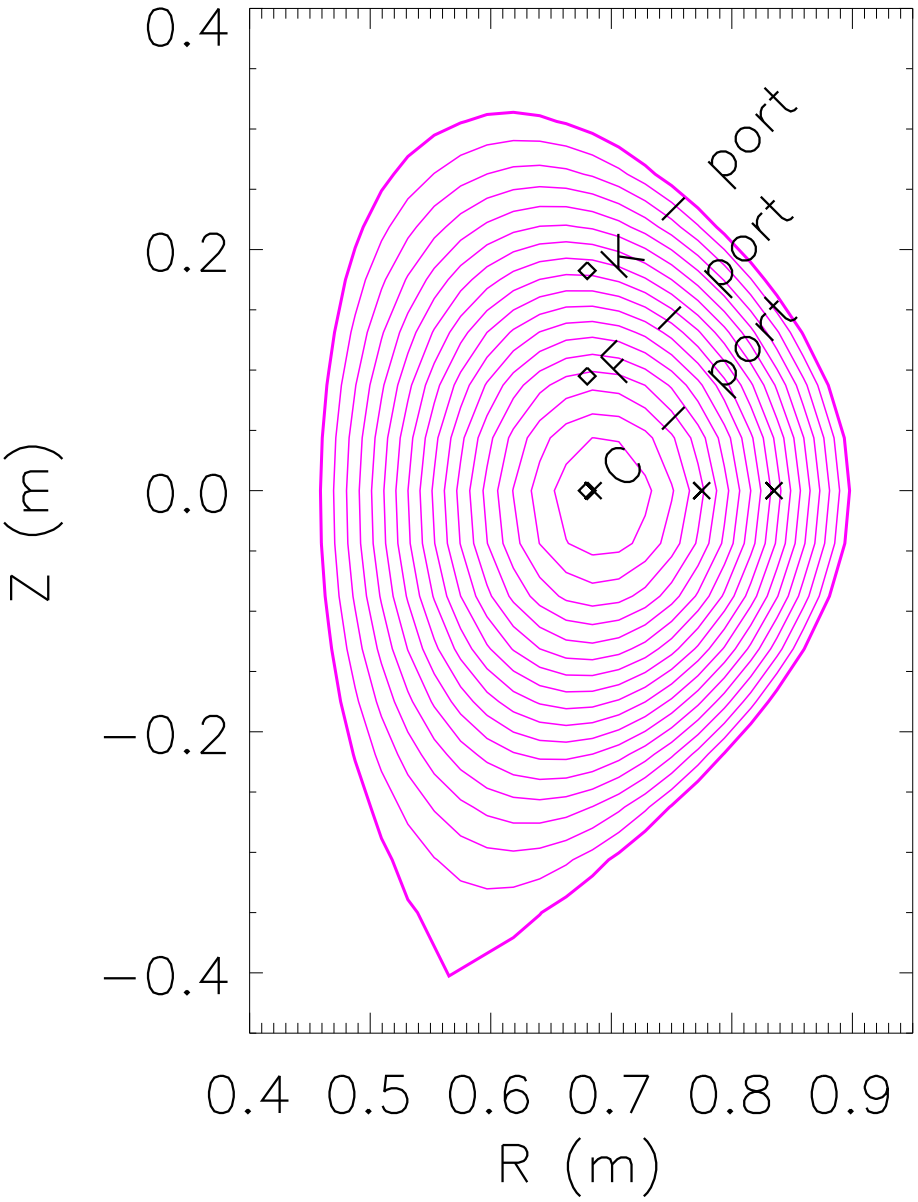

Figure 4-11: A plot of the flux surfaces for a standard shaped C–Mod discharge. The positions of the various spectrometer views at C, F, and K–ports are overplotted. The "×" symbols represent the positions mapped to the midplane.

Chapter 5

Rotation in Ohmic Discharges

Some of the data taken with the tangential high resolution x–ray spectrometer during Ohmic discharges will be presented in this chapter. It should be restated here that Ohmic discharges offer a unique opportunity to measure rotation and momentum parameters with unequivocally no internal momentum source.

5.1 Rotation Profiles in Ohmic L–Modes

In Ohmic L–modes, the rotation profiles are found to be flat, and rotating very slightly in the counter-current direction.

During the L–mode portion of an Ohmic discharge, the photon counting rate is often so small that meaningful data can not be gleaned. If the plasma parameters stay constant during the L–mode portion of the discharge, which they most often do, it is acceptable to add spectra, and use the new spectrum for the L–mode baseline[1]. Using this technique the L–mode time history of the rotation is clearly lost. However, higher confidence in the L–mode rotation velocity is achieved in return.

[1]This technique can be used in any type of discharge, provided the plasma parameters are "constant." More will be said about this in §5.2.2.

5.1.1 Toroidal Rotation in Standard L–Mode Plasmas

The standard shot in Alcator C–Mod, the most plain or least exotic, often used for fiducial comparisons, has a density of $n_e = 1 \times 10^{20}\ m^{-1}$, temperature of $T_e = 1\ keV$, $B_T = 5.4$ T, $I_p = 0.8$ MA, $P_{RF} = 0$, with lower null magnetic geometry. Data taken during this type of shot have been used to measure the standard toroidal rotation velocity profile.

The rotation profile for the standard L–mode is assumed to be flat. The inner most spectrometer rotates at about $-10\ km/s$. A typical plot of this profile averaged over an entire shot is shown in Fig. 5-1

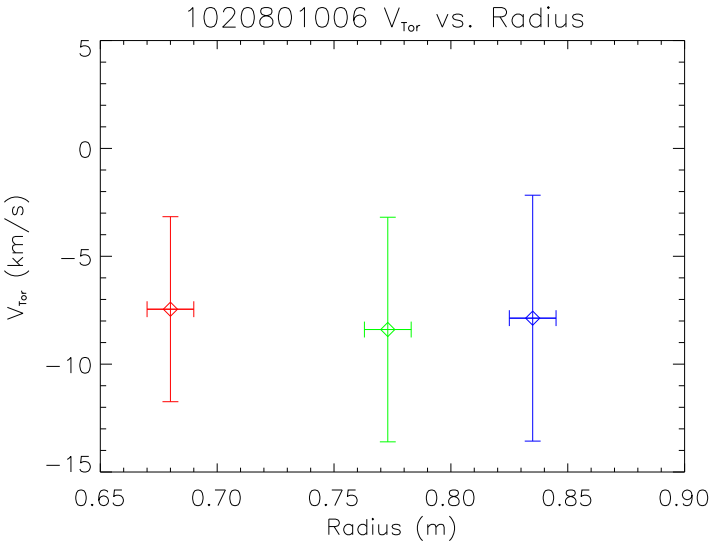

Figure 5-1: This is the most basic rotation in a generic Alcator plasma. Plasma conditions are totally average, the plasma is in L–mode, rotating slightly counter-current. These data are averaged over the length of the discharge. The counting rate was rather low, hence the large error bars.

5.1.2 L–Mode Rotation Scaling with Density

The impurity rotation velocity in a frame of reference in which the total momentum density is zero has been calculated in Ref. [16]. It depends on the plasma density (n_i), the ion temperature(T_i), the loop voltage[2] (V_ℓ), the plasma charge (Z_i) and the

[2]Based on sign conventions from Refs. [16, 107] the loop voltage is negative here.

ion–ion collision time (τ_{ii}, from Eq. 2.15) [16, 107], by the relation (Eq. (56) from Ref. [16]):

$$V_{\|} = -\frac{\tau_{ii} Z_i e E_{\|}}{m_i} \frac{Z_I - Z_i}{Z_I} \frac{\sqrt{2} + 13\alpha/4}{(1+\alpha)(\sqrt{2}+\alpha)} \frac{n_i m_i}{n_i m_i + n_I m_I} + \frac{n_e m_e}{n_i m_i + n_I m_I} \frac{\sigma_{Spitzer}}{e n_e} E_{\|} \tag{5.1}$$

where the Spitzer resistivity is given by[6]:

$$\sigma_{Spitzer} \simeq \frac{\pi e^2 \sqrt{m}}{(4\pi\epsilon_0)^2 (k T_e)^{3/2}} \ln \Lambda. \tag{5.2}$$

The second term on the right hand side of Eq. 5.1 is the contribution due to the electron momentum. This term has been dropped because it is smaller by a factor of the square root of the mass ratio, ($\simeq \sqrt{\frac{m_e}{m_i}}$.) When the constants are evaluated, Eq. 5.1 reduces to (Eq. (1) from Ref. [107]):

$$V_\phi = 4.19 \times 10^5 f \frac{Z_i V_\ell T_i^{3/2}}{\sqrt{\mu} R n_i} \qquad (m/s) \tag{5.3}$$

where (Eq. (2) from Ref. [107]):

$$f = \frac{Z_I - Z_i}{Z_I} \frac{\sqrt{2} + 13\alpha/4}{(1+\alpha)(\sqrt{2}+\alpha)} \frac{n_i m_i}{n_i m_i + n_I m_I} \tag{5.4}$$

where Z is ion charge, m is the ion mass, and n is the ion density for the majority ion (i) or the impurity ion (I), $\alpha \equiv n_I Z_I^2 / n_i Z_i^2$. Equation 5.3 can be rewritten as:

$$\frac{1}{n_i} = -2.387 \times 10^{-6} \frac{V_\phi R \sqrt{\mu}}{f Z_i V_\ell T_i^{3/2}} \equiv RHS \qquad (m^3). \tag{5.5}$$

The bulk ion velocity in the same frame of reference is also given by Eq 5.3, but with f given by:

$$f = -\frac{Z_I - Z_i}{Z_I} \frac{\sqrt{2} + 13\alpha/4}{(1+\alpha)(\sqrt{2}+\alpha)} \frac{n_I m_I}{n_i m_i + n_I m_I}. \tag{5.6}$$

To avoid confusion this will be referred to as f_i. Since $f_i/f = n_I m_I / n_i m_i \ll 1$ the velocity of the impurities in this reference frame is much greater that the velocity of

the bulk ions. For the bulk ions, assuming a nominal impurity density of 1×10^{-4}, Eq. 5.5 can be written as:

$$\frac{1}{n_i} = 2.387 \times 10^{-6} \frac{V_\phi R \sqrt{\mu}}{f_i Z_i V_\ell T_i^{3/2}} \qquad (m^3)$$

$$= -RHS \cdot \frac{n_i m_i}{n_I m_I} \simeq -500 \cdot RHS \quad (m^3). \tag{5.7}$$

During a density scan, rotation data were taken over a wide range of densities for many ohmic L–mode discharges. In order to take into account the effects of T_e and n_e profiles, data have been used to evaluate the right hand side (RHS) of equation 5.5. The result is plotted in Fig. 5-2 versus n_e, using the C–port spectrometer data as $V(0)$.

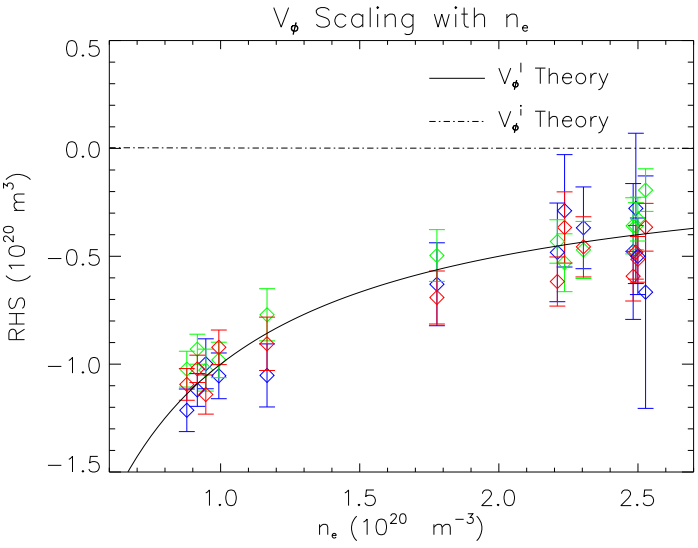

Figure 5-2: A plot of the right hand side (RHS) of Eq. 5.5 vs. n_e. This plot makes the assumption that the electron density and the ion density are the same. In this set of shots $Z_{eff} \simeq 1$, so this is a valid assumption. Overplotted is the line RHS $= 1/n_e$. The chain curve is the density scaling for the ions, predicted by Eqs. 5.3 & 5.7.

The agreement with the line $1/n_e$ is within error bars. The data are therefore consistent with the bulk ion velocity being zero; the observed negative impurity velocity reflects, entirely, the difference between the impurity and the bulk ion velocity, caused

by the balance between the drag and the toroidal electric field. It is also consistent with there being zero total momentum density.

The data at each radius adhere to this scaling (Eq. 5.1) within error bars, it is then concluded that this relationship between neoclassical rotation velocity and density in L–mode is valid over most of the plasma. These data were obtained during a "piggy back" run, better agreement could perhaps be reached with a dedicated run.

5.2 Rotation Profiles in Ohmic H–Modes

During Ohmic H–modes the plasma rotates in the co–current direction just as it does in ICRF H–modes[17, 30, 108], although the rotation velocity is, in general, smaller in magnitude.

The shape of the rotation profile in Ohmic H–mode is fairly flat. From this it has been inferred that if momentum comes from the edge, it only diffuses into the plasma; there is no evidence for a velocity pinch mechanism in the inner half of the plasma during Ohmic plasmas.

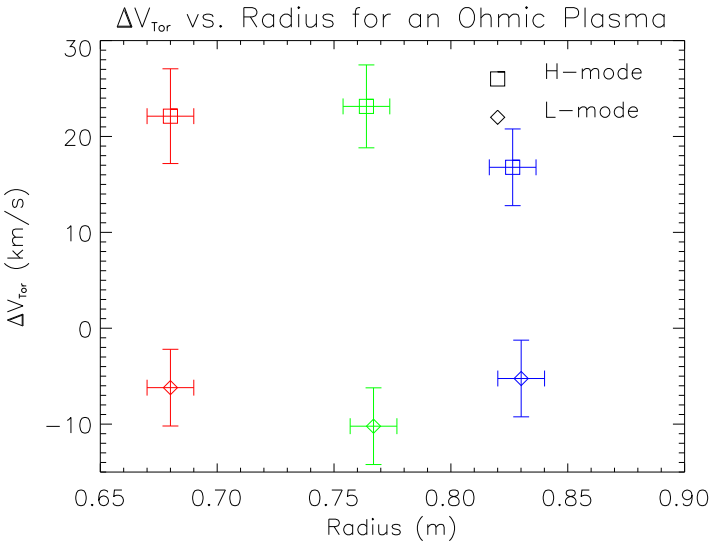

Figure 5-3: Rotation profiles in the L–mode phase of the discharge, and the fully developed H–mode phase of the discharge.

Figure 5-3 is fairly characteristic of the rotation profiles during both the L–mode and the H–mode phases of Ohmic discharges. During the L–mode phase the rotation is flat and counter-current, (§5.1). When the H–mode is fully developed, the profile is again fairly flat. The Ohmic H–mode rotation velocity has consistently been found to be 15 $km/s < V_\phi < 40$ km/s, co–current.

5.2.1 Ohmic L → H Transition

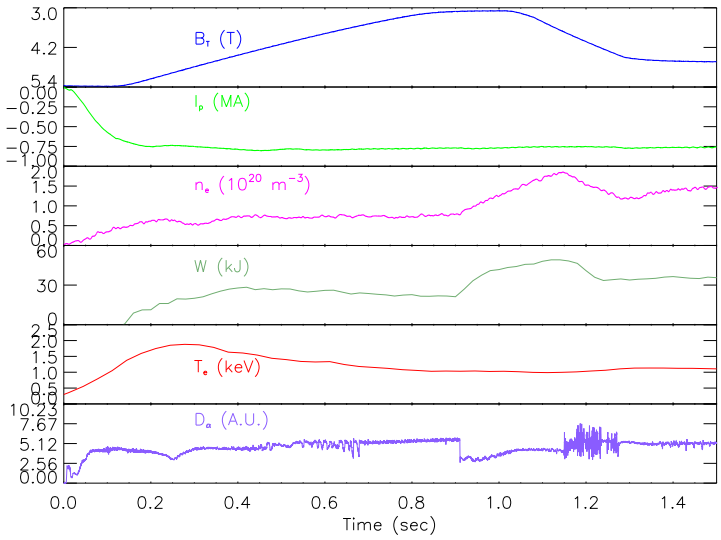

Figure 5-4: Time histories of some plasma parameters. From top to bottom: B_T (T), I_P (MA), n_e (10^{20} m^{-3}), $W(kJ), T_e$ (keV), and the Emissivity of D_α light (A.U.).

One way to achieve Ohmic H–modes is by ramping the toroidal magnetic field down. Lowering the toroidal field with a constant plasma current and relatively low density lowers the H–mode threshold. This can lead to an Ohmic H–mode.

Time histories of some plasma parameters have been plotted in Fig. 5-4. From top to bottom: toroidal magnetic field in Tesla, plasma current in Megamperes, electron density in number per cubic meter, the plasma stored energy in kilojoules, electron temperature in kiloelectron–volts, and the emissivity of D_α light in arbitrary units. These parameters are for just one of the eight discharges used to create the spectra for the time history in Fig. 5-5. The discharges were highly reproducible.

The ramping of the toroidal field can clearly be seen in the B_T trace. At approximately 0.9 seconds the electron density and the plasma stored energy both start to rise and there is a drop in the D_α emission.

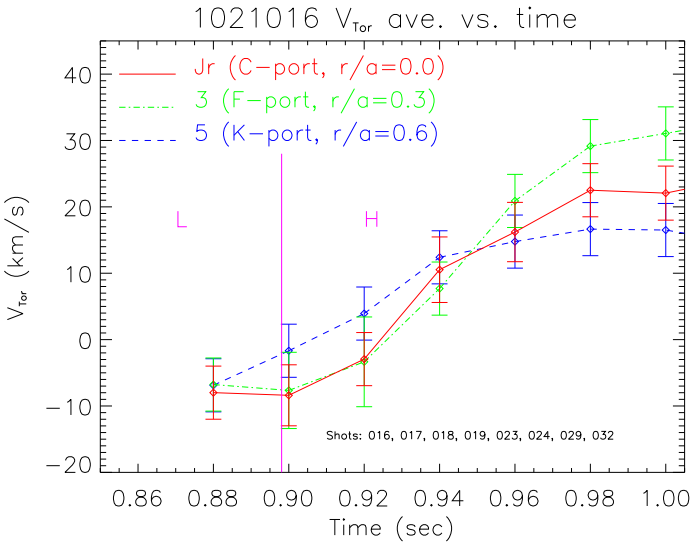

Figure 5-5: Time history of toroidal rotation for a plasma(s) going into an Ohmic H–mode. The outermost channel can clearly be seen to rise first, the inner two seem to rise together, at a later time. These traces were generated from the average over 8 different plasma shots. (These data have been smoothed in time using "nearest neighbor" smoothing.)

Figure 5-5 shows the time histories of the three spectrometer channels. The rotation can be seen to start in the outer portion of the discharge, and propagate in. This will be discussed further, later in this Chapter.

The signature of a plasma going into an H–mode is a drop in the Balmer α light emitted from deuterium (D_α). Fig. 5-6 is a plot of the time traces for the D_α emission from the eight discharges that were added together to produce Fig. 5-5. The sudden precipitous drop is the indication that the plasma has made the transition into H–mode.

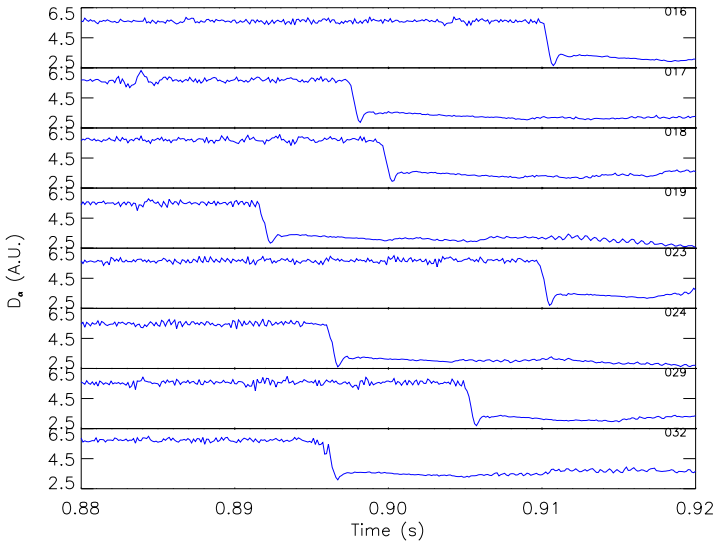

Figure 5-6: The transition from L–mode to H–mode for eight different shots as seen in the emission of D_α light. The deviation, the average, and the standard deviation for these L $\rightarrow$ H transitions have been calculated and tabulated, see Table 5.1

5.2.2 Spectra Adding

To use different shots to increase the photon counting statistics it is necessary to make sure, among other things that the L $\rightarrow$ H transition occurs at the "same" time in each shot, really just within the spectrum integration time, (20 ms for this set of shots). That is, no transition that is going to be used in this spectral adding can deviate from the average L $\rightarrow$ H transition time by more than one half of the integration time.

The transition times associated with each shot have been tabulated, and their average and standard deviation calculated; this information is presented in Table 5.1.

A mean time of transition and a standard deviation in the times of transition have been calculated as 0.900729 s and 0.00686 s, respectively. The standard deviation of the L $\rightarrow$ H times is less than half the integration time of the data acquisition (20 $ms/2$), so we may add together the spectra from these shots with confidence. In this case even the maximum deviation from the average (0.009396 s, shot 016) is less than half of the integration time, so these data can certainly be used together introducing only negligible error.

Shot	t_{L-H} (s)	$\Delta\ t_{L-H} = \bar{t}_{L-H}$ - t_{L-H}
016	0.910125	−0.009396
017	0.897553	0.003176
018	0.899616	0.001113
019	0.891583	0.009146
023	0.90988	−0.009151
024	0.895973	0.004756
029	0.905011	−0.004282.
032	0.896093	0.004636
$\bar{t}_{L-H}$	0.900729	0.0
$\sigma_{t_{L-H}}$	0.00686	—

Table 5.1: For run 1021016: the shots involved, their associated L → H transition times ($t_{L\rightarrow H}$) and deviation ($\Delta\ t_{H-L}$). A mean time of transition and a standard deviation in the times of transition have been included. The standard deviation of the L → H times is less than half the integration time of the data acquisition, so we may add together the spectra from these shots with confidence. In this case even the maximum deviation from the average transition time is less than half of the integration time.

5.3 Momentum Diffusion Time Scale Measurements

The time scale for momentum diffusion can be inferred from the relative lag in the rise times of the spectrometers. By watching the rotation velocities on the outermost, then the middle, and finally the core channels rise, the momentum confinement time can be measured.

Figure 5-7 shows rotation profiles at different times for the sum of shots shown as time histories in Fig. 5-5. In this figure it is easy to see that the rotation increases on the outer most channel ($r/a = 0.6$, r = 0.835 m) first and then propagates inward. The rotation on the core spectrometer ($r/a = 0.0$, r = 0.685 m) and the middle spectrometer ($r/a = 0.3$, r = 0.773 m) seem to come up at about the same time.

5.3.1 The Simple Model

In Ohmic H–modes it appears that momentum diffusion is the dominant process. In this section momentum diffusion will be modeled using a simple diffusion equation.

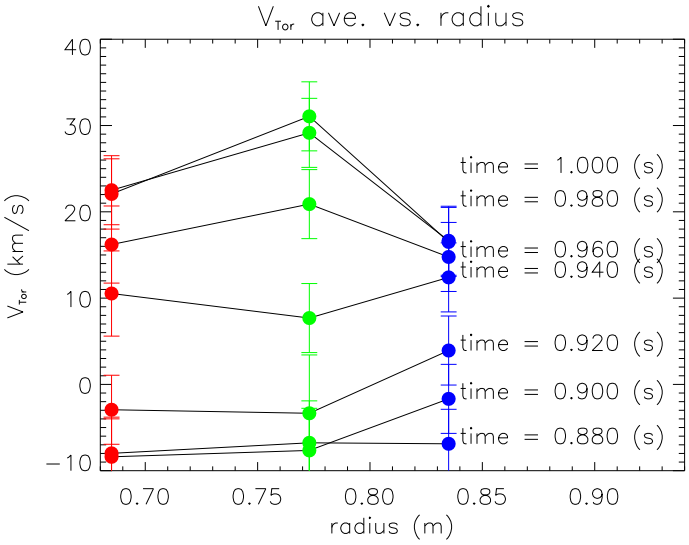

Figure 5-7: Rotation profiles at various times for the set of discharges in Figs. 5-4 – 5-6 . The velocity can be seen to rise first at the edge, and then later in the core, this indicates that the momentum source is at the edge of the plasma, and propagates into the core by diffusion.

The model will then be compared to some data.

The simplest model for the diffusion of momentum is to assume that momentum obeys the equation:

$$\frac{\partial}{\partial t}P + \frac{1}{r}\frac{\partial}{\partial r}r\Gamma_P = 0 \tag{5.8}$$

where:

$$\Gamma_P = -D\frac{\partial}{\partial r}P \tag{5.9}$$

and P $= n_i m_i V$. With the assumptions that $\mathbf{V} = V_\phi$ and the density profile is flat (*i.e.* $\frac{\partial}{\partial r}\, n_i = 0$.) During H–mode this assumption has been shown to be correct over most of the plasma, except the pedestal. Equation 5.8 then becomes:

$$\frac{\partial}{\partial t}V_\phi - D\left[\frac{\partial^2}{\partial r^2}V_\phi + \frac{1}{r}\frac{\partial}{\partial r}V_\phi\right] = 0. \tag{5.10}$$

Assuming Eq. 5.10 is separable (with separation constant λ_i), in cylindrical coordinates, a general solution is[109, 110]:

$$V_\phi = V_{\phi T}(t)V_{\phi R}(r) = V_0 + \sum_{i=1}^{\infty} c_j e^{-\lambda_i D t} J_0(\sqrt{\lambda_i} r) \tag{5.11}$$

or toroidal momentum P_ϕ is:

$$P_\phi = m_i n_i V_{\phi T}(t)V_{\phi R}(r) = P_0 + m_i n_i \sum_{j=1}^{\infty} c_j e^{-\lambda_j D t} J_0(\sqrt{\lambda_j} r) \tag{5.12}$$

Equations 5.11 and 5.12 are Bessel expansion solutions of Eqs. 5.8 or 5.10 with one differing from the other by a factor of $n_i m_i$. One of these together with the assumed boundary conditions, (at $r = a$):

$$f_\phi = \begin{cases} 0, & t < t_{L\to H} \\ P, & t_{L\to H} \le t \le t_{H\to L} \\ 0, & t > t_{H\to L} \end{cases} \tag{5.13}$$

where: f_ϕ is the momentum or velocity boundary value, uniquely define a solution for momentum diffusion, with parameters D the diffusion coefficient, P the edge rotation velocity or edge momentum density, depending on which quantity is being solved for. In either case the coefficient c_j is given by:

$$c_j = \frac{\int_0^a f_\phi J_0\left(\frac{z_j r}{a}\right) r dr}{\int_0^a \left(J_0\left(\frac{z_j r}{a}\right)\right)^2 r dr}. \tag{5.14}$$

The eigenvalues are defined as $\lambda_i \equiv z_i^2 / a^2$, where z_i is the ith zero of the Bessel function J_0 and a is the minor radius.

These boundary conditions imply a step function in the edge velocity or momentum, that turns on instantaneously at time $t = t_{L\to H}$ (the L $\to$ H transition) and then stays on until the plasma returns to L–mode. The physical interpretation of this P is a momentum source at the edge of the plasma, most likely it is some source in the H–mode pedestal, or in the scrape off layer (SOL).

The momentum confinement time (τ_{V_ϕ}) is taken from the time dependent portion

of the solution: $V_{\phi T}(t) = [\exp(-\lambda_i D t)] = [1 - \exp(-t/\tau_{V_\phi})]$. Thus:

$$\tau_{V_\phi} = \frac{1}{\lambda_0 D}. \tag{5.15}$$

Only λ_0 is used, ($\lambda_0 = \frac{z_0^2}{a^2} = \frac{2.405^2}{0.21^2} \simeq 131.157$), because it will have the longest time associated with it and therefore dominates the process.

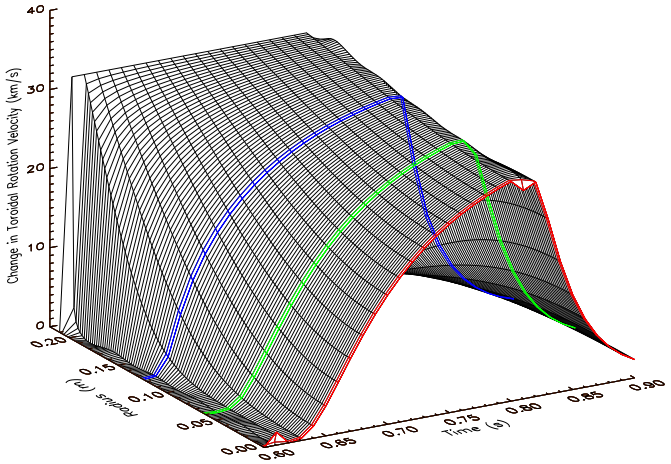

Figure 5-8: Surface plot of the toroidal rotation velocity versus space and time, as predicted by the simple model. The locations of the three spectrometers are indicated in their conventional colors. A small spike upwards at $r = 0$, $t = t_{L\rightarrow H}$, and a small spike down at $r = 0$, $t = t_{H\rightarrow L}$, can be seen on the surface, these are artifacts of the truncated series.

Figure 5-8 is a surface plot of Eq. 5.11; the change[3] in toroidal rotation velocity versus minor radius and time. For this calculation the momentum source (P) was turned on at the L $\rightarrow$ H transition ($t \simeq 0.61\ s$) and turned off at the H $\rightarrow$ L transition ($t \simeq 0.81\ s$). The particle mass is constant and density is assumed to be flat, including them in this solution will change the absolute value of the solution, but it will not change the general shape.

Equation 5.11 (equivalently eq. 5.12) is an infinite sum over Bessel functions.

[3]That is the change between the L–mode value and the H–mode value of toroidal rotation.

The series was truncated, (191^{st} Bessel zero). There are two results from this lack of convergence. First, a slight ringing, (a residual oscillation,) left over from the approximation of convergence. Second, a slight bump on the innermost grid point at the L $\rightarrow$ H and H $\rightarrow$ L transition times, this is because the series of c_ns is an alternating one[4], and the convergence to 1 is quite slowly. Were this series carried out to infinity, this ringing and the shift would, of course, disappear.

Figure 5-9 shows the time histories of three spatial slices of the surface, (Fig. 5-8,) corresponding to the three spectrometer's view locations. Overplotted in this figure is the change in the rotation velocity from Ohmic L–mode to H–mode.

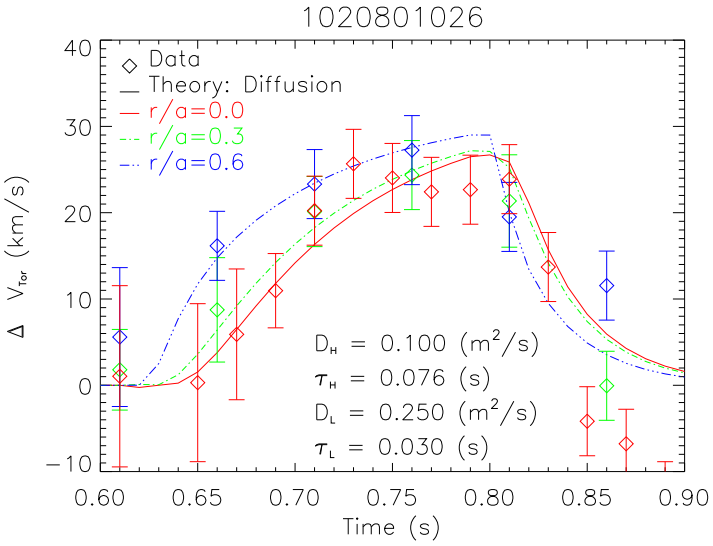

Figure 5-9: Time history of Ohmic rotation data with the corresponding traces as predicted by the simple momentum diffusion model. The diffusion coefficients and the momentum confinement times for both the L $\rightarrow$ H ($D_{LH} \equiv D_H$ and $\tau_{LH} \equiv \tau_H$) and H $\rightarrow$ L, ($D_{HL} \equiv D_L$ and $\tau_{HL} \equiv \tau_L$) transitions are noted on the plot. The data are plotted here as the change in rotation between L–mode and H–mode. (These data have been smoothed in time using "nearest neighbor" smoothing.)

Figure 5-10 has some of the plasma parameters for the discharge from which the data in Fig. 5-9 were taken.

The data and the time traces from the simple model were fitted, using D as a

[4]If the 192^{nd} zero were used the shifts would be reversed.

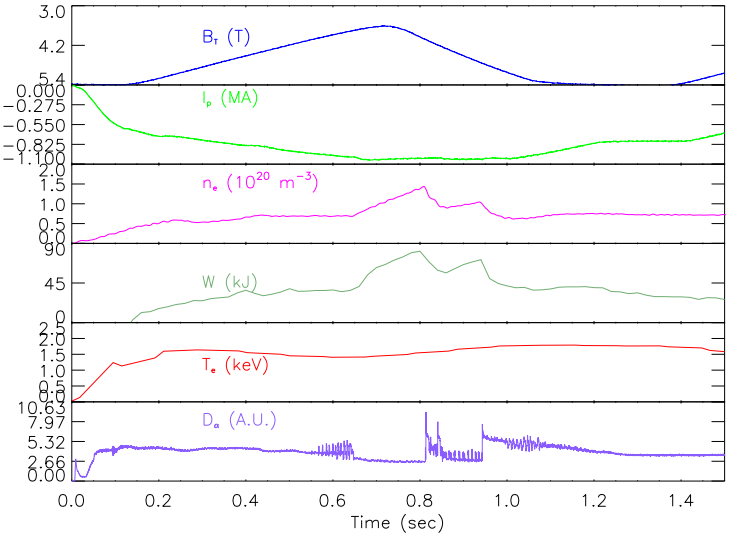

Figure 5-10: Some plasma parameters for the discharge in Figs. 5-8 and 5-9.

free parameter, for the various periods in the discharge. A constant D was chosen for the H–mode portion of the discharge, and different constant D was chosen for the L–mode portion of the discharge. The edge rotation velocity P from Eq. 5.11 and the boundary conditions Eq. 5.13 are taken from the data. The final rotation velocity P is taken from the outermost spectrometer's rotation value, ($P = 32\ km/s$ in this case.) The L $\rightarrow$ H and the H $\rightarrow$ L times are taken from the D_α traces. The diffusion coefficient D is then varied until the data and the model surface coincide. Using $D_{LH} \equiv D_H = 0.100\ m^2/s$ and $D_{HL} \equiv D_L = 0.250\ m^2/s$ the fit is quite good. These diffusion coefficients imply momentum confinement times of $\tau_{V_\phi,LH} = \tau_{LH} \equiv \tau_H = 0.076$ s and $\tau_{V_\phi,HL} = \tau_{HL} \equiv \tau_L = 0.030$ s.

It is interesting to note that the time scale of the L $\rightarrow$ H and H $\rightarrow$ L transitions are not the same. The time scale for the transition from L–mode to H–mode is about 2.5 times longer. Stated differently:

$$\frac{\tau_{\phi H}}{\tau_{\phi L}} \simeq 3 \simeq \frac{\tau_{EH}}{\tau_{EL}}. \tag{5.16}$$

Similar results have been found on other devices, see Chapter 3.

The simple model and the assumed boundary conditions seem to do quite a good job of explaining the observed data. For comparison the time scales from various theories presented in Chapter 2 have been calculated and are presented in Table 5.2.

	R. Neocls. $(\tau_{U_{\parallel,i}})_{viscous}$ (s)	R. Neocls. $(\tau_{U_{\parallel,i}})_{f.l.r.}$ (s)	Subneocls. $\tau_{U_{\parallel,i}}$ (s)	Subneocls. $\tau_{U_{\parallel,i}}$ (s)	Simple Model τ_{V_ϕ} (s)
Shot	Eq. 2.20	Eq. 2.21	Eq. 2.22	Eq. 2.25	Eq. 5.15 or 6.9
1021016017	9432.4946	0.00227556	3629.3007	233.47253	0.076 (H) 0.030 (L)

Table 5.2: Momentum confinement times from revisited neoclassical theory, subneoclassical theory, and the simple models fit to data presented in this chapter.

The τ_ϕs are short and thus imply anomalous momentum transport, and the diffusivities $\chi_\phi \equiv D$ are large, a factor of 50 higher than that predicted by neoclassical theory, $\chi_\phi \simeq \rho_i^2 \nu_{ii}$[82]. A plot of the fitted diffusivities and the expected neoclassical diffusivities is presented in Fig. 5-11.

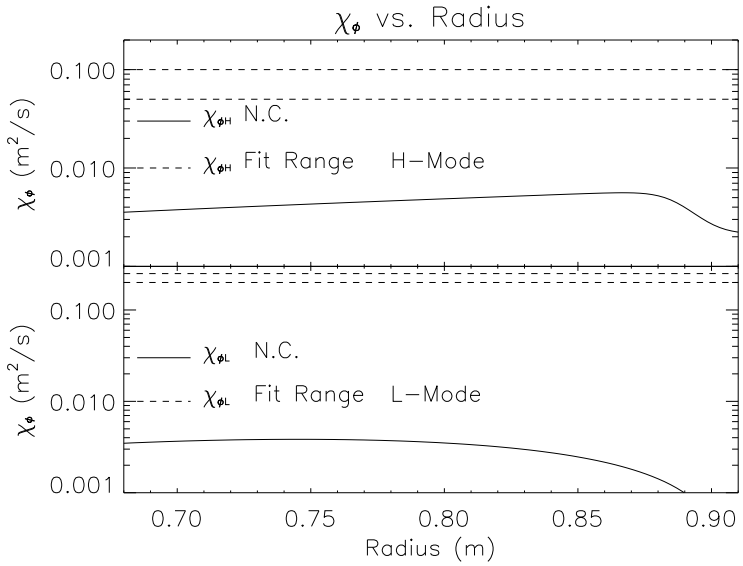

Figure 5-11: A plot of the χ_ϕ vs. radius, for the fitted diffusivities and that predicted by neoclassical theory. The top plot is for H–mode, and the bottom plot is for L–mode.

5.4 Inferred Radial Electric Field

From neoclassical theory, Eq. 2.16 of §2.1.4 can be used to calculate what the radial electric field in the plasma must be in order to give these rotation profiles.

$$E_r = V_\phi^I B_\theta - \frac{(K_1 + \frac{3}{2}K_2 - 1)}{e}\frac{\partial}{\partial r}T_i + \frac{T_i}{en_i}\frac{\partial}{\partial r}n_i \tag{2.16}$$

Using Eqs. 2.5 – 2.14, and Table 2.1 from §2.1.1, in Chap. 2, we can calculate the values of the coefficients K_1 and K_2 throughout the volume of the plasma for all regimes.

Fig. 5-12 is a plot of the individual terms from equation 2.16. On axis the radial electric field must be zero. Terms 1, 2 and 3 have been thus been set, identically, to zero at $r/a = 0$. These are *not* measured quantities. It can be seen that the dominant term is Term 1, ($V_\phi^I B_\theta$.) Term 2, ($-\frac{(K_1+\frac{3}{2}K_2-1)}{e}\frac{\partial}{\partial r}T_i$,) has the least effect, it corresponds to $V_\theta^I B_\phi$.[5] In the above formulation (Eq. 2.16) Term 3 is a density gradient scale length ($\frac{T_i}{en_i}\frac{\partial}{\partial r}n_i$), it is of the same order as Term 2.

The remaining quantities in Eq. 2.16 are measured during normal plasma operation. Figure 5-13 shows time histories of the radial electric field at the outer two spectrometer view locations, the central view has been set to zero. Figure 5-14 shows the same information in profile form.

It can be seen that the E_r profiles are Flat throughout the discharge.

5.5 Error Analysis

5.5.1 Measurement Error

The error associated with these measurements comes from two main sources. Systematic error associated with the measurement and the error associated with the Gaussian line fits.

The systematic error, associated with the lack of absolute wavelength calibration

[5]This can be seen by substituting Eq. 2.3 in for this term. The quantity V_θ^I is very small and offsets the large value of B_ϕ

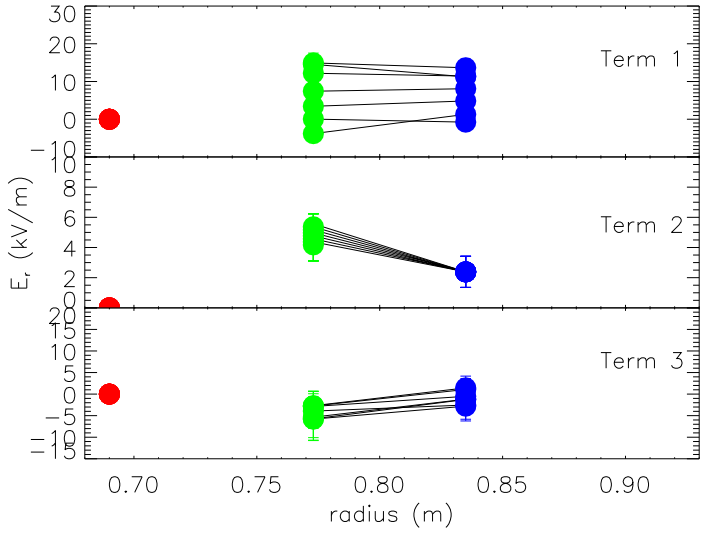

Figure 5-12: The profiles of the three terms that make up the calculation of the inferred radial electric field. Term 1 $\equiv V_\phi^I B_\theta$, Term 2 $\equiv -\frac{(K_1+\frac{3}{2}K_2-1)}{e}\frac{\partial}{\partial r}T_i$ and Term 3 $\equiv \frac{T_i}{en_i}\frac{\partial}{\partial r}n_i$. Each term has been plotted vs. radius in 50 ms steps from before the H–Mode, throughout its development and back to L–Mode.

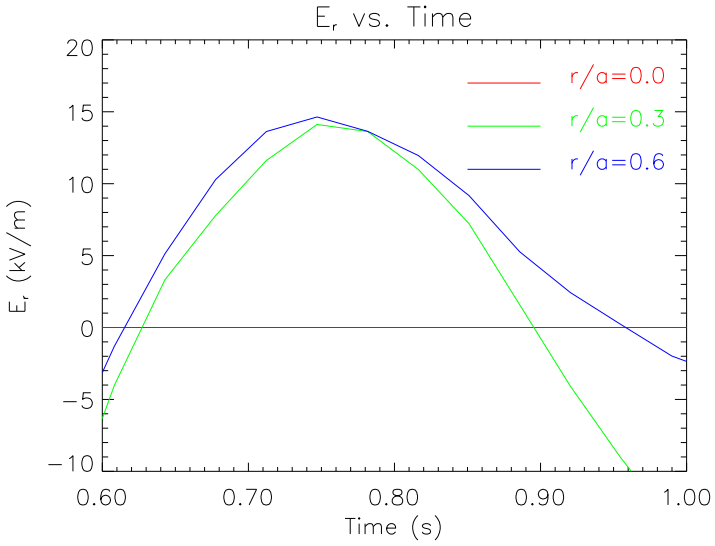

Figure 5-13: Time histories of the inferred radial electric field at the view locations of the three spectrometers.

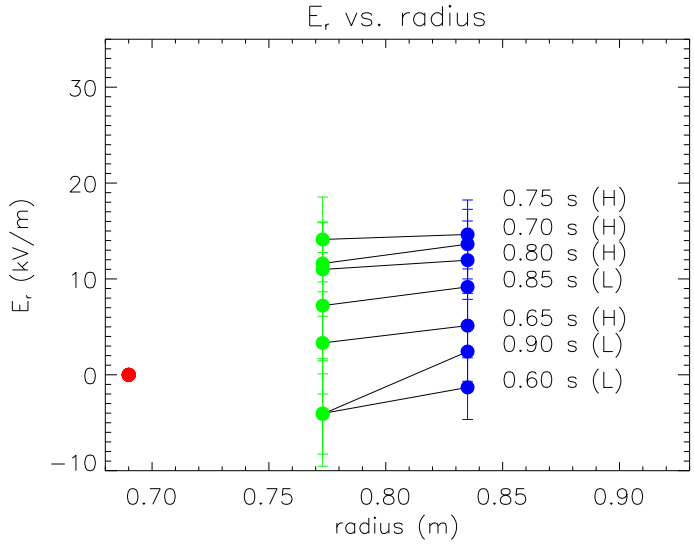

Figure 5-14: Profiles of the radial electric field every 50 ms during the evolution of the H–mode. The profiles are essentially flat throughout the evolution.

has been estimated, by assuming that the L–mode rotation profile deviates from flat by as much as half of the L–mode offset, ($\simeq 4.0\ km/s$). An absolute calibration was made for the C–port spectrometer before it was installed, (see §4.3.3.) In this thesis it has been assumed that the L–mode profile is flat.

The Gaussian line fits are performed by an IDL procedure, the outputs from which are the Gaussian fit parameters, and the associated standard deviations. These standard deviations and the "systematic" uncertainty are folded together to generate a total error for any given rotation velocity datum. A sample calculation has been made below.

$$\sigma_{total} = \sqrt{\sigma_{fit}^2 + \sigma_{Systematic}^2} \tag{5.17}$$

This can be stated as:

$$\sigma_{total} = \sqrt{\sigma_{fit}^2 + (4.0)^2} \tag{5.18}$$

For the K–port spectrometer, in Fig. 5-1:

$$\sigma_{total} = \sqrt{(3.57)^2 + (4.0)^2} = 5.36(km/s)$$

The estimate of the systematic drift in the baseline was found by summing spectra from the L–mode phase of various shots over the course of the campaign, and determining the weighted average L–mode offset and its standard deviation. Fig. 5-15 is a plot of this information for a series of shots, the weighted average and standard deviation have been tabulated in Table 5.3. The L–mode rotation velocity does not drift noticeably in time. It is concluded that the time dependent systematic error is within the standard deviation of the L–mode baseline.

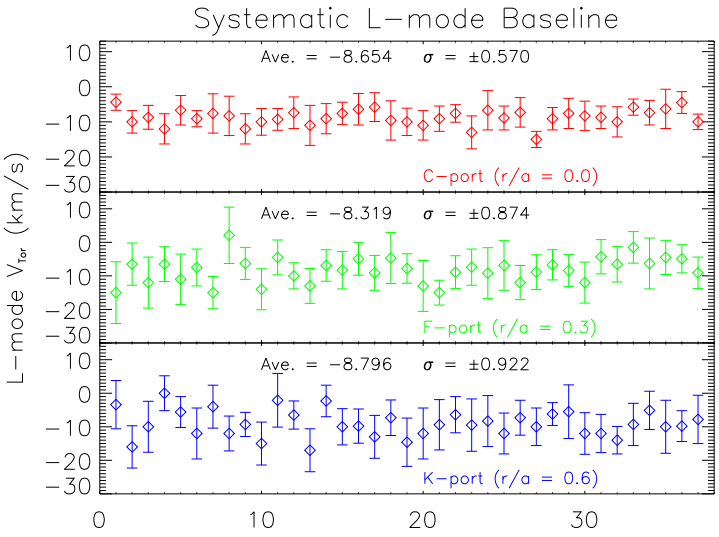

Figure 5-15: A plot of the L–mode baseline rotation for 37 different shots throughout the run campaign. The average offset, the standard deviation of the offset and the average standard deviation, have been included on the plot, for each spectrometer.

A simple calculation of the detector shift required to produce a 1 km/s shift in the measured velocity can be made. The detector is 4 cm wide. There are 1024 channels in this space, each channel corresponds to 17.0 km/s, so[6]:

[6]The coefficient of linear thermal expansion of Al, which most of the spectrometer stand is made out of, is 23.1 $\frac{\mu m}{K \cdot m}$ [111].

Spectrometer	$\overline{V_{Tor}}$ (km/s)	$\sigma_{V_{tor}}$ (km/s)
C $(r/a \simeq 0.0)$	-8.684	$\pm$ 0.570
F $(r/a \simeq 0.3)$	-8.281	$\pm$ 0.874
K $(r/a \simeq 0.6)$	-9.095	$\pm$ 0.922

Table 5.3: The weighted average and the standard deviation of the offset for the L–mode baseline, from Fig. 5-15.

$$\frac{0.04}{1024 \cdot 17} = 2.29 \times 10^{-6} \ \frac{m}{km/s} = 2.29 \ \frac{\mu m}{km/s}.$$

There is also an uncertainty in the absolute radial position of the measurement. The error in this value arises from the localization of the view and the peak in the emissivity, see §4.3.1. Based on the shape of the emissivity profile the uncertainty in the location is nominally $\pm$ 1 cm, ranging between about $\sim$ 2 cm for the C–port spctrometer, and $\sim$ 0.8 cm for the K–port spectrometer.

The calculation for the radial electric field was done in three terms, each of which has an error associated with it[7]

$$\sigma_{E_r} = \sqrt{\sigma^2_{Term1} + \sigma^2_{Term2} + \sigma^2_{Term3}} \tag{5.19}$$

Where:

$$\sigma_{Term1} = \sqrt{B^2_\theta \sigma^2_{V_\phi} + V^2_\phi \sigma^2_{B_\theta}} \tag{5.20}$$

$$\sigma_{Term2} = \frac{(K_1 + \frac{3}{2}K_2 - 1)}{e} \sigma_{\frac{\partial}{\partial r}T_i} \tag{5.21}$$

[7]A more thorough treatment of the error in this calculation would include covariant terms in the calculation of the standard deviations σ_{E_r}. This has not been done her for two reasons. First, the correlation between terms is believed to be small, that is deviation in one measured quantity will not, in general, have a large effect on another measured quantity. This is not necessarily true for the temperature or density and their respective derivatives. Second, and more importantly, there is not sufficient data to calculate a statistically significant covariance for either of these terms.

$$\sigma_{Term3} = \sqrt{\left(\frac{T_i}{en_i}\frac{\partial}{\partial r}n_i\right)^2}\sqrt{\frac{1}{T_i^2}\sigma_{T_i}^2 + \frac{1}{n_i^2}\sigma_{n_i}^2 + \frac{1}{\left(\frac{\partial}{\partial r}n_i\right)^2}\sigma^2_{\frac{\partial}{\partial r}n_i}} \tag{5.22}$$

These errors have been propagated through and overplotted on their respective terms (Fig. 5-12) and on the electric field profiles, (Fig. 5-14). The largest contribution to the error is the toroidal rotation velocity. The uncertainties in most of the other quantities are fairly low, (< 10 %.)

Error introduced by taking numerical derivatives present a particular problem, small deviations in the original data can lead to wildly different values for the derivative. This was overcome by fitting a spline to the data and then taking the derivative, numerically, of the fit. The χ^2 error statistic of the fit then provides a measure of the uncertainty in the derivative.

5.5.2 Model Error and Sensitivity

The error in the model fit comes from the fitting of the free parameter: the diffusivity. The amplitude of the edge source is assumed to be final rotation velocity, as measured by the outer most spectrometer. While the terminal or edge rotation velocity could be considered a free parameter, it has not been because the fit is quite dependent on it. If the H–mode lasts long enough, (a few times τ_ϕ) it is quite clear what the value should be. If the H–mode doesn't last it can be more difficult to determine what this value is.

To properly deal with the fit and the uncertainty in the free parameter, a minimization of the χ^2 statistic was performed[112]. For a function of two variables, (*e.g.* $V_\phi(r,t)$,) χ^2 is defined as:

$$\chi^2 \equiv \sum_i \sum_j \left\{\frac{1}{\sigma_{ij}^2}[y_{ij} - y(x_i, x_j)]^2\right\}. \tag{5.23}$$

Where: σ_{ij}^2 are the experimental variances, y_{ij} are the data points, and $y(x_j, x_j)$ are the functional fits to the data at points x_i and x_j, with parameter a. The function $\chi^2(a)$ will be minimized with respect to the parameter a_k. In this case the parameter

a is D the diffusivity. When:

$$\frac{d\chi^2}{da} = \frac{d}{da}\sum_i\sum_j\left\{\frac{1}{\sigma_{ij}^2}[y_{ij} - y(x_i, x_j)]^2\right\} = 0$$
$$= -2\sum_i\sum_j\left\{\frac{1}{\sigma_{ij}^2}[y_{ij} - y(x_j, x_i)]\frac{dy(x_i, x_j)}{da}\right\} \quad (5.24)$$

the χ^2 error statistic has been minimized and thus the fit optimized. The χ^2 error Statistic has been plotted vs. D, for both the L $\rightarrow$ H transition, (D_H,) and the H $\rightarrow$ L transition, (D_L,) in figs. 5-16 and 5-17 respectively.

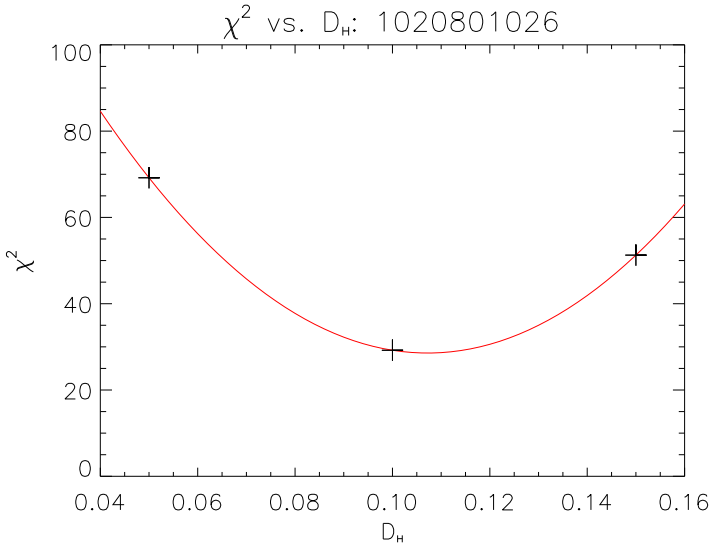

Figure 5-16: A plot of the χ^2 error statistic vs. D_H the fitted diffusivity, for the fit in Figs. 5-8 and 5-9. The fit parameter is almost the absolute minimum of the χ^2 curve, thus implying a very good fit of the parameter. It can also be seen that the fit is quite sensitive to the model parameter D, thus there is high confidence in the fit.

From these figures we can determine that the fit parameter D_H should be in the range 0.060 – 0.150 m^2/s, and D_L should be in the range 0.100 – 0.400 m^2/s.

Finally, a true "goodness of fit" can be calculated using the reduced chi squared, $\chi^2_\nu \equiv \frac{\chi^2}{\nu}$ where ν is the degrees of freedom defined as the number of points minus the number of fit parameters. If $\chi^2_\nu = 1$, this implies that the fit is optimal, much larger or much smaller imply a problem with the data or the model, respectively. For the

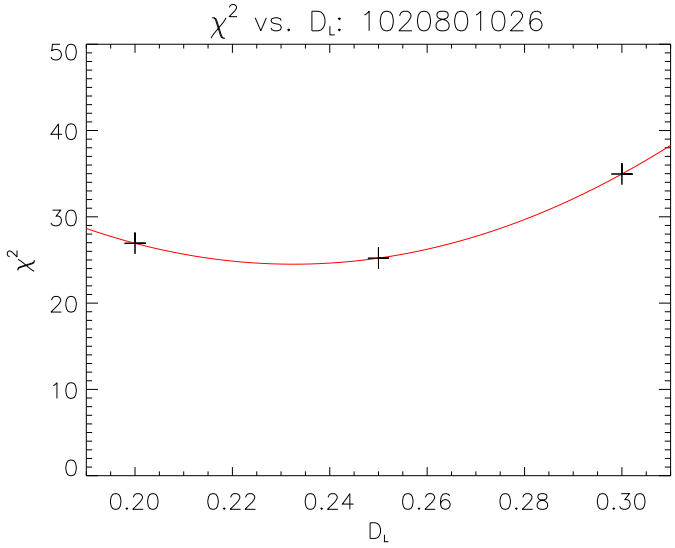

Figure 5-17: A plot of the χ^2 error statistic vs. D_L the fitted diffusivity, for the fit in Figs. 5-8 and 5-9. The fit parameter is almost the absolute minimum of the χ^2 curve, thus implying a very good fit of the parameter. It can also be seen that the fit is not very sensitive to the model parameter D_L.

fit to D_H:

$$\chi^2_\nu \equiv \frac{\chi^2}{\nu} = \frac{27}{22-1} = 1.227.$$

For the fit to D_L, $\chi^2_\nu = 2.6$. The model is quite sensitive to the input free parameter, (D).

Finally, it should be noted that the terminal rotation velocity is determined from the data by inspection, not fit as a free parameter. In many discharges, the length of the H–mode makes this quantity well known. In all the discharges presented in this chapter and the next, the rotation velocity was within 10% of the terminal velocity by the end of the H–mode.

Figure 5-18 is three plots showing the sensitivity of the fit to the value P. A change of 0.1 in the value of P, positive or negative completely under minds the fit.

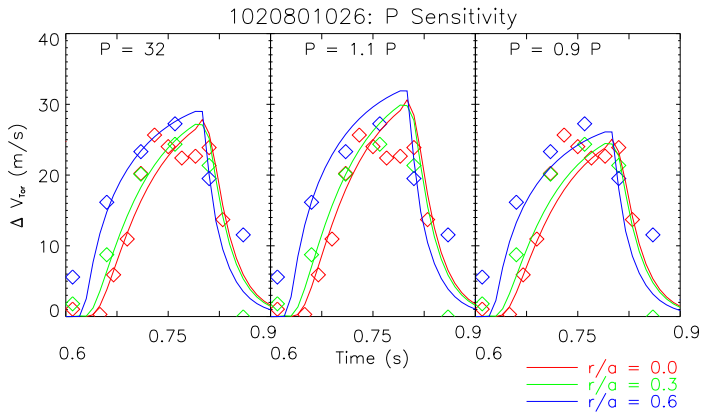

Figure 5-18: The three frames show the fit over plotted on the data for the discharge presented in Figs. 5-8 and 5-9, the fit if the boundary condition P is increased by 10% and the fit if the boundry condition P is decreased by 10%.

5.6 Rotation and Magnetic Geometry

It has been observed that during Ohmic L–mode discharges, in either the double null or upper null magnetic configuration, occasionally the plasma will start to rotate spontaneously in the counter current direction. In every observed case the discharge has been well developed and well evolved in a steady state L–mode and then, spontaneously, the rotation drops until the current ramp down begins.

The upper portion of Fig. 5-19 is a time history of the rotation as measured by the three spectrometers, for one such discharge. The lower portion is the quantity SSEP from the EFIT code[101–104]. When SSEP is negative the plasma is in the lower null configuration; when it is positive the plasma is in the upper null configuration. When it is zero the plasma is in the double null configuration. There is about 1 mm uncertainty in SSEP.

At about 1.2 s the rotation velocity starts to go strongly counter–current. Figure 5-20 is a plot of the magnetic geometry at 1.2 s. It is interesting to note that at the peak counter current velocity, the profile remains basically flat.

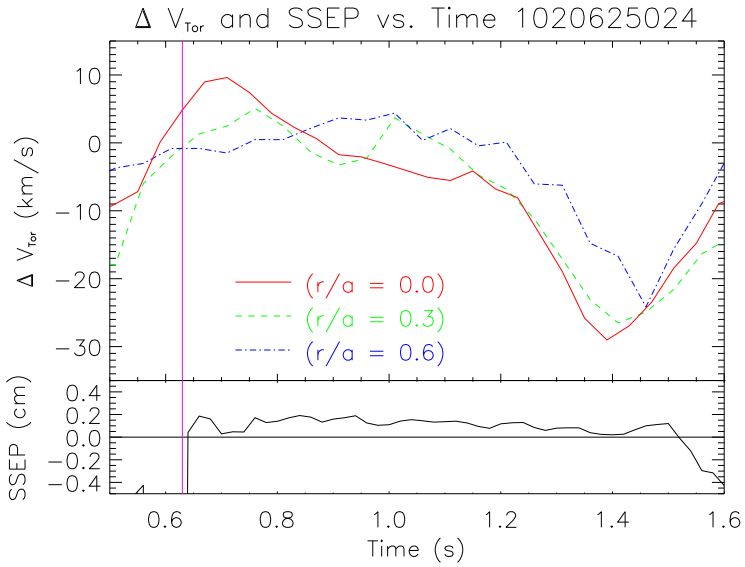

Figure 5-19: The upper plot are some data from a discharge when the plasma started to spontaneously rotate. The profile appears to be flat, that is the rotation velocity at each radial point measured is about the same. The lower plot is of SSEP (a measure of the null location) the vertical line shows the approximate time when the plasma went into double null configuration. (These rotation data have been smoothed in time using "nearest neighbor" smoothing.)

Figure 5-21 is a plot of the rotation velocity and SSEP for two other discharges where the rotation drops as the plasma goes into the double null configuration. These shots were before the spectrometer array had been built, so they only show the core rotation.

Figure 5-22 is a plot of the time of double null vs. the time the plasma starts to rotate strongly in the counter current direction, for 14 such discharges. The diagonal line is $y = x$. Points that fall on this line imply that the time the rotation drops corresponds exactly to the time the plasma goes into the double null. Points below this line imply the double null precedes the rotation drop. Points above this line would imply the rotation drop precedes the double null.

All the points fall on or below the line $y = x$, from this causality can be determined. In this set of shots, the double null always precedes or corresponds to the rotation drop. No systematic experimental study of this phenomena has yet been performed,

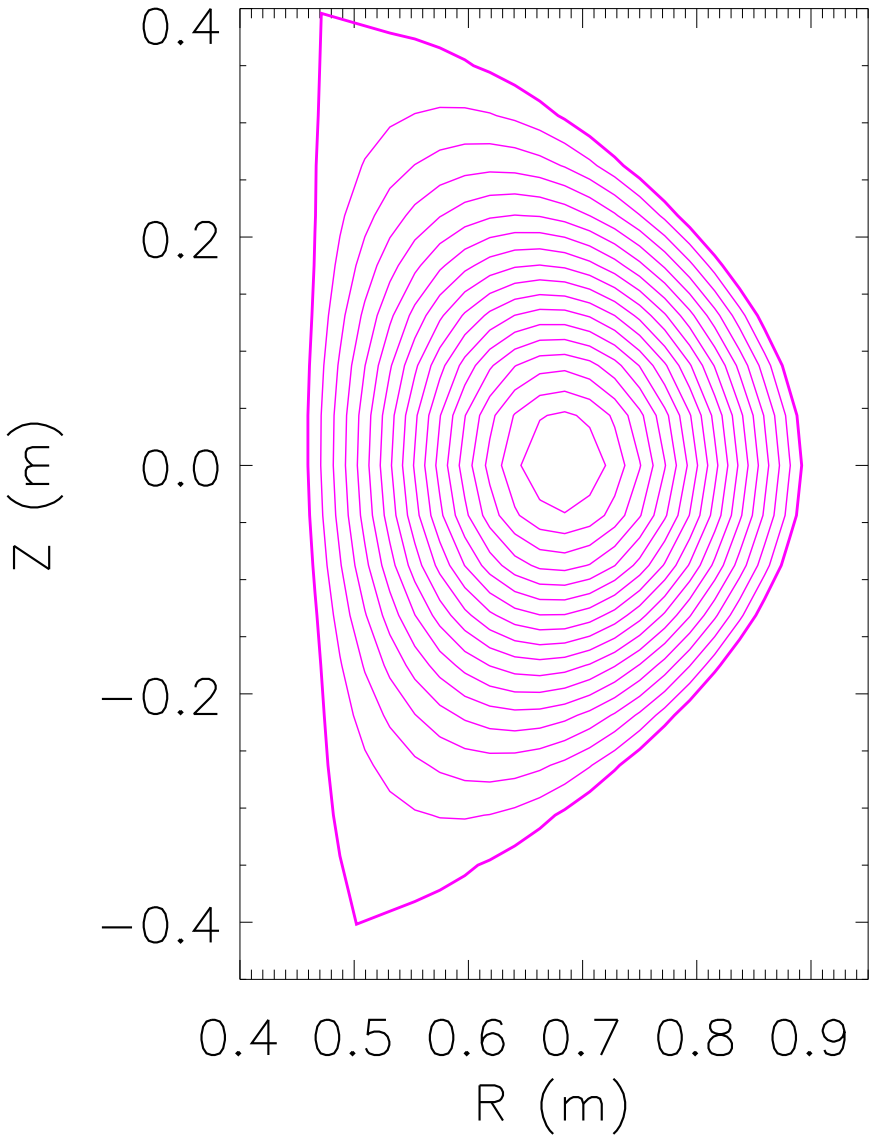

Figure 5-20: Magnetic geometry for the shot of the rotation traces in Fig. 5-19, at time equals 1.2 sec.

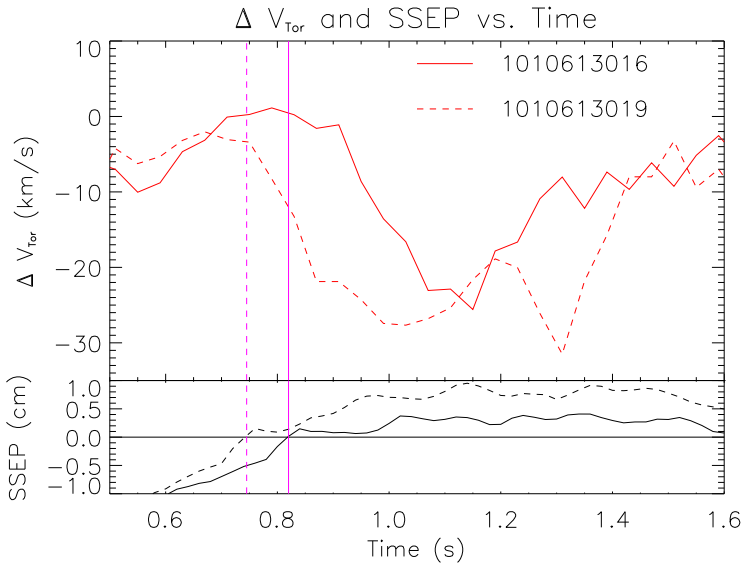

Figure 5-21: The upper plot are some data from two discharges when the plasma started to spontaneously rotate. The lower plot is of SSEP (a measure of the null location) the vertical line shows the approximate time, for each discharge, when the plasma went into double null configuration. (These rotation data have been smoothed in time using "nearest neighbor" smoothing.)

so the number of discharges included is fairly limited.

There are also examples of double null configuration plasmas where the plasma did not start to rotate, (1020701018). From the above information it is concluded that the double null or upper null configuration is a necessary but insufficient condition for this counter–current rotation.

If present theories of H–mode development, linking the H–mode threshold to some required edge E_r, are correct, then this observation could explain the apparent increased H–mode threshold in the double null and upper null configuration. The strong counter current rotation could lead to velocity and thereby E_r shearing, increasing the relative E_r required to cross the H–mode threshold.

5.7 Chapter Summary

This chapter has covered rotation in Ohmic plasmas. First looking at some basic data from Ohmic L–modes, a background rotation profile for a standard shot was

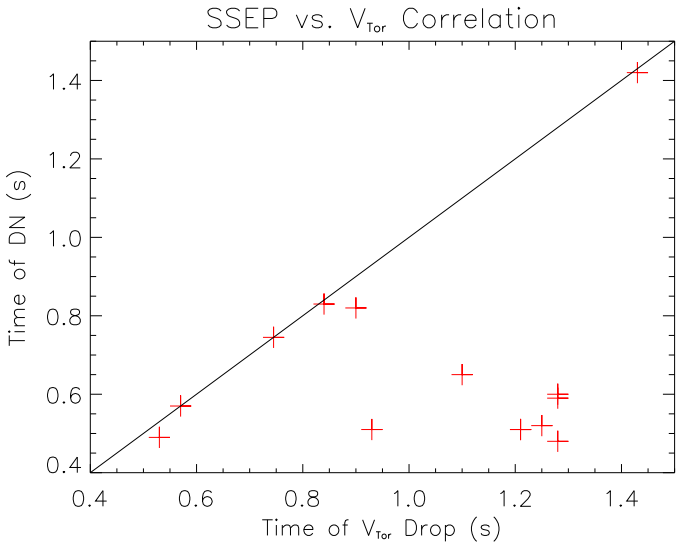

Figure 5-22: a plot of the time of double null vs. the time the plasma starts to rotate strongly in the counter current direction. The diagonal line is $y = x$.

established. A scaling of toroidal rotation of L–mode plasmas versus the plasma density was presented. Good agreement with sign, magnitude and n_e trend were found with neoclassical theory. Some data from Ohmic H–modes were then presented. The flat rotation profile in the Ohmic H–modes lead to the assumption that momentum diffusion was the only process at work in Ohmic plasmas. This conclusion led to an attempt to model the time scale for the diffusion of momentum into the plasma. The time scales were calculated based on a simple diffusion model, with diffusion coefficients $D_L \simeq 0.250\ m^2/s$ and $D_H \simeq 0.100\ m^2/s$. It was found that momentum confinement times and energy confinement times were similar in that both went up by a factor of about 3 between H–mode and L–mode. The momentum confinement times in H–mode ($\tau_{\phi,H} \sim 0.100\ s$) and L–mode ($\tau_{\phi,L} \simeq 0.030\ s$) seem to imply momentum transport is anomalous, while the diffusion coefficients are more nearly neoclassical. Finally, Ohmic rotation data dependent on magnetic geometry were presented.

Chapter 6

Rotation in ICRF Heated Discharges

One of the features of Alcator C–Mod that makes it very interesting for plasma physics studies is the high ICRF power density. Alcator is equipped with three ICRF antennas, capable of launching up to 6 MW of ICRF power. C–Mod has been able to reach power densities up to 5 MW/m^3.

6.1 ICRF Driven H-Modes

ICRF heated H–modes[113] constitute a great deal of the run time in C–Mod. The ICRF system is quite versatile, capable of launching many MW of power at a few different frequencies and with a variety of antenna phasings. This makes for many possible RF configurations and power deposition profiles. It is not surprising that a great diversity of toroidal rotation profile shapes has been seen under these varied conditions.

This chapter will focus on two shapes in particular: flat profiles and centrally peaked profiles. Towards the end of the chapter some of the other profile shapes will be shown and briefly discussed.

6.2 Flat Profiles

Many of the rotation profiles measured in ICRF plasmas are flat. Figure 6-1 is an example of such a profile. Shown here are the averaged L–mode and H–mode portions of a discharge. As in the Ohmic case, the profile starts out flat during L–mode and then starts to rise from the outside and finishes, in a fully developed H–mode, with a flat rotation profile. This can be seen in Fig. 6-2.

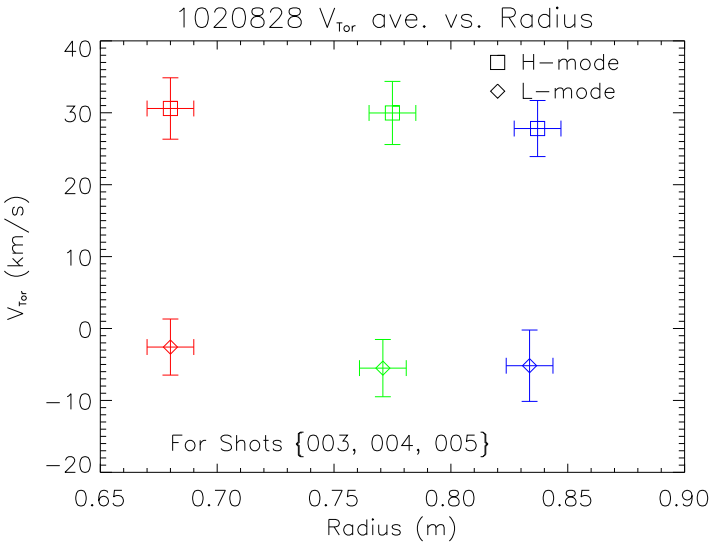

Figure 6-1: A rotation profile in an ICRF H–mode. The profile is flat during the L–mode phase of the discharge. Once the H–mode has formed the profile again becomes flat. This plot represents the average over three shots 003, 004, 005 from the 1020828 run.

In most instances of flat profiles, measurements of the toroidal rotation after the L $\rightarrow$ H transition show the outer channels rising before the core, and thus imply that the momentum responsible for the rotation originates further out in the plasma and diffuses in. Figure 6-3 shows time histories of toroidal rotation velocities for a different discharge. The outer most spectrometer view, shown in blue ($r/a \simeq 0.6$), rises first. Next, the middle channel, shown in green ($r/a \simeq 0.3$), rises. Finally, the core channel, shown in red ($r/a \simeq 0.0$) starts to rise.

Figure 6-4 shows time histories of various plasma parameters for this discharge.

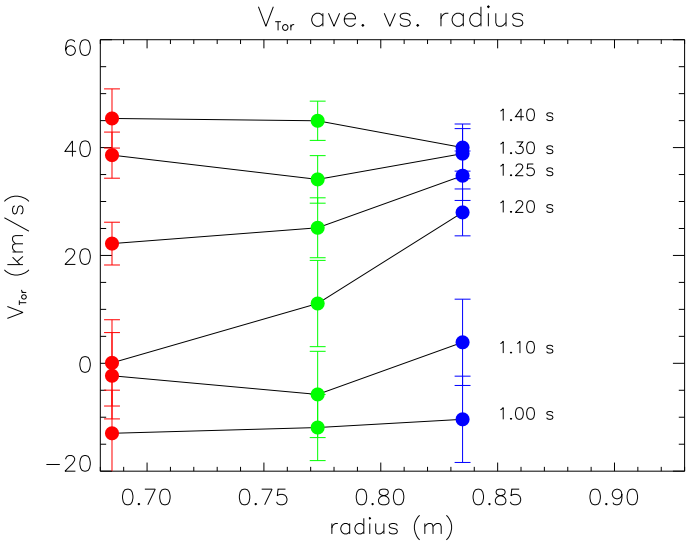

Figure 6-2: Rotation velocity profiles for different times after the L → H transition, (1.03 s). It can clearly be seen that the velocity speeds up on the outside first, and propagates inward to the core. The shapes of the intermediate profiles in time imply that the momentum originates at the edge. The flat final profile implies that the momentum diffuses in, with no evidence of convection.

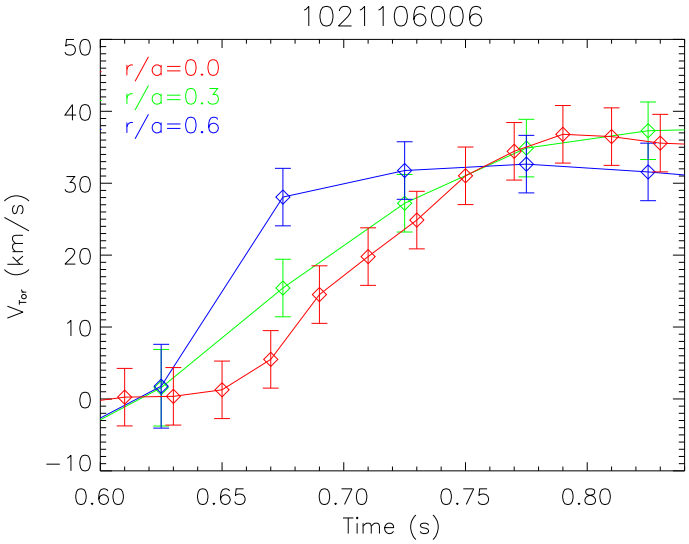

Figure 6-3: Rotation measurements for the three spectrometer views vs. time. The delay in the rotation can clearly be seen. First the outer channel starts to rotate, then the middle, and lastly the core channel. (These data have been smoothed in time using "nearest neighbor" smoothing.)

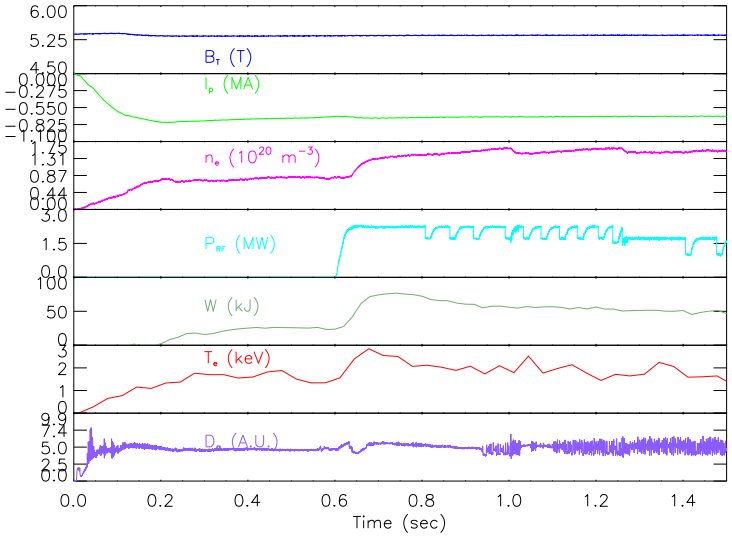

Figure 6-4: Time histories for some of the plasma parameters for the discharge in Figs. 6-3, 6-5 & 6-6. From top to bottom: B_T (T), I_P MA, n_e (10^20 m^-3), P_{RF} (MW), W (kJ), T_e (keV) and D_α emission (A.U.).

6.2.1 The Simple Model: Momentum Diffusion

Following the simple model detailed in Chapter 5, §5.3.1, a solution to the diffusion equation can be fit to the data.

Figure 6-5 is a surface plot of the solution of the diffusion equation, Eq. 5.10 to match the data in Fig. 6-3. Again, the solution has been taken to be a Bessel expansion, Eq. 5.11.

Figure 6-6 shows the spatial slices of the surface in Fig. 6-5 at the locations of the spectrometers views, plotted vs. time, with the data from Fig. 6-3 overplotted. The diffusion coefficient (D) that was used to fit these data and the implied confinement time (τ_{V_ϕ}) have been calculated again using Eq. 5.15. In this case the terminal rotation velocity (P, from the boundary conditions) was taken to be 42 km/s. The data were fit best with a diffusion coefficient $D = 0.100\ m^2/s$, which implies a confinement time $\tau_H = 0.076\ s$.

The values found for momentum purely diffusing into an ICRF heated plasma were exactly the same as those for the diffusion of momentum into an Ohmic plasma.

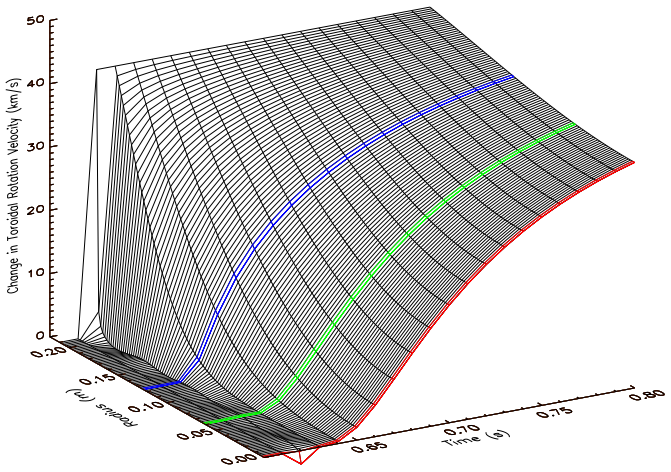

Figure 6-5: A surface of rotation velocity vs. radius and time as predicted by the simple diffusion model. An analytical solution was found in the form of a Bessel expansion. When this surface was calculated and plotted, the series was truncated at 191 Bessel modes. Residual oscillations on the solution surface are numeric artifacts.

Both plasmas were making the transition from L–mode to an EDA H–mode.

Figures 6-7 and 6-8 are a second example of rotation data fitted to the simple diffusion model. Plasma parameters for this discharge are shown in Fig. 6-9.

In this case the values for D_{V_ϕ} and τ_{V_ϕ} are found to be slightly different, but very similar. The best fit to the data gives a $D_{V_\phi,LH} = D_H = 0.050\ m^2/s$ and $D_{V_\phi,HL} = D_L = 0.200\ m^2/s$. These values for the diffusion coefficients give momentum confinement times: $\tau_{V_{\phi,LH}} = \tau_H = 0.152\ s$ and $\tau_{V_{\phi,HL}} = \tau_L = 0.038\ s$. In this case the terminal rotation velocity (P, from the boundary conditions) was taken to be 52 km/s. By using this model to describe these measurements we have been able to find both the L–mode and the H–mode momentum confinement times, in a momentum–source–free tokamak.

The values of D_H and τ_H in this discharge are about a factor of two different from the Ohmic or the previous ICRF D_H and τ_H values. The values of D_L and τ_L, however, are just about the same as the Ohmic case. Generally speaking, EDA H–modes exhibit diffusion coefficients between ~ 0.050 and $\sim 0.100\ m^2/s$, and L–modes

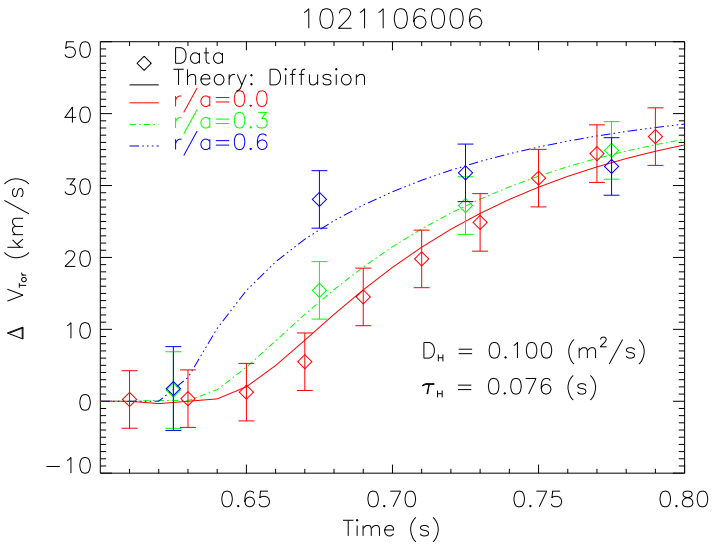

Figure 6-6: Fig. 6-5 projected into the rotation velocity – time plane, with data overplotted. There is quite a bit of scatter in the raw data, but the trend based on the simple model fits well with momentum diffusion. The diffusivities (D) and the time constants (τ) have been calculated for both the L $\rightarrow$ H and H $\rightarrow$ L. (These data have been smoothed in time using "nearest neighbor" smoothing.)

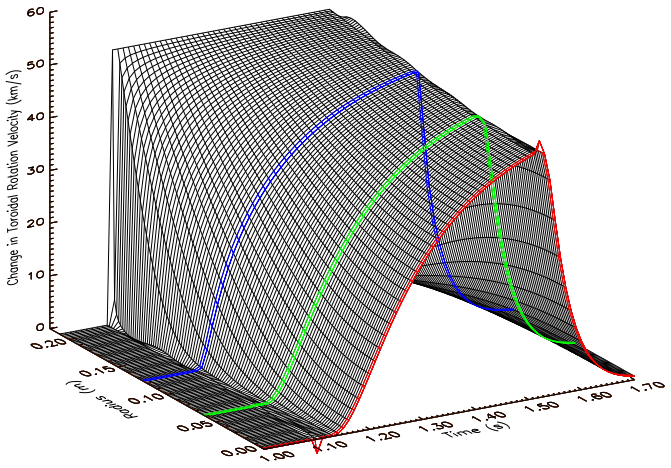

Figure 6-7: A surface plot of rotation velocity vs. radius and time as predicted by the simple diffusion model. An analytical solution was found in the form of a Bessel expansion, an infinite series of Bessel functions. When this surface was calculated and plotted, the series was truncated at 191 Bessel modes.

show diffusion coefficients of about 0.200 m^2/s – 0.250 m^2/s. The reason for the variation in these parameters is not well understood. From theory, these parameters should vary over the minor radius of the plasma, since a single value is being used to describe the diffusivity over the entire plasma, this fit parameter only represents an average value. Slight differences in profile shapes of plasma parameters can lead to different values for all transport coefficients.

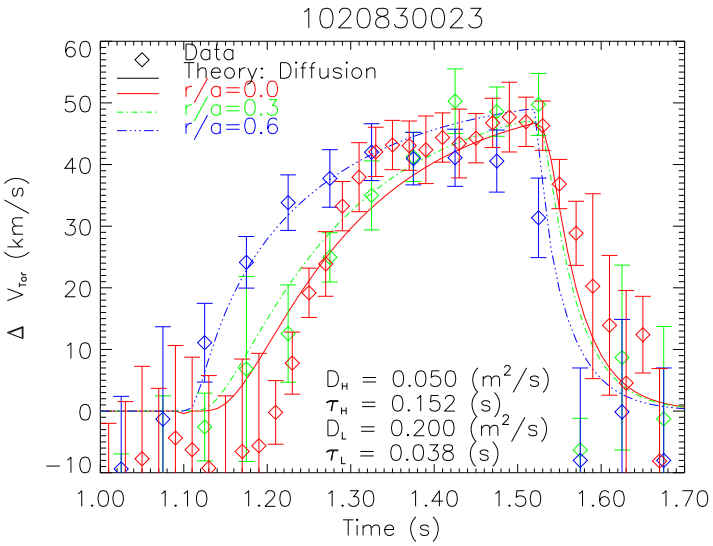

Figure 6-8: Fig. 6-7 projected into the rotation velocity – time plane, with data overplotted. There is quite a bit of scatter in the data, but the trend based on the simple model fits well with momentum diffusion. The diffusivities (D) and the time constants (τ) have been calculated for the L–mode ($D_{HL} \equiv D_L = 0.200\ m^2/s$; $\tau_{HL} \equiv \tau_L = 0.038\ s$), and H–mode ($D_{LH} \equiv D_H = 0.050\ m^2/s$; $\tau_{LH} \equiv \tau_L = 0.152\ s$), phases of the discharge. (These data have been smoothed in time using "nearest neighbor" smoothing.)

Further, in this discharge the L $\rightarrow$ H transition occurs at about 1.1 s, there is a step up in the input RF power at about 1.2 s. In both this shot and the shot in Figs. 6-3 – 6-6 the change in the stored energy (ΔW) from the L–mode to the H–mode was $\sim$ 43 kJ. In the previous shot (Figs. 6-3 – 6-6) the time for the stored energy to reach its peak value was $\sim$ 0.080 – 0.100 s. In this shot, because of the step in the RF power and time of the L $\rightarrow$ H transition, the change in the stored energy took about $\sim$ 0.180 – 0.200 s. Correspondingly, (or perhaps coincidentally,) the fitted $\tau_{\phi,H}$ has

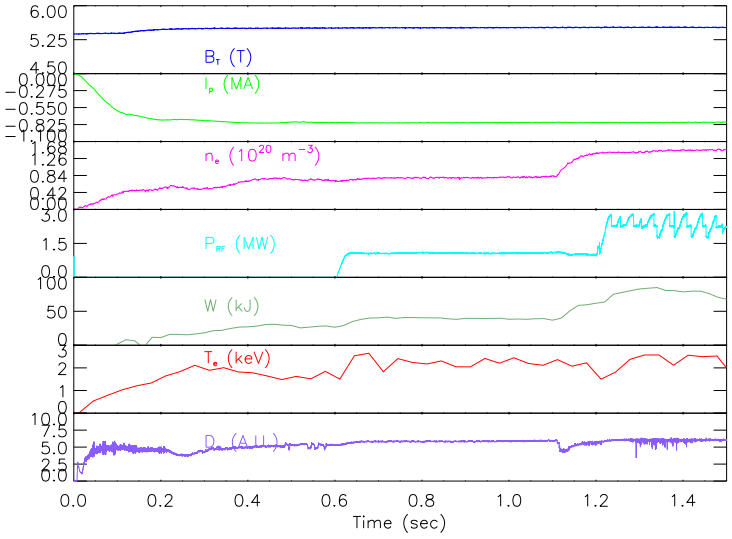

Figure 6-9: Plasma parameters for discharge in Figs. 6-7 & 6-8

changed by a factor of two. The analysis of this shot most likely is more complicated.

6.2.2 Inferred Radial Electric Field

Fig. 6-10 is a plot of the individual terms from Eq. 2.16. Again, the terms 1, 2 and 3 have been set, identically, to zero at $r/a = 0$, and these are not measured quantities. It can be seen that the dominant term is Term 1, $(V_\phi^I B_\theta.)$ Term 2, $(-\frac{(K_1+\frac{3}{2}K_2-1)}{e}\frac{\partial}{\partial r}T_i,)$ has little effect. Term 3, $(\frac{T_i}{en_i}\frac{\partial}{\partial r}n_i)$, is practically negligible.

The remaining quantities in Eq. 2.16 are measured during normal plasma operation. Figure 6-11 shows time histories of the radial electric field at the outer two spectrometer view locations, the central view has been set to zero. Figure 6-12 shows the same information in profile form.

It can be seen that like the flat profile Ohmic (EDA) H–mode, the ICRF flat profile (EDA) H–mode also has a flat E_r profile.

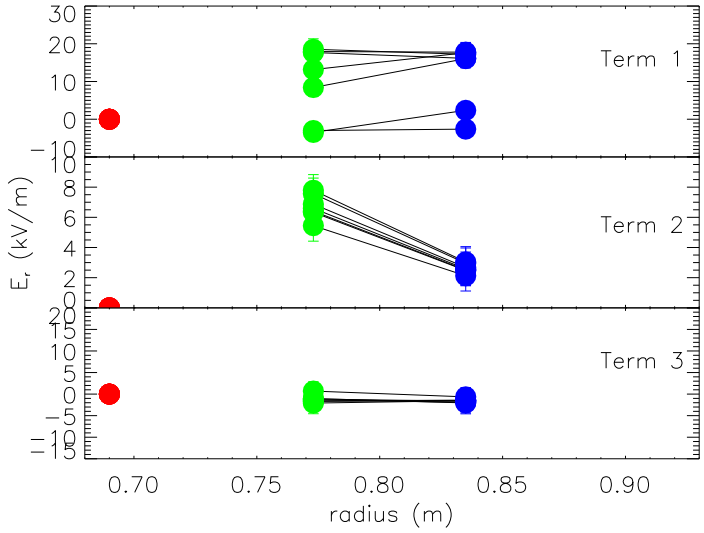

Figure 6-10: The profiles of the three terms that make up the calculation of the inferred radial electric field. Term 1 $\equiv V_\phi^I B_\theta$, Term 2 $\equiv -\frac{(K_1+\frac{3}{2}K_2-1)}{e}\frac{\partial}{\partial r}T_i$ and Term 3 $\equiv \frac{T_i}{en_i}\frac{\partial}{\partial r}n_i$. Each term has been plotted vs. radius for seven 50 ms steps during the discharge.

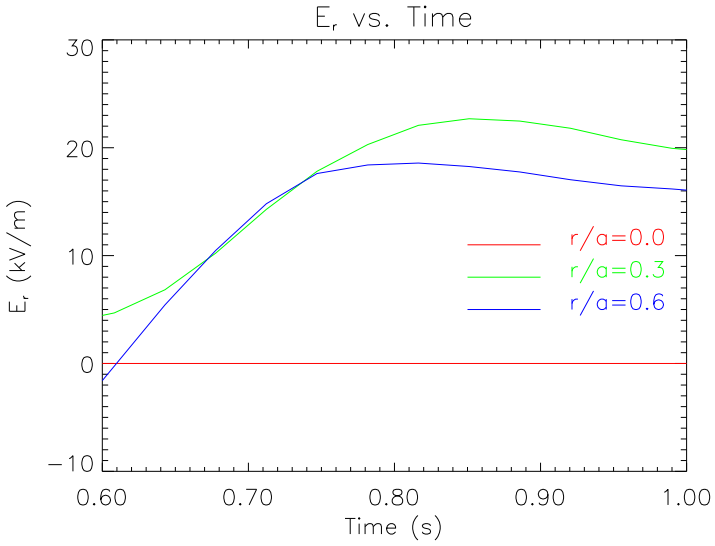

Figure 6-11: Time histories of the inferred radial electric field at the view locations of the three spectrometers.

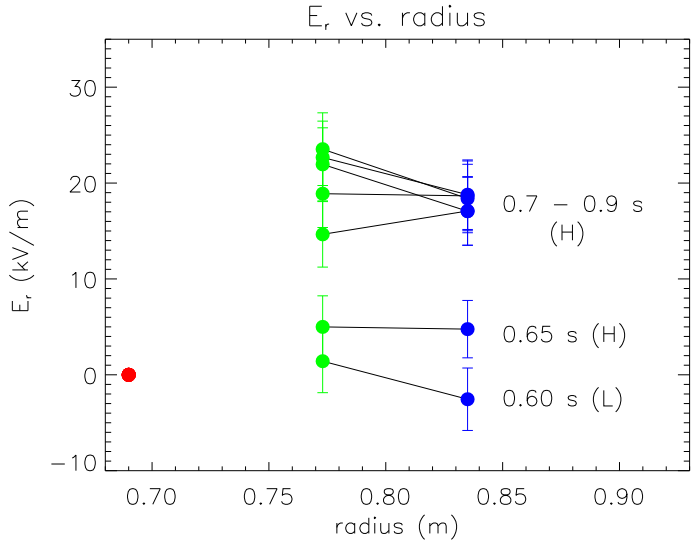

Figure 6-12: Profiles of the radial electric field at 50 ms intertals during the discharge.

6.3 Peaked Profiles

Peaked profiles are also very common in C–Mod. Fig. 6-13 shows just one example of such a profile. Figure 6-14 has some of the plasma parameters for the discharge of the profile in Fig. 6-13.

6.3.1 The Simple Model: Diffusion and Convection

For the case of peaked rotation profiles, the simple diffusion model fails to predict the appropriate profile shape. To fit these data, a slightly more complicated model, diffusion with a convection velocity that depends linearly on the radius, will be used.

Starting with Eq. 5.8:

$$\frac{\partial}{\partial t}P + \nabla \cdot \Gamma_P = 0 \tag{5.8}$$

where Γ_P is now defined as:

$$\Gamma_P = -D\frac{\partial}{\partial r}P - \frac{v_c r}{a}P \tag{6.1}$$

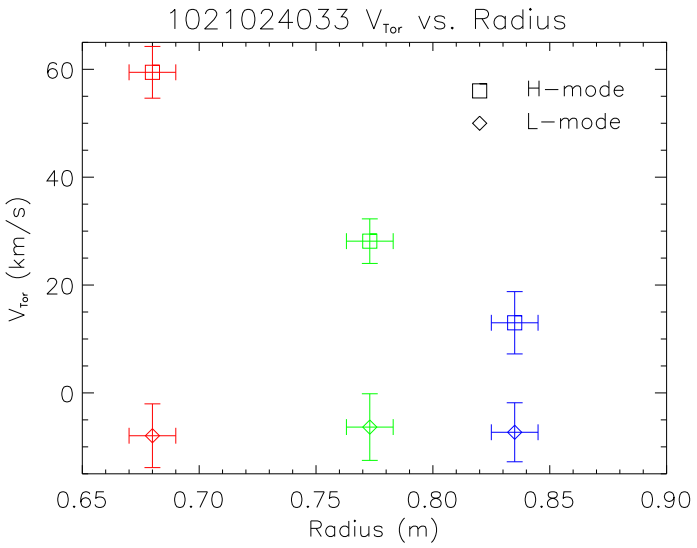

Figure 6-13: The rotation profile in an ICRF H–mode. The profile is flat during the L–mode phase of the discharge. Once the H–mode has formed the profile becomes extremely peaked in the core, and the profile is quite steep.

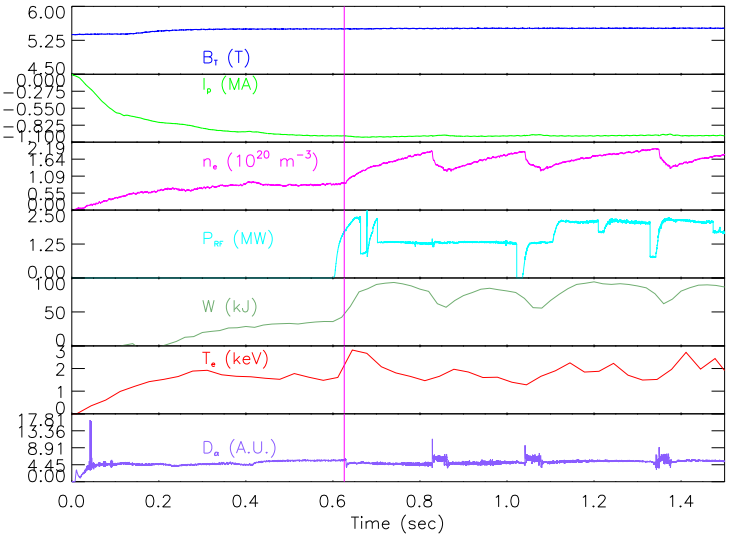

Figure 6-14: Plasma parameters for Fig. 6-13. The vertical line indicates the time of transition into the first H–mode.

again: P = $n_i m_i V$, with the assumptions that $V = V_\phi$ and the density profile is flat ($\frac{\partial}{\partial r}\ n_i = 0$). Equation 5.8, in cylindrical coordinates, then becomes:

$$\frac{\partial}{\partial t}V_\phi - D\left[\frac{\partial^2}{\partial r^2}V_\phi + \left(\frac{1}{r} + \frac{v_c r}{aD}\right)\frac{\partial}{\partial r}V_\phi + \frac{2v_c}{aD}V_\phi\right] = 0. \tag{6.2}$$

Assuming Eq. 6.2 is separable, it has a general solution

$$V_\phi(r,t) = \sum_{n=0}^{\infty} C_n \frac{1}{r}[e^{-t/\tau_n}](e^{-v_c r^2/4aD})M_{\left(\frac{\lambda_n Da + v_c}{2v_c}\right),0}(v_c r^2/4aD) \tag{6.3}$$

where: $M_{\left(\frac{\lambda_n Da+v_c}{2v_c}\right),0}(v_c r^2/4aD)$ are confluent hypergeometric functions, specifically Whittaker functions[114], and λ_n are the eigenvalues, determined from the zeros of the Whittaker functions, ($M_{\kappa(\lambda_n),0}(\frac{v_c a}{4D}) = 0.$) The time constants ($\tau_n$) are determined by the relation:

$$\tau_n = \frac{a^2}{\lambda_n D} \tag{6.4}$$

with the condition: $\lambda_{n-1} < \lambda_n,\ \forall\ n \in \mathbb{N} \Rightarrow \tau_{n-1} > \tau_n,\ \forall\ n \in \mathbb{N}$. Again, assuming an edge source, the boundary conditions:

$$V(a,t) = \begin{cases} 0, & t < t_{L\to H} \\ P, & t_{L\to H} \le t \le t_{H\to L} \\ 0, & t > t_{H\to L} \end{cases} \tag{6.5}$$

are imposed.

The radial portion of this solution satisfies the orthogonality condition[115]:

$$\int_0^a V_{\phi,R}(\frac{\lambda_n r}{a})V_{\phi,R}(\frac{\lambda_m r}{a})\frac{2\pi r}{a^2}dr = \delta_{nm}. \tag{6.6}$$

The coefficients C_n can then be determined by the relation:

$$C_n = \frac{\int_0^a f(r)V_{\phi,R}(\frac{\lambda_n r}{a})r dr}{\int_0^a V_{\phi,R}^2(\frac{\lambda_n r}{a})r dr} \tag{6.7}$$

where: $f(r)$ is a function for the initial conditions, in this case zero through out the

radius, and P at the edge, ($r = a$.)

In this case the slowest eigenvalue, $\tau_1 \simeq 70\ ms$. The higher order modes, (τ_n, $n \geq 2$,) have time scales of 3.5 ms or less, ($\tau_2 \simeq 3.5\ ms$ [116].) The contribution these higher order modes make to the solution will be very short lived, less than the first 10 ms, clearly not perceptible with the spectrometer's current time resolution[1].

To model the data, on this relatively long time scale, we can approximate Eq. 6.3 as:

$$V_\phi(r,t) \simeq C_1 \left[e^{-v_c r^2/2aD} - [e^{-t/\tau_1}] \frac{1}{r} (e^{-v_c r^2/4aD}) M_{(\frac{\lambda_1 Da + v_c}{2v_c}),0}(v_c r^2/4aD) \right] \tag{6.8}$$

with $C_1 = V_{Term} = e^S P$, S is the convection parameter Eq. 6.10, $\lambda_1 = 1.57$. Equation 6.8 is the first order solution to Eq. 6.2. The higher order modes decay away in well under 20 ms justifying this approximation[115].

Seguin *et. al.* [116], determined τ_1 could be approximated over a large range of S, ($|S| \leq 50$,) as:

$$\tau_1 \simeq \frac{(77 + S^2)}{(56 + S^2)} \left[\frac{e^S - S - 1}{4S^2} \right] \frac{a^2}{D} \tag{6.9}$$

where, the convection parameter, (S,) is:

$$S = \frac{a v_c}{2D}. \tag{6.10}$$

Eqs. 6.8 – 6.10, with D and v_c as free parameters, represent an approximate solution that can be used to fit the data, with a slower than 10 ms time scale.

Figure 6-15 is a surface plot of rotation velocity vs. space and time. This discharge had two complete L $\rightarrow$ H, H $\rightarrow$ L transition cycles, and the surface reflects this. The surface was generated using $D_H = 0.400\ m^2/s$ and $v_c = 12\ m/s \Rightarrow \tau_H \simeq 0.070\ s$. It should be noted that the rotation velocity at the edge of the plasma is predicted to be

[1]To insure that this was true a numeric solution to Eq. 6.2 was also found and it did not differ from the analytic solution on a 10 ms timescale.

quite small ($P \simeq 4$); this is due to the convection velocity which varies linearly with radius. The pinch effect on any momentum that originates at the edge is greatest at the edge of the plasma.

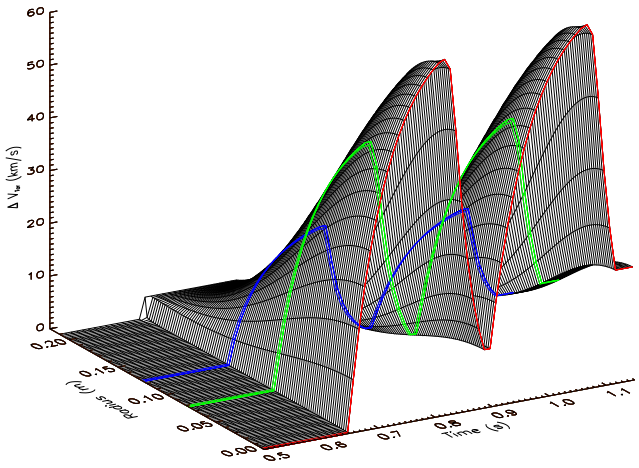

Figure 6-15: A surface plot of toroidal rotation velocity vs. space and time for a discharge with a peaked rotation profile.

Figure 6-16 is a plot of spatial slices of the surface in Fig. 6-15, that correspond to the radii of the spectrometer views. Over plotted in this figure are the data from this shot. The agreement is certainly passable, considering the simplicity of the model.

Figure 6-17 are some of the plasma parameters for the shot in Figs. 6-15 and 6-16.

6.3.2 Momentum Confinement Time

Unfolding the proper time scale for this equation (Eq. 6.3) is slightly more complicated than in the simple diffusion model. Using Eq. 6.9 to calculate the confinement time for the L $\rightarrow$ H transition, with $D_H = 0.400\ m^2/s$ and $v_c = 12\ m/s$, $S = 3.15$, $\tau_H \simeq 0.070\ s$. This is an ELM free H–mode, the impurity confinement time is known to be long ($\tau_{imp} \sim 0.1\ s$).

The convection parameter S is essentially a measure of the steady state radial profile shape. The confinement time (τ_1) is essentially a measure of the shape of the

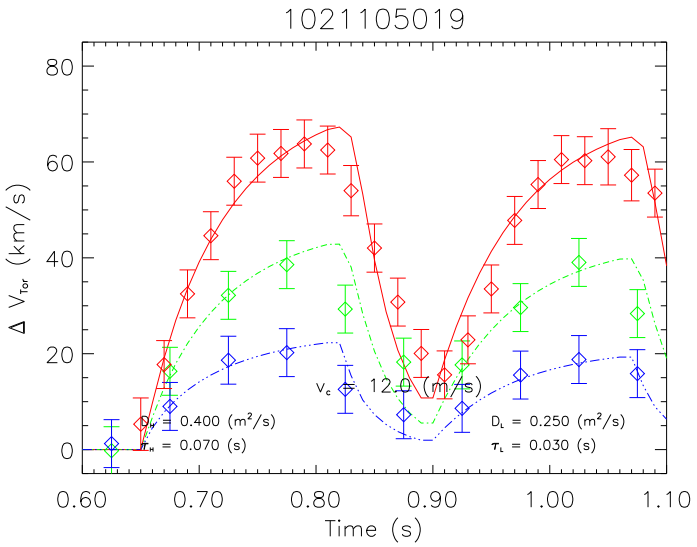

Figure 6-16: A plot of rotation velocity vs. time. Over plotted are the data from this shot. In the lower portion of the figure are the diffusion coefficients, the confinement times and the convection velocity used in the diffusion and convection model to fit this data. (These data have been smoothed in time using "nearest neighbor" smoothing.)

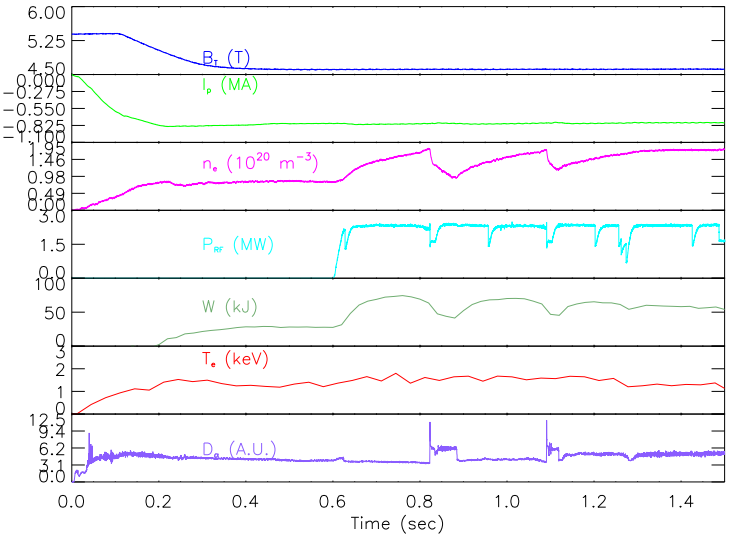

Figure 6-17: Plasma parameters for the discharge in Figs. 6-15 and 6-16.

time history. The peak value, together with these two parameters (S and τ_1) can uniquely define any $V_\phi(r,t)$ surface that satisfies Eq. 6.2. Figure 6-18 is a plot of τ_1 vs. S for various values of both v_c and D_H. Inset in this figure is a plot of the steady state profile shape for the convection parameter value fitted to these data, (S = 3.15.)

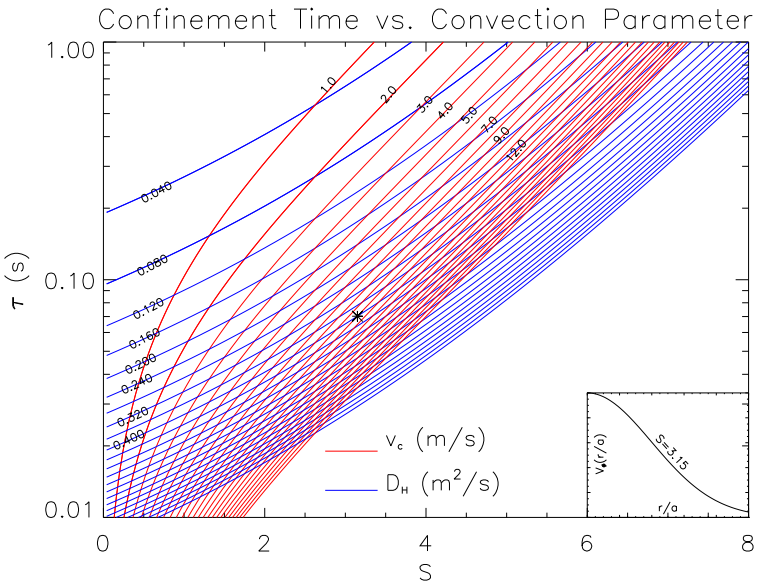

Figure 6-18: Confinement time (τ_1) vs. Convection Parameter (S). Lines of constant convection velocity (v_c) are plotted in red. Lines of constant diffusivity (D) are plotted in blue. The asterisk (*) represents the choice of S and τ or v_c and D_H for this discharge. The inset figure is a plot of the steady state profile shape, ($S = 3.15$,) for the peaked discharge discussed in detail in this chapter, (Figs. 6-15 – 6-17.)

6.3.3 Inferred Radial Electric Field

Fig. 6-19 is a plot of the individual terms from Eq. 2.16. Again, the terms 1, 2 and 3 have been set, identically, to zero at $r/a = 0$, and these are not measured quantities. It can be seen that the dominant term is Term 1, ($V_\phi^I B_\theta$.) Term 2, ($-\frac{(K_1+\frac{3}{2}K_2-1)}{e}\frac{\partial}{\partial r}T_i$,) has the least effect. Term 3, ($\frac{T_i}{en_i}\frac{\partial}{\partial r}n_i$), is about a factor of 2 less than Term 1.

The remaining quantities in Eq. 2.16 are measured during normal plasma operation. Figure 6-20 shows time histories of the radial electric field at the outer two

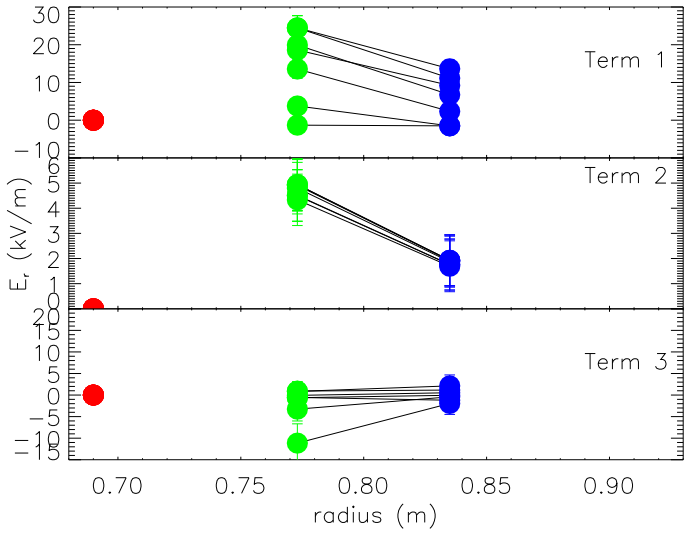

Figure 6-19: The profiles of the three terms that make up the calculation of the inferred radial electric field. Term 1 $\equiv V_\phi^I B_\theta$, Term 2 $\equiv -\frac{(K_1+\frac{3}{2}K_2-1)}{e}\frac{\partial}{\partial r}T_i$ and Term 3 $\equiv \frac{T_i}{en_i}\frac{\partial}{\partial r}n_i$. Each term has been plotted vs. radius for seven 50 ms steps during the discharge.

spectrometer view locations, the central view has been set to zero. Figure 6-21 shows the same information in profile form.

It can be seen that The E_r profile is highly sheared in the region r/a 0.3 – 0.6. These data are consistent with the findings from DIII-D[79].

6.4 Other Shapes

Other variations on the previously mentioned profile shapes have been seen with the spectrometer array, flatter, more peaked, less peaked, etc. These other profile shapes could be fitted using this model, by varying the convection velocity and or the diffusion coefficient. It seems logical that the mechanism that drives the rotation peaking, has a continuous range. This means that shapes anywhere from flat to fully peaked would not only be possible, but expected.

In addition to the two shapes focused on in this chapter, a class of hollow profiles has been seen. A simple model to describe these has not been developed here. Figure

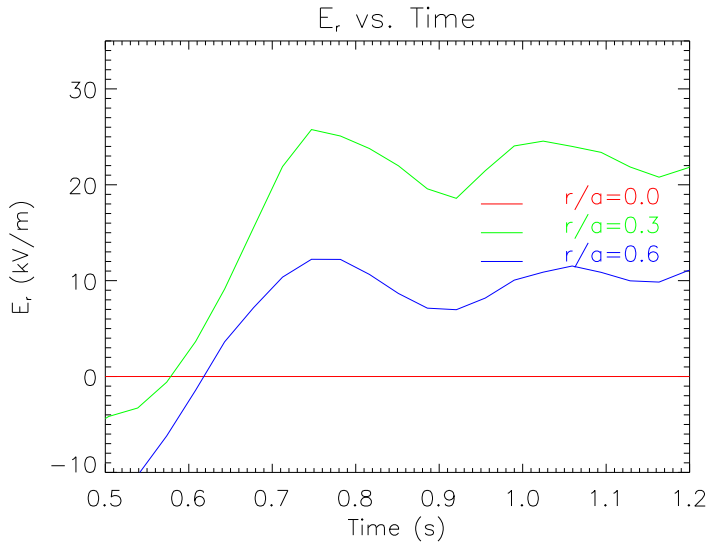

Figure 6-20: Time histories of the inferred radial electric field at the view locations of the three spectrometers.

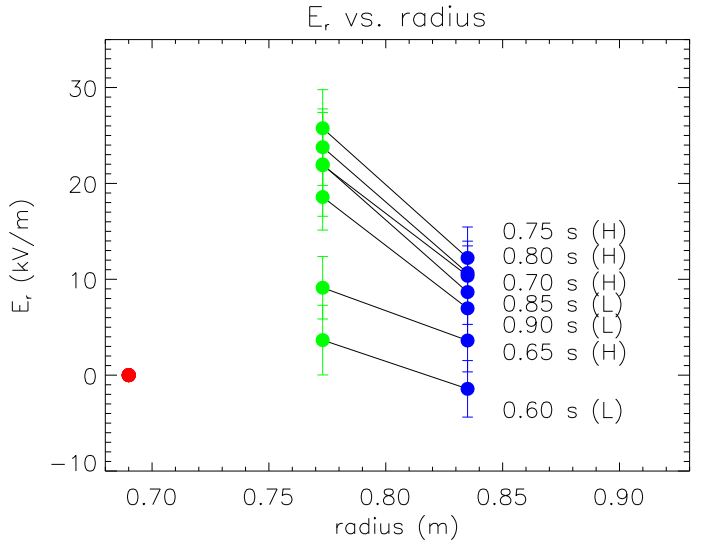

Figure 6-21: Profiles of the radial electric field at 50 ms intervals during the discharge.

6-22 is an example of a hollow profile.

Figures 6-23 and 6-24 are examples of some of the other profile shapes that have been seen.

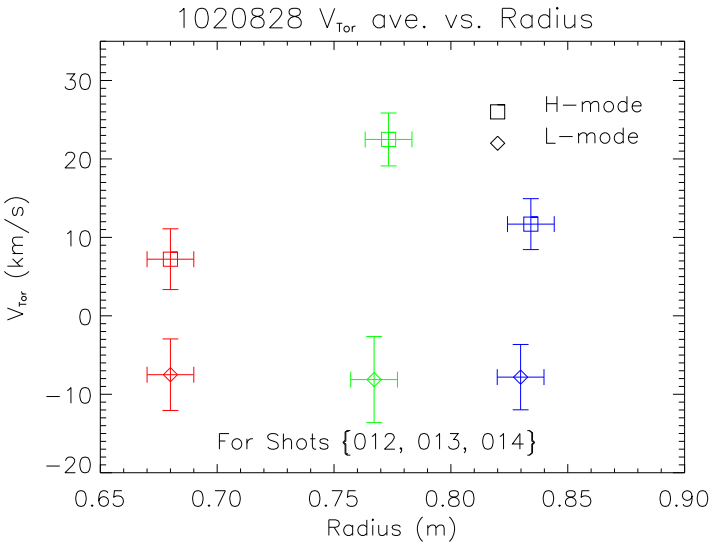

Figure 6-22: The rotation profile in an ICRF H–mode. The profile is flat during the L–mode phase of the discharge. Once the H–mode has formed the profile becomes steep on the outside, and very hollow towards the core.

Originally, it was thought that the location of the peak in the rotation profile might be linked to the ICRF resonance location. There does seem to be a link, but it is not totally straight forward. More will be said about this in the future work section, §8.2

6.5 Comparison With Magnetics

Magnetohydrodynamic reconnection events known as the sawtooth crashes ($n = 1$, $m = 1$ tearing modes) present an alternative method of deciphering some information about plasma rotation. During a few ICRF heated discharges rotation data from the magnetics diagnostics[117] are available. Figures 6-25 and 6-26 have the x–ray rotation data, the simple model, (diffusion or diffusion and convection,) and the magnetics data plotted together, for the discharges in Figs. 6-6 and 6-16, respectively.

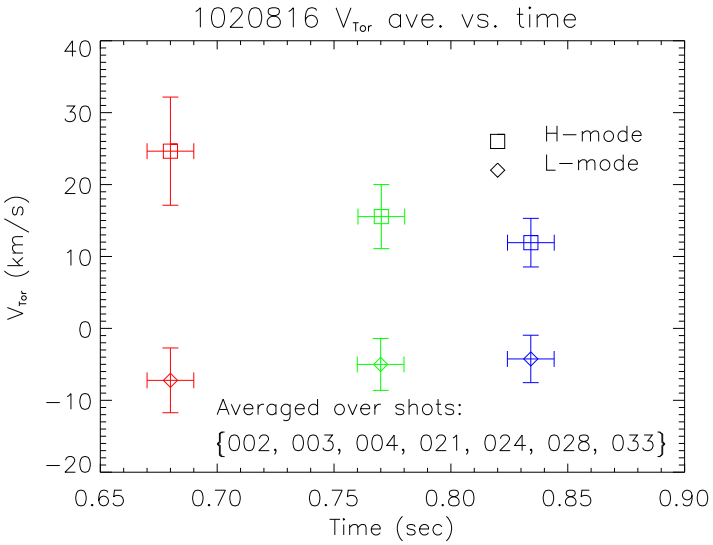

Figure 6-23: The rotation profile in an ICRF H–mode. The profile is flat during the L–mode phase of the discharge. Once the ICRF comes on the profile becomes peaked on axis.

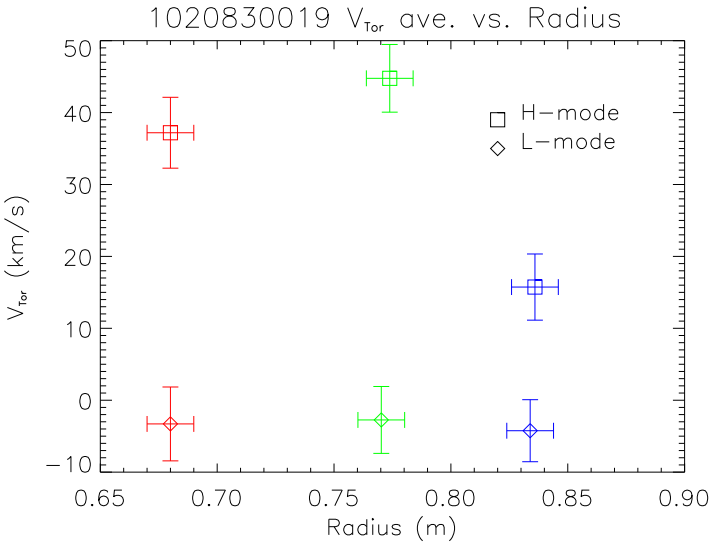

Figure 6-24: The rotation profile in an ICRF H–mode. The profile is flat during the L–mode phase of the discharge. Once the H–mode has formed the profile becomes very steep on the outside, and hollow towards the core.

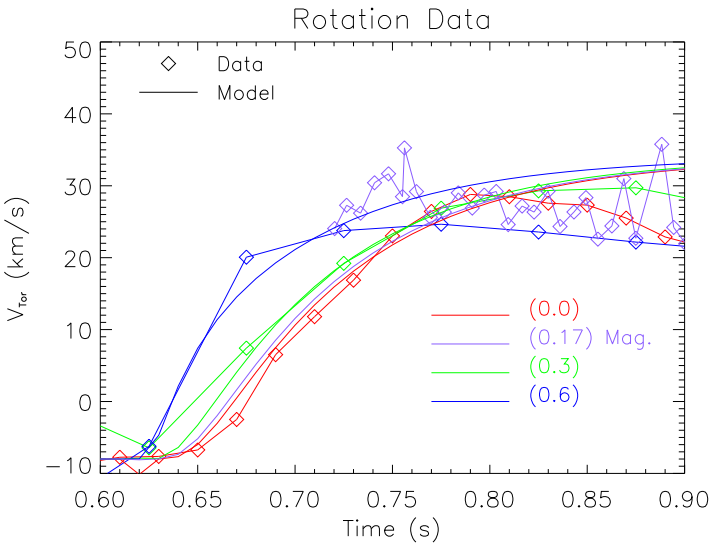

Figure 6-25: Rotation data vs. time for four radii. The red ($r/a \simeq 0.0$), green($r/a \simeq 0.3$), and blue ($r/a \simeq 0.6$) correspond to the data from the x–ray spectrometers. The purple data points ($r/a \simeq 0.17$) are from the magnetics diagnostics. These data are essentially the rotation frequency, (here multiplied by 2πR,) at the sawtooth radius, or the q = 1 surface. The smooth solid curves are from the simple model. These are the same data as in Fig. 6-6.

In Fig. 6-6 the x–ray data were shifted down by 8 km/s, (the L–mode baseline.) The magnetics data also seem to agree quite well with the model, error bars for the magnetics data are about 50%. Figure. 6-26 is a peaked or ELM–free discharge.

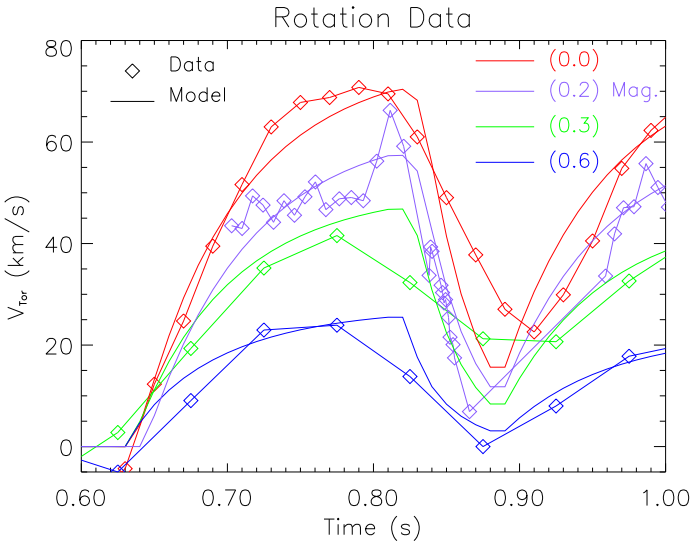

Figure 6-26: Rotation data vs. time for four radii. The red ($r/a \simeq 0.0$), green($r/a \simeq 0.3$), and blue ($r/a \simeq 0.6$) correspond to the data from the x–ray spectrometers. The purple data points ($r/a \simeq 0.2 = r(q{=}1)$) are from the magnetics diagnostics. The smooth solid curves are from the simple model. These are the same data as in Fig. 6-6.

6.6 Error Analysis

6.6.1 Measurement Error

Analysis of measurement error in the ICRF case is propagated in the same manner as in the Ohmic case, §5.5 of Chapter 5.

The analysis of error for the radial electric field was done in the same manner as in the Ohmic case, §5.5.1 of Chapter 5.

6.6.2 Model Error and Sensitivity

The error in the model fit comes from the fitting of the free parameters. In the case of the flat profiles, associated with EDA H-mode, (Figs. 6-5, 6-6, 6-7 and 6-8,) the

diffusivity is the only free parameter. In the case of the ELM-free discharge, (Figs. 6-15 and 6-16,) both the diffusivity and the convection velocity are free parameters.

In this chapter, just as in the last, the "goodness of fit" for the simple diffusion cases have been checked by minimizing the χ^2 error statistic and calculating the reduced chi squared χ^2_ν, (see §5.5.2). Figures 6-27, 6-28 and 6-29 are plots of χ^2 vs. D for the fits in Figs. 6-5, 6-6 (D_H) and 6-7, 6-8, (D_H) & (D_L).

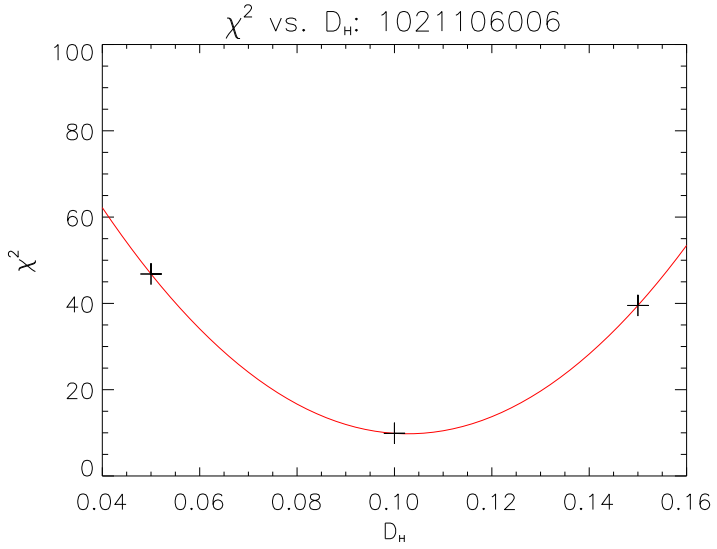

Figure 6-27: A plot of the χ^2 error statistic vs. D_H the fitted diffusivity, for the fit in Figs. 6-5 and 6-6. The fit parameter is almost the absolute minimum of the χ^2 curve.

For the fit to D_H in Figs. 6-5 and 6-6, $\chi^2_\nu = 0.785$. The χ^2 vs. D plot tells us to expect D to be in the range 0.075 – 0.130 m^2/s. For the fit to D_H in Figs. 6-7 and 6-8, $\chi^2_\nu = 2.79$, with D_H in the range 0.01 – 0.08 m^2/s, and for the fit to D_L, $\chi^2_\nu = 7.5$, with D_L in the approximate range 0.100 – 0.500 m^2/s.

The fit for the diffusion and convection model, have also been checked by minimizing the χ^2 error statistic. However, the process is slightly different for a fit with two parameters. The χ^2 error statistic is defined just as it was in §5.5.2:

$$\chi^2 \equiv \sum_i \sum_j \left\{ \frac{1}{\sigma_{ij}^2} [y_{ij} - y(x_i, x_j)]^2 \right\}. \qquad 5.23$$

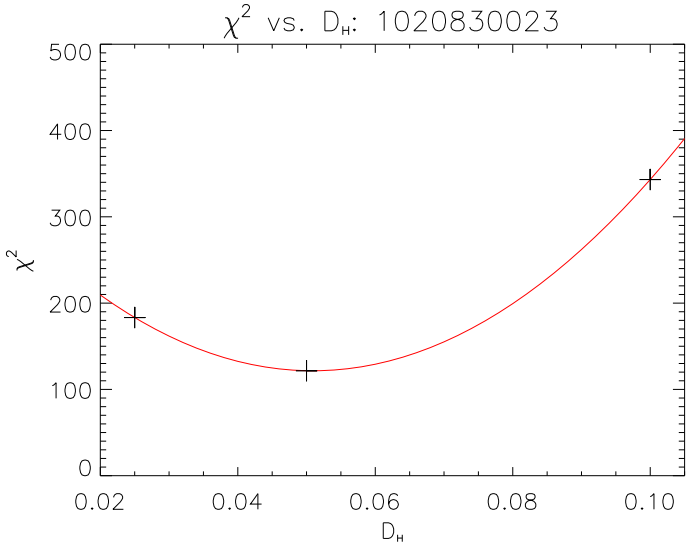

Figure 6-28: A plot of the χ^2 error statistic vs. D_H the fitted diffusivity, for the fit in Figs. 6-7 and 6-8. The fit parameter is almost the absolute minimum of the χ^2 curve.

Minimizing is then done for each of the parameters, looking for an absolute minimum in the χ^2 surface, (or possibly hyper-surface of some sort.) Minimization is then achieved by taking the partial derivative of χ^2 with respect to each of the parameters a_k and solving for zeros, that is:

$$\begin{aligned}\frac{\partial \chi^2}{\partial a_k} &= \frac{\partial}{\partial a_k} \sum_i \sum_j \left\{ \frac{1}{\sigma_{ij}^2} [y_{ij} - y(x_i, x_j)]^2 \right\} = 0 \\ &= -2 \sum_i \sum_j \left\{ \frac{1}{\sigma_{ij}^2} [y_{ij} - y(x_j, x_i)] \frac{\partial y(x_i, x_j)}{\partial a_k} \right\} \end{aligned} \tag{6.11}$$

This minimization has been done for this fit ($a_k = D$, v_c) and the χ^2 surface has been contour plotted in Fig. 6-30.

From the χ^2 in Fig. 6-30, the two parameter fit of D_H and v_c gives a reduced chi squared of $\chi^2_\nu = 1.16$. Again, from the χ^2 vs. v_c, (Fig. 6-31,) and χ^2 vs. D, (Fig. 6-32,) plots we deduce that D_H should be in the range 0.310 – 0.470 m^2/s and v_c could be anywhere between $\sim$ 10 – 14 m/s.

Figure 6-33 is three plots showing the sensitivity of the fit in Fig.6-3 – 6-6 to the

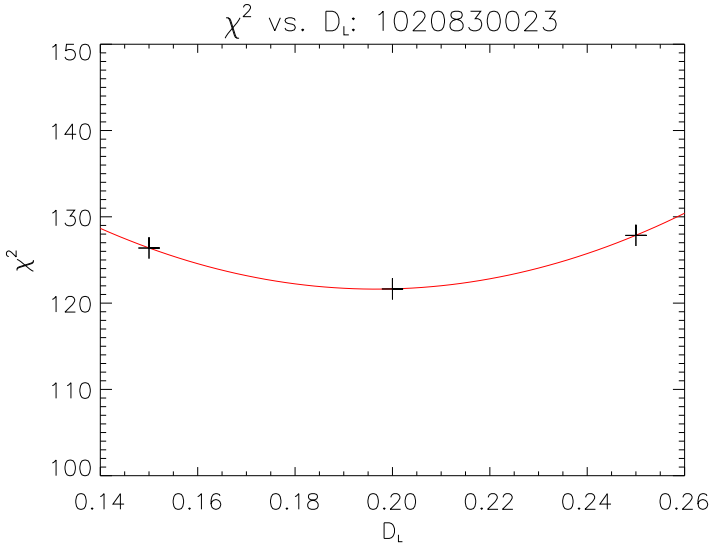

Figure 6-29: A plot of the χ^2 error statistic vs. D_L the fitted diffusivity, for the fit in Figs. 6-7 and 6-8. The fit parameter is almost the absolute minimum of the χ^2 curve. (note: the zero has been suppressed on this plot.))

value of P. Figure 6-34 is three plots showing the sensitivity of the fit in Fig. 6-7 and 6-8 to the value of P. Figure 6-35 is three plots showing the sensitivity of the fit in Fig. 6-15 and 6-16 to the value of the terminal rotation velocity, (V_{Term}.) This is essentially the same as varying P the boundary condition, ($P = 4$, in this case.)

6.7 Discussion

It was noticed that flat rotation profiles corresponded to EDA H–modes, while peaked rotation profiles corresponded to Edge Localized Mode free (ELM – free) discharges. A more thorough quantification of this should be undertaken.

These are quite simple models of the rotation velocity profile in the plasma. Two very interesting aspects to these models are that they are so simple yet accurate, and that this is the same behavior as is seen in the transport of particles[2].

In the limit that $v_c \rightarrow 0$, the diffusion and convection model reduces to simple

[2]This should not be too surprising because it is the particles that carry the momentum.

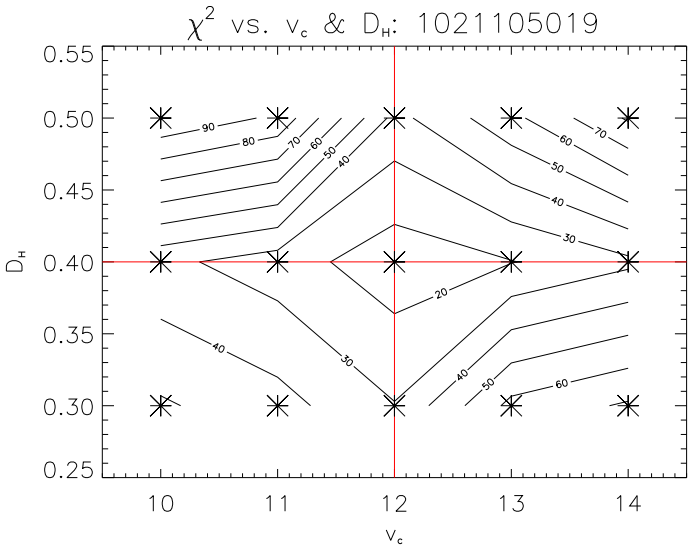

Figure 6-30: A contour plot of the χ^2 error statistic vs. v_c the convection velocity and D_H the fitted diffusivity, for the fit in Figs. 6-15 and 6-16. The fit parameter is almost the absolute minimum of the χ^2 surface.

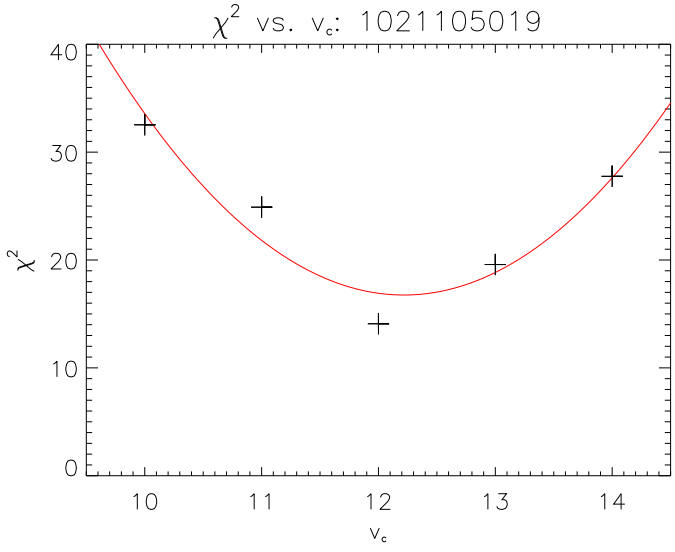

Figure 6-31: A plot of the χ^2 error statistic vs. v_c the convection velocity, for the fit in Figs. 6-15 and 6-16. The fit parameter is almost the absolute minimum of the χ^2 curve for this diffusivity.

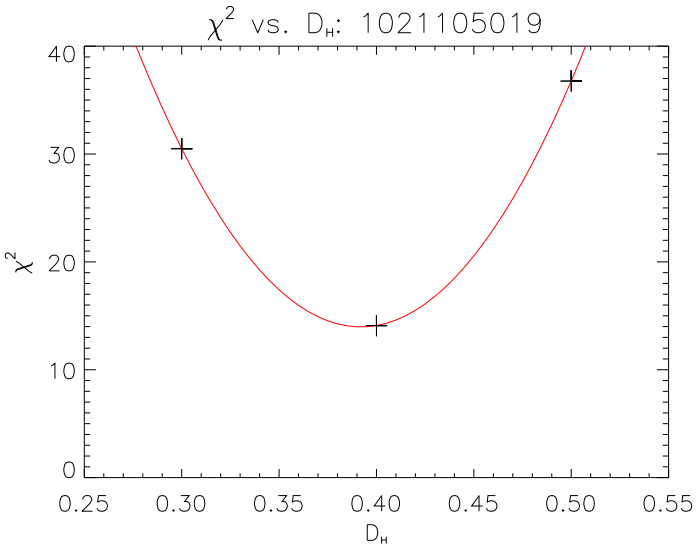

Figure 6-32: A plot of the χ^2 error statistic vs. D_H the fitted diffusivity, for the fit in Figs. 6-15 and 6-16. The fit parameter is almost the absolute minimum of the χ^2 curve for this convection velocity.

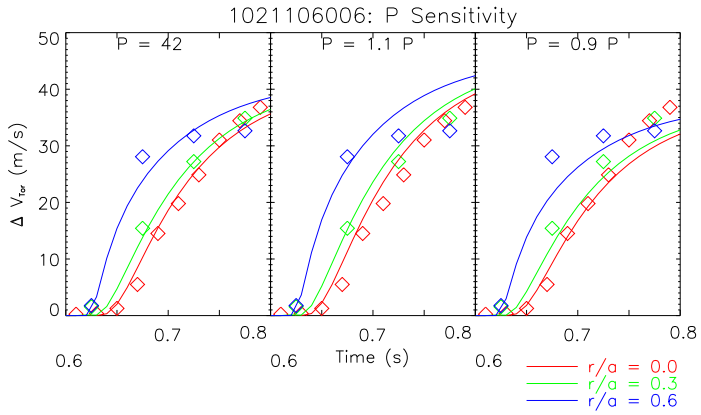

Figure 6-33: The three frames show the fit over plotted on the data for the discharge presented in Figs. 6-3 – 6-6, the fit if the boundary condition P is increased by 10% and the fit if the boundry condition P is decreased by 10%.

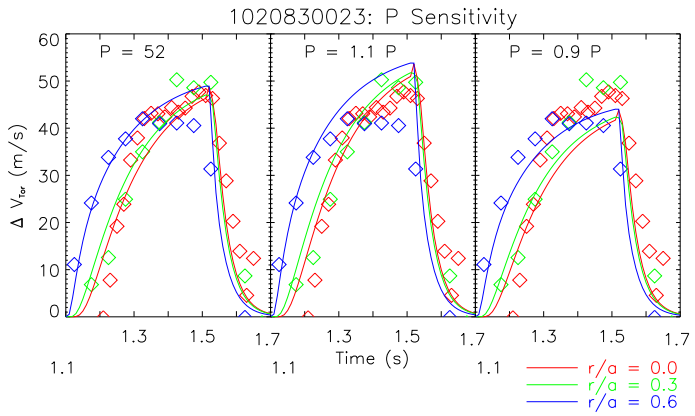

Figure 6-34: The three frames show the fit over plotted on the data for the discharge presented in Figs. 6-7 and 6-8, the fit if the boundary condition P is increased by 10% and the fit if the boundry condition P is decreased by 10%.

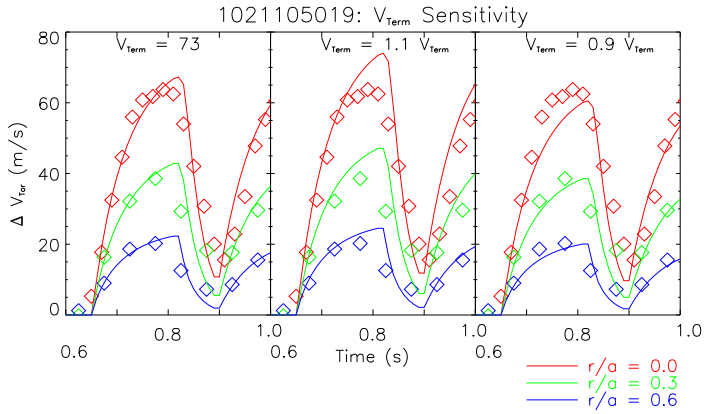

Figure 6-35: The three frames show the fit over plotted on the data for the discharge presented in Figs. 6-15 and 6-16, the fit if the terminal rotation velocity V_{Term} is increased by 10% and the fit if the terminal rotation velocity V_{Term} is decreased by 10%.

τ In s	R. NC. $\tau_{U_{\parallel,i}vis}$	R. NC. $\tau_{U_{\parallel,i}f.l.r.}$	SNC. $\tau_{U_{\parallel,i}}$	SNC. $\tau_{U_{\parallel,i}}$	Simple Model τ_{V_ϕ}	N.C. τ_{NC}
Shot	Eq. 2.20	Eq. 2.21	Eq. 2.22	Eq. 2.25	Eq. 5.15 or 6.9	$\tau_\phi = \frac{10}{\lambda_0 \rho_i^2 \nu_{ii}}$
1021106006	6414	0.0022	2527	162	0.076	$0.006 \sim 0.015$
1020830023	2839	0.0035	1688	108	0.038 (L)	$0.003 \sim 0.004$
					0.152(H)	$0.006 \sim 0.015$
1021105019	3713	0.0027	1820	117	0.030 (L)	$0.003 \sim 0.004$
					0.070 (H)	$0.006 \sim 0.015$

Table 6.1: Momentum confinement times from revisited neoclassical theory, subneoclassical theory, and neoclassical theory for the data presented in this chapter. Also see Fig. 5-11 for diffusivities.

diffusion. In general one should fit both the diffusion coefficient and the convection velocity for all the shots and determine $v_c \simeq 0$ from the fit. If, however, S the convection parameter, is less than ~ 0.1 the shape is essentially, indistinguishable from zero, as far as the spectrometer is concerned. Thus in "flat" discharges, ($S \sim 0.1$,) we use the case of simple diffusion[3], ($v_c = 0$.)

Table 6.1 lists most of the discharges mentioned in this chapter, and the momentum confinement times as calculated by revisited neoclassical theory (§2.2) subneoclassical theory (§2.3) and the appropriate simple model, either pure diffusion or diffusion and convection. This information is also plotted, along with the Ohmic data, in Fig. 6-36, a τ vs. S plot, (similar to Fig. 6-18.) Error bars for these data were created using the χ^2 from §5.5.2 and §6.6.2.

It is worth pointing out that the time dependence that the rotation exhibits in these ICRF discharges (and the Ohmic discharges as well), has the same time dependence that was predicted by Chang[25] in §2.4.2. *i.e.*:

$$V_\phi \propto V_\phi^0 (1 - e^{-t/\tau_\phi}) \tag{6.12}$$

where V_ϕ^0 is the terminal rotation speed, and it has been assumed that $\tau_\phi \simeq \tau_E$.

[3]As per Occam's razor

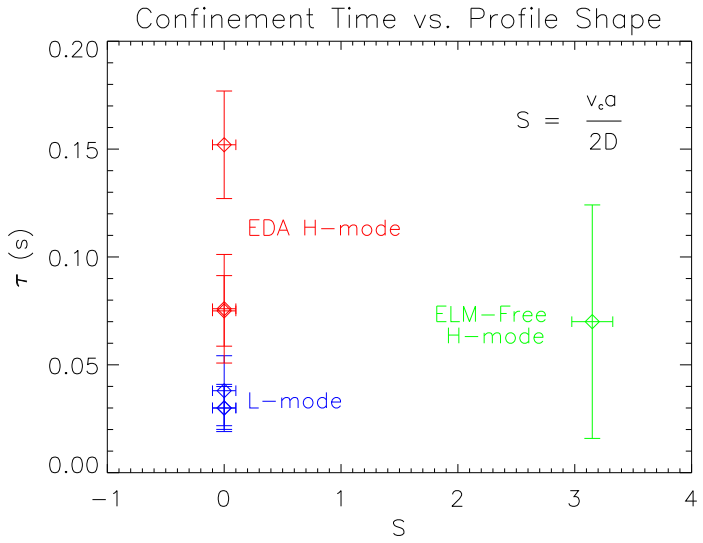

Figure 6-36: Confinement time Eq. 6.9 vs. convection parameter Eq. 6.10 for the discharges in this and the preceeding chapter. Error bars were generated based on the χ^2 error statistics, and the assumption that "flat" profiles had $S \leq 0.1$

6.8 Chapter Summary

In this chapter data have been presented from ICRF heated H–mode discharges. Two profile shapes have been focused on here, flat profiles and peaked profiles.

Flat profiles have been found to fit a simple model of pure momentum diffusion. Momentum diffusion coefficients and confinement times have been calculated based on this model. These profiles correspond to EDA H–modes.

Peaked profiles have been presented and a slightly more complicated model including both diffusion and convection was utilized to fit these data. The simple model seems again to do quite a good job fitting the data, thus offering a simple explanation for the physical processes at work in the plasma. Momentum diffusion coefficients and confinement times have been calculated based on this model. These Profiles correspond to ELM–Free H–modes.

Chapter 7

Internal Transport Barrier Discharges

A very advantageous mode of plasma operation includes Internal Transport Barriers (ITBs). ITBs lead to improved confinement in the core of the plasma and an enhanced bootstrap current fraction[43, 44]. On Alcator C–Mod, ITBs are most easily recognized by a peaking of the core density[1]. In many instances this can directly, in real time, be seen in the visible light emission from a wide angle camera.

Figure 7-1 is a digital photo of a plasma with an ITB, through a wide angle camera lens. The center of the photo is dominated by the central column of the tokamak. The view is such that a torus of increased intensity can be seen encircling the central column; this is the ITB.

When an ITB forms, the characteristic behavior of the toroidal rotation is a drop in velocity, ultimately leading to a reversal in rotation direction, *i.e.* eventually a slightly negative (counter-current) toroidal rotation velocity. The profile tends to have a mostly hollow shape. The region inside the barrier has zero rotation velocity, or slightly negative, while the region outside the barrier has a slightly positive toroidal rotation velocity.

[1]Discrepancies in the definition of an ITB lead to some ambiguity. Properly, ITBs should be defined in terms of pressure, not just density or temperature.

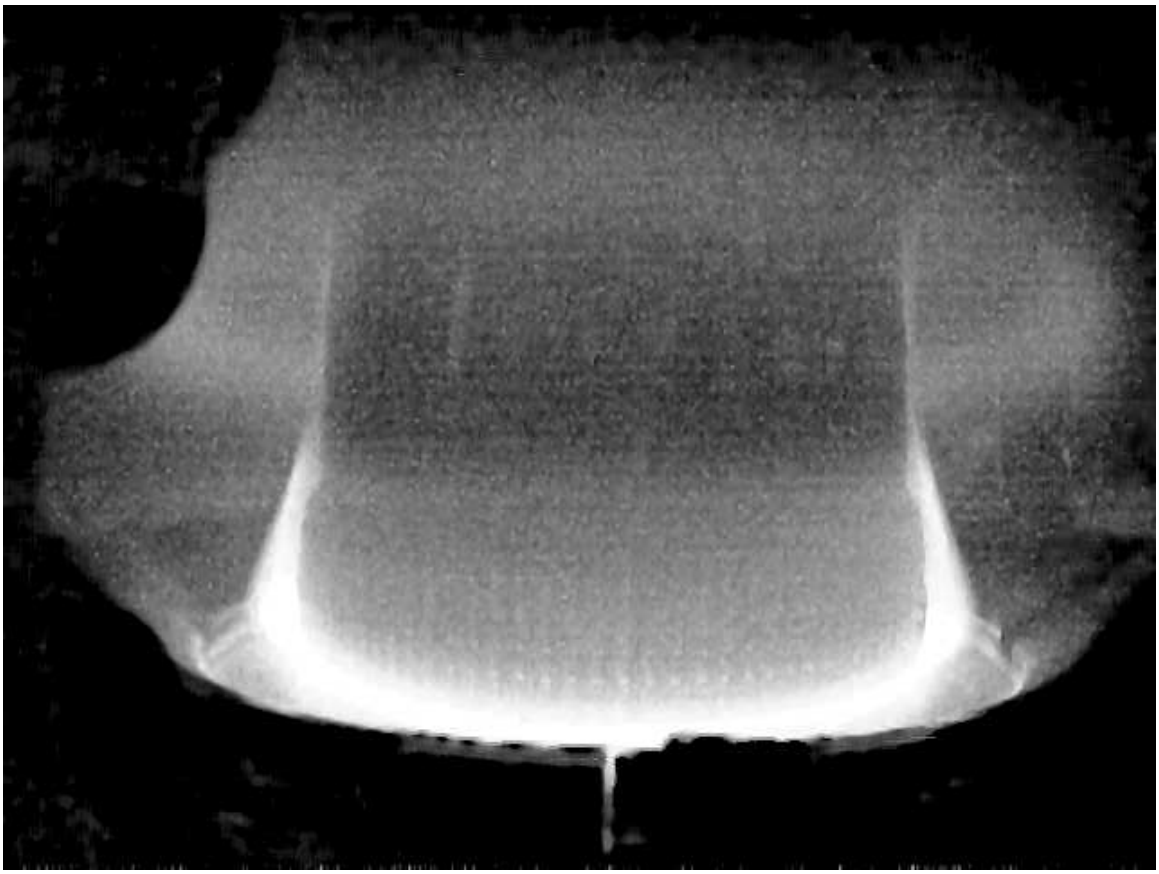

Figure 7-1: A wide angle view of an ITB in C-Mod. The faint ring of more intense light emission, towards the top of the photo, is the region of the ITB. This view is from below the midplane. (Photo graciously provided by Dr. Chris Boswell.)

7.1 ICRF Generated Internal Transport Barriers

7.1.1 ICRF ITB Rotation Data

Figure 7-2 are some density profiles at various times during an ITB discharge. During the ITB the density peaks up by a factor of two or more as compared to the non–ITB H–mode level. The point where the density drastically changes slope ($r/a \sim 0.5$, $R = 0.785\ m$ in this case) is called "the foot" of the barrier.

During the L–mode portion of the discharge the rotation is flat and near zero in magnitude. As the plasma makes the L $\rightarrow$ H transition, it starts to rotate in the co–current direction. Figure 7-3 shows the time histories of the measured rotation.

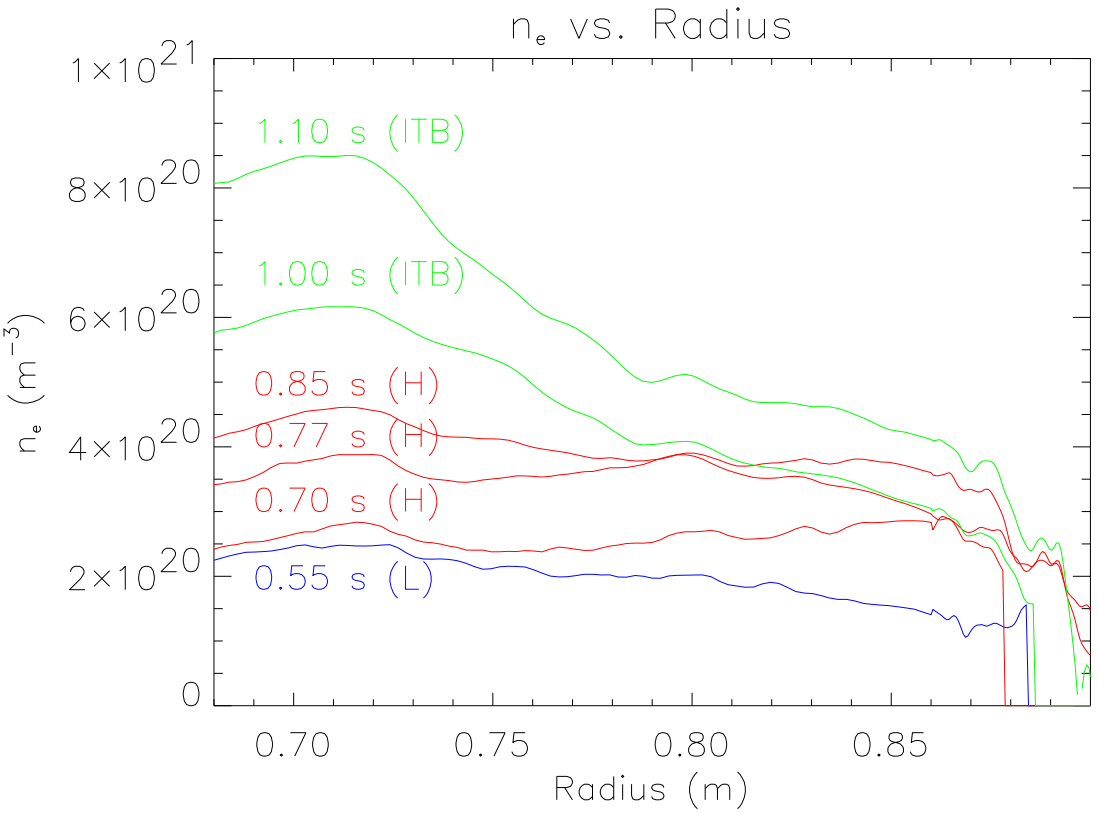

Figure 7-2: Density profiles during an ITB discharge. At 0.55 s (blue profile) the plasma is still in L–mode, the density is flat and the edge pedestal has not yet formed. At 0.68 s the ICRF heating turns on, and the plasma goes into H–mode, (red profiles) the edge pedestal has formed, but the core density is flat and relatively low. At about 0.87 s the ITB forms and the density starts to peak. By 1.10 s the core density is a about a factor of two over the H–mode level, and a factor of four over the L–mode level.

Again, the rotation starts at the outside edge of the plasma, and moves in as the plasma spins up to its H–mode value. Shortly after the H–mode fully develops ($\sim$ 0.87 s) the plasma enters the ITB portion of the discharge. At one second into the discharge the barrier has formed, the density is peaking up (Fig. 7-2), and the toroidal rotation has started to drop (Fig. 7-3).

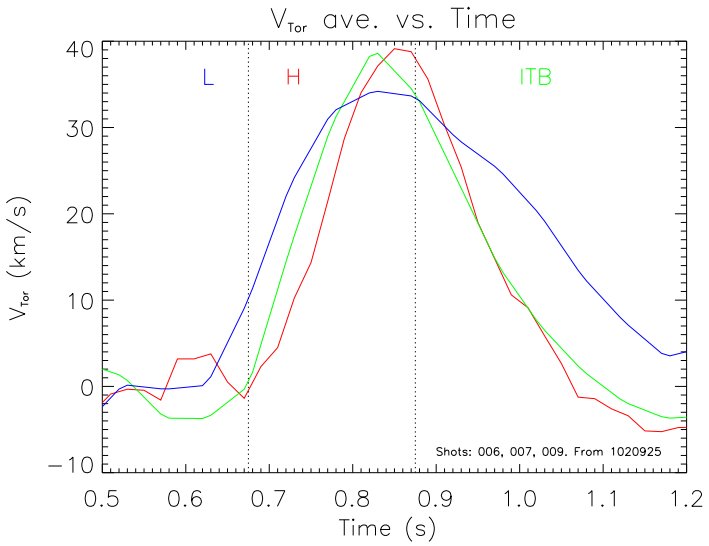

Figure 7-3: Toroidal Rotation time histories for the three spectrometers throughout the evolution of the discharge. V_{Tor} in km/s is on the ordinate, and time in seconds in on the abscissa. The core view ($r/a = 0.0$) is plotted in red. The middle view ($r/a = 0.3$) is plotted in green. The outermost view ($r/a = 0.6$) is plotted in blue. (These data have been smoothed in time using "nearest neighbor" smoothing.)

Figure 7-3 has some interesting features. First, the rise in the rotation from the L–mode to the H–mode phase exhibits the same shape and clear momentum diffusion as seen in flat ICRF EDA H–modes. One of the requirements for most ITBs on C–Mod is to first establish an EDA H–mode. Second, after the H–mode is fully developed, the profile is flat; again this is an EDA H–mode, a flat profile is usually seen. Once the barrier forms; the rotation starts to drop on the channels inside the barrier, quite quickly. However, the rotation outside the barrier, although also slowing down, falls off much more slowly.

Figure 7-4 shows the rotation profiles during the evolution of the H–mode, and

then later during the formation of the ITB. This is the same information as in Fig. 7-3 displayed vs. radius, to show the lag in the toroidal rotation rise times. The data plotted in this figure (7-4) confirm previous results, (see §3.1, specifically Fig. 3-3) plus add a new measurement point outside the foot of the barrier.

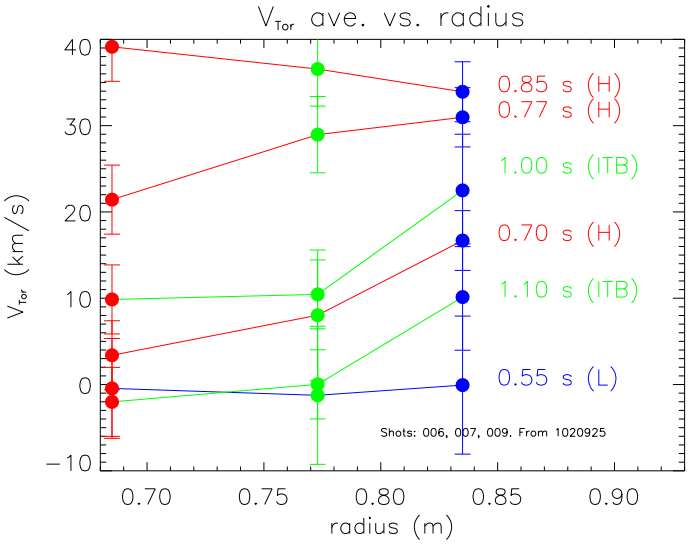

Figure 7-4: Rotation profiles for various time slices through out the evolution of the discharge. V_{Tor} in km/s is on the ordinate, and major radius in meters in on the abscissa. The first time slice is during the L–mode, (shown with a blue line, and label). The second three time slices are during the H–mode rise in rotation (shown with a red lines, and labels). The final two time slices are during the ITB phase of the discharge (shown with green lines and labels). The foot of the density barrier is at $R \simeq 0.785\ m$, just out from the F–port spectrometer, (green circles). This is the same information as in Fig. 7-3. These time slices correspond to those in Fig. 7-2.

The plasma rotation profile starts out flat, perhaps slightly negative. When the ICRF heating is turned on the plasma goes into H–mode, as seen at 0.68 sec, on the D_α trace in Fig. 7-5. At this point the plasma starts to rotate in the co–current direction, with the rotation starting at the edge, and propagating inward. At about 0.87 s the ITB forms, and the rotation inside the barrier can be seen to drop. The rotation outside of the barrier seems also to decrease in magnitude, but it seems to drop at a slower rate.

Figure 7-6 is the Ar's momentum density from the same shot as Figs. 7-2 – 7-5.

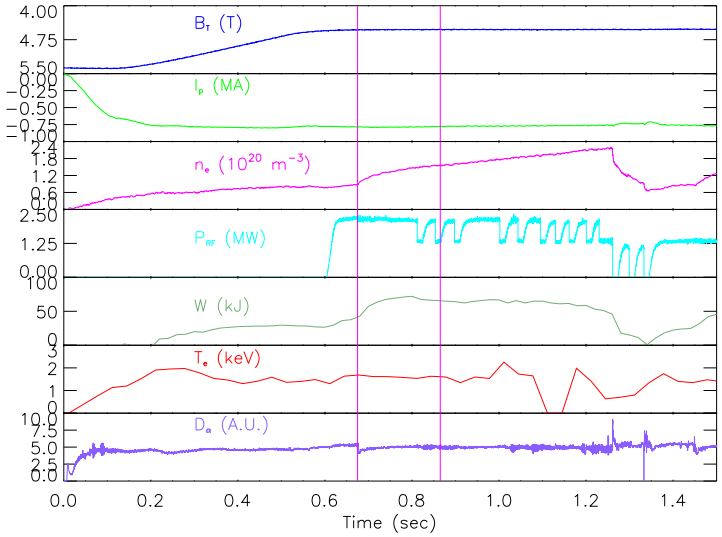

Figure 7-5: Time histories of some plasma parameters. From top to bottom: the magnetic field, the plasma current, the plasma density, the RF power, the plasma temperature, and the D_α emission. The first vertical line shows the time of the L $\rightarrow$ H transition. The second vertical line shows the time the density starts to peak, and the ITB forms.

The diffusion of momentum into the plasma during the L $\rightarrow$ H transition can clearly be seen. When the barrier forms, the momentum is pushed out of the core of the plasma, by some outward convection mechanism. This figure has been included because all the quantities that go into the calculation are known, the rotation velocity, the Ar density from the brightness, and the mass of Ar. Argon transport is totally governed by the deuterium transport because the two are strongly collisionally coupled. A more interesting quantity is the deuterium momentum density.

By combining Eqs. 2.1 and 2.2, and a correction term for the $E_\parallel$ contribution from Catto *et. al.* [118], an equation for the bulk deuterium toroidal rotation velocity, (V_ϕ^i,) can be found, depending on the Ar rotation velocity (V_ϕ^I), the temperature gradient ($\frac{\partial}{\partial r}T_i$), the poloidal magnetic field (B_θ), the coefficient K_2, the total magnetic field (B), the ion–ion collision frequency (ν_{ii}), the parallel electric field ($E_\parallel = V_\ell/2\pi R$) and the ion charge ($Z_i$), in the form:

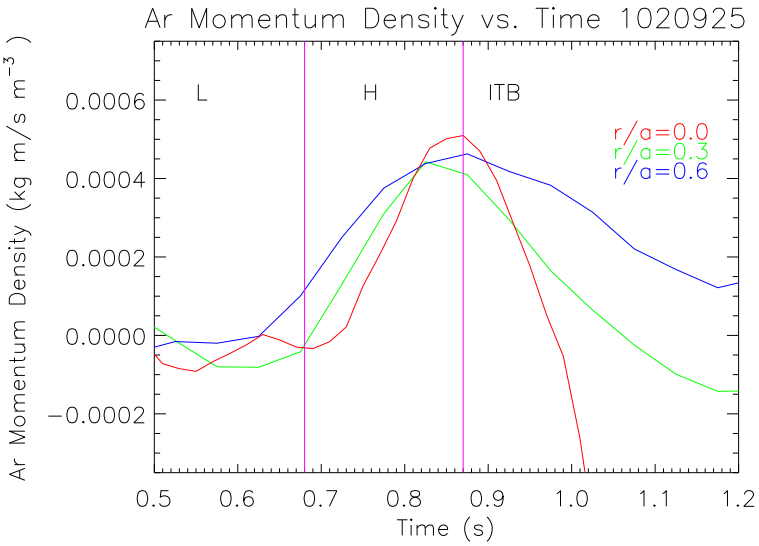

Figure 7-6: Ar momentum density vs. time for the shot in Figs. 7-2 – 7-5. The red trace is the core spectrometer ($r/a \simeq 0.0$), the green trace is the middle spectrometer ($r/a \simeq 0.3$) and the blue trace is the outermost spectrometer ($r/a \simeq 0.6$). For this plot the Ar density and ion mass have been folded together with the rotation data to give the momentum density. After the L $\rightarrow$ H transition the error is 15% or less.

$$V_\phi^i = V_\phi^I + \frac{3K_2}{2eB_\theta}\frac{\partial}{\partial r}T_i + \frac{Z_i eB\langle BE_\parallel\rangle}{m_i\nu_{ii}\langle B^2\rangle}C_Q \tag{7.1}$$

where C_Q is the constant that arises from the inclusion of trapped particle effects, ($C_Q|_{0.0} \simeq 9.115$, $C_Q|_{0.3} \simeq 3.150$ and $C_Q|_{0.6} \simeq 2.239$.)[2] The dominant term in this calculation is the impurity rotation velocity V_ϕ^I. The temperature gradient term is generally negative, but can change sign, (here $K_2 \sim 1$.) In this discharge the impurity rotation velocity is about 40 km/s, the temperature gradient term is of order $-$ 10 km/s and the $E_\parallel$ term is of order 1 km/s.

On the axis the temperature gradient term becomes indeterminate, ($\frac{3K_2}{2e} \cdot \frac{0}{0}$.) To deal with this we assume $T_i \simeq T_{i0}\exp(-r^2/\lambda_{Ti}^2)$, which implies $\frac{\partial}{\partial r}T_i \simeq -2r/\lambda_{Ti} \cdot T_i$. The poloidal field can be stated as $2\pi r B_\theta = \mu_0 \int J_\phi \cdot dA$, which implies $B_\theta = \mu_0 J_{\phi 0} r/2$,

[2]Here $C_Q \equiv (1+L)I\left[\frac{1}{\langle\langle Q\rangle\rangle} + (1-I)\left\langle\left\langle\frac{1}{Q}\right\rangle\right\rangle\right]$, $I \simeq 1 - 1.46\epsilon^{1/2}$, $L(I,Z) = \frac{0.68(Z-0.38)I}{Z^2-(0.55Z-0.18)I}$, $\langle\langle Q\rangle\rangle = 0.4$ $\langle\langle Q^{-1}\rangle\rangle = 5.4$,[118].

$\mu_0 J_{\phi 0} = 2B_0/q_0 R_0$. Assuming $\lambda_{Ti} \sim 0.06\ m$:

$$\frac{3K_2}{2eB_\theta}\frac{\partial}{\partial r}T_i\bigg|_{0.0} \simeq \frac{3K_2 q_0 R_0 T_i}{eB_0\lambda_i} \simeq 6\ (km/s)$$

Figure 7-7 is the D's momentum density calculated in this manner, for the shot in this chapter.

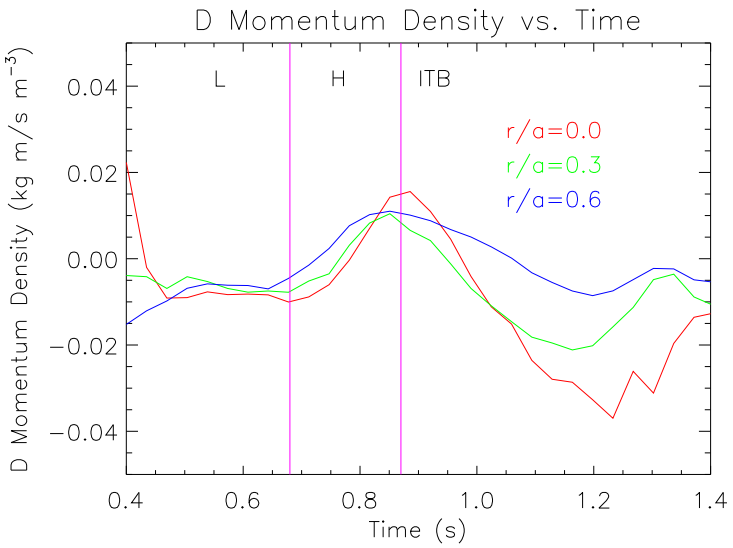

Figure 7-7: Deuterium momentum density vs. time for the shot in this chapter. The red trace is in the core about $r/a \simeq 0.0$, the green trace at $r/a \simeq 0.3$ and the blue trace at $r/a \simeq 0.6$. For this plot the density and ion mass have been folded together with the rotation data to give the momentum density. After the L $\rightarrow$ H transition the error is 10% or less.

These data were taken from spectra added from three shots (006, 007 and 009) during this run ($1020925xxx$). Figure 7-8 plots the D_α brightness trace for these three shots. The sudden drop is indicative of the L $\rightarrow$ H transition into EDA H–mode, and is thus used as the time of transition. Transition times for the three shots, their average, their deviation from the average and the standard deviation have all been calculated and are listed in Table 7.1.

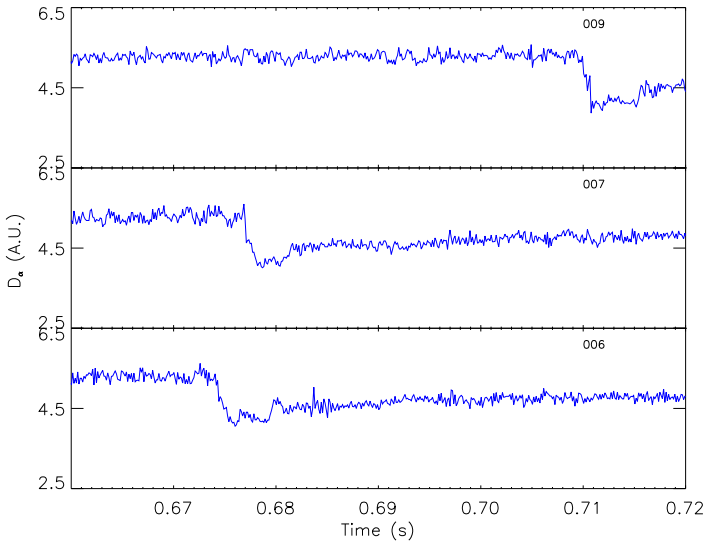

Figure 7-8: Time histories of the D_α emission during the L $\rightarrow$ H transition for each of the shots used in the analysis.

Shot	t_{L-H} (s)	$\Delta\, t_{L-H} = \bar{t}_{L-H} - t_{L-H}$
006	0.7087	-0.0216
007	0.6727	0.0135
009	0.6772	0.0090
$\bar{t}_{L-H}$	0.6862	0.0
$\sigma_{t_{L-H}}$	0.0196	–

Table 7.1: For run 1020925: the shots involved and their associated L $\rightarrow$ H transition times have been tabulated. A mean time of transition and a standard deviation in the times of transition have been included. The standard deviation of the L $\rightarrow$ H times is less than half the integration time of the data acquisition, so we may add together the spectra from these shots with confidence.

7.1.2 Inferred Radial Electric Field

Fig. 7-9 is a plot of the individual terms from Eq. 2.16. Again, the terms 1, 2 and 3 have been thus been set, identically, to zero at $r/a = 0$, and these are not measured quantities. It can be seen that the dominant term is Term 1, $(V_\phi^I B_\theta.)$ Term 2, $(-\frac{(K_1+\frac{3}{2}K_2-1)}{e}\frac{\partial}{\partial r}T_i,)$ has the least effect. Term 3, $(\frac{T_i}{en_i}\frac{\partial}{\partial r}n_i)$, is of the same order as Term 1.

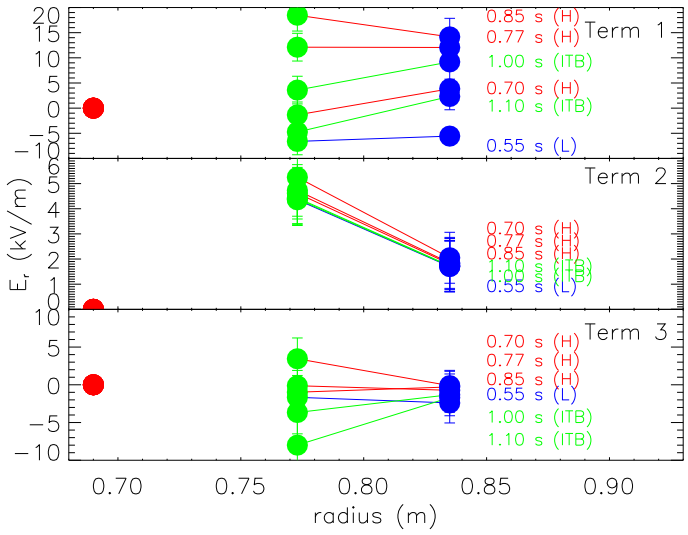

Figure 7-9: The profiles of the three terms that make up the calculation of the inferred radial electric field. Term 1 $\equiv V_\phi^I B_\theta$, Term 2 $\equiv -\frac{(K_1+\frac{3}{2}K_2-1)}{e}\frac{\partial}{\partial r}T_i$ and Term 3 $\equiv \frac{T_i}{en_i}\frac{\partial}{\partial r}n_i$. Each term has been plotted vs. radius at the same six time slices as in Figs. 7-2 and 7-4.

The remaining quantities in Eq. 2.16 are measured during normal plasma operation. Figure 7-10 shows time histories of the radial electric field at the outer two spectrometer view locations, the central view has been set to zero. Figure 7-11 shows the same information in profile form.

During the ITB the radial electric field becomes highly sheared. (These data are consistent with the radial electric field profiles found in DIII-D[79, 85].) The inferred $E_r(r)$ in Fig. 7-11 puts a lower limit on the steepness of the profile during the ITB. One can easily imagine that if a more detailed profile were taken, the points right

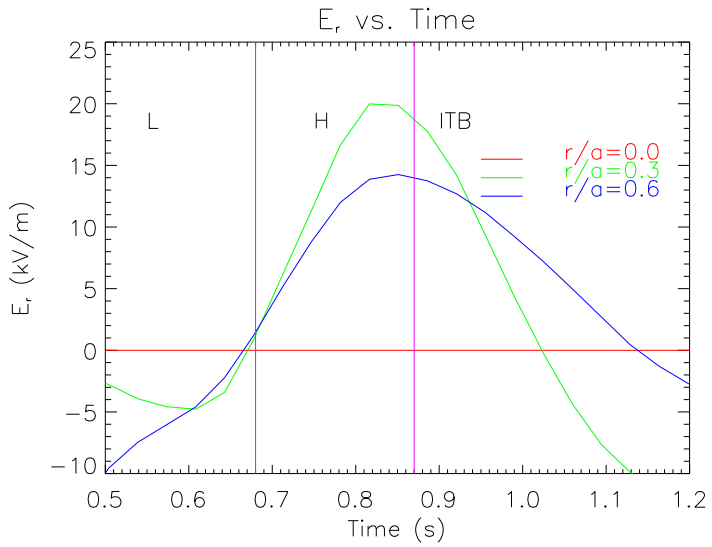

Figure 7-10: Time histories of the inferred radial electric field at the view locations of the three spectrometers.

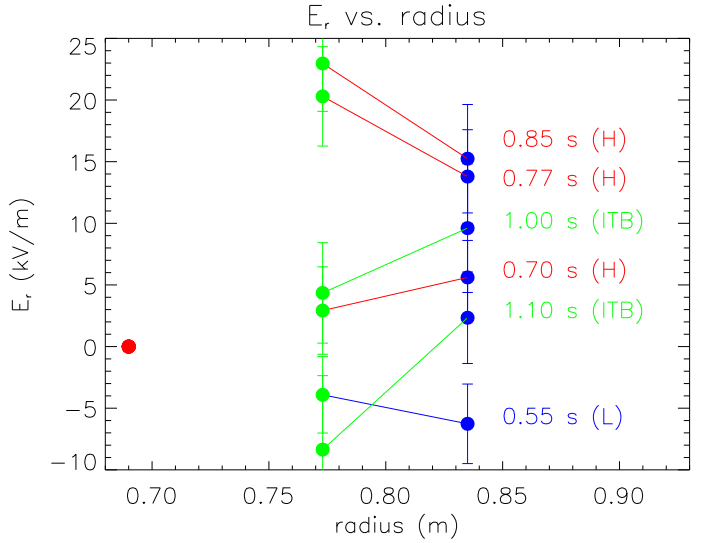

Figure 7-11: Profiles of the radial electric field at various times during the discharge. Note: these profiles are taken at the same time slices as both the density profiles (Fig. 7-2) and the rotation profiles (Fig. 7-4, they are the sum of the terms in Fig. 7-9).

up to the location of the barrier foot on either side would have drastically differing values. The E_r shear could then be very high. Based on the measured rotation velocity profile and the electric field profile that is inferred, a statement that the E_r shear is greater than or equal to about 183 kV/m^2 ($\partial/\partial r\ E_r \geq 183\ kV/m^2$) can be made.

A very simple calculation of the minimum ω_E at the foot of the barrier can be made from Eq. 2.47[3]:

$$\omega_E = \frac{RB_\theta}{B}\frac{d}{dr}\left(\frac{E_r}{RB_\theta}\right). \tag{2.47}$$

Averaged parameters from the shots, at the locations in question, at $t = 1.1\ s$, are: $B_\theta|_{0.6} = 0.6$ T, $B_\theta|_{0.5} = 0.63$ T, $B_\theta|_{0.3} = 0.7$ T, $E_r|_{0.6} = 3$ kV/m, $E_r|_{0.3} = -\ 8$ kV/m, $R|_{0.6} = 0.83\ m$, $R|_{0.5} = 0.81\ m$, $R|_{0.3} = 0.77\ m$ and $B|_{0.5} = 3.8$ T. The B_θ values come from EFIT Equilibrium analysis code[101–104]. It is found:

$$\omega_E \geq \left.\frac{RB_\theta}{B}\right|_{0.5}\left(\frac{\left.\frac{E_r}{(RB_\theta)}\right|_{0.6} - \left.\frac{E_r}{(RB_\theta)}\right|_{0.3}}{R|_{0.6} - R|_{0.3}}\right) \sim 3.8 \times 10^4 rad/s.$$

Note: this is a "back of an envelope" calculation based on two points, inferred E_r profiles, and a linear slope derivative.

This shearing rate (ω_E) can now be compared with the growth rate for some form of turbulence. In this plasma after the barrier has formed the best comparison could be made with the growth rate for trapped electron modes (TEM), γ_{TEM} a reasonable estimate for this growth rate is $1.5 \times 10^5\ rad/s$ [119, 120].

The ω_E calculated above is about a factor of 4 low to suppress the growth of TEM mode instabilities. If the shear layer is thinner than the $\sim 6\ cm$ gap between the view chords, this could still be enough to suppress TEM mode turbulence. It is important to remember that this measurement does not have the resolution to make a definitive statement about anything except the *minimum* shearing frequency. It is certainly

[3]The factor k_θ / k_r is generally ~ 1, thus it is neglected here.

possible, that the shearing layer is significantly thinner than the $\sim 6\ cm$ gap between the view chords of the spectrometers. A similar calculation at time $t = 1.0\ s$ yields $\omega_E \simeq 1.8 \times 10^4\ rad/s$.

7.2 Error Analysis

7.2.1 Measurement Error

Analysis of rotation measurement error in the ITB case is propagated in the same manner as in the Ohmic case, §5.5.

For the case of momentum density the error in the density has been folded in, propagating error with the relation:

$$\sigma_{mnV} = m\sqrt{(n\sigma_{V_{Tor}})^2 + (\sigma_n V_{Tor})^2 + 2nV_{Tor}\sigma^2_{nV_{Tor}}} \simeq m\sqrt{(n\sigma_{V_{Tor}})^2 + (V_{Tor}\sigma_n)^2} \tag{7.2}$$

The covariance term has been dropped. The correlation between the density and the toroidal rotation velocity is low therefore on average the positive deviations will cancel the negative deviations, and the net contribution will be about zero.

The analysis of error for the radial electric field was done in the same manner as in §5.5.1 of Chapter 5.

7.3 Chapter Summary

Internal transport barriers are regions of improved confinement in the plasma core, generally, although not exclusively, formed from H–mode plasmas. During ITBs on C–Mod the density is seen to peak up over the standard H–mode value in the central region of the plasma, and the toroidal rotation is seen to drop.

During ICRF heated ITBs the plasma is seen to stop rotating, first in the core, and later out by the edge. The measured momentum density profile shape implies that there is a outward momentum convection during the ITB portion of a discharge.

Based on the measured rotation profiles and the plasma parameters taken from other diagnostic measurements, the radial electric field was calculated. This calculation reveals a lower limit on the steepness of the shear in the radial electric field, not less than 183 $k\mathrm{V}/m^2$, or a shearing frequency, $\omega_E \geq 3.8 \times 10^4\ rad/s$.

Chapter 8

Conclusions and Future Work

The final chapter of this thesis will summarize the work presented here, and offer some suggestions for future directions that might further this experimental study, and recapitulate the theoretical explanation of the data presented here.

8.1 Summary

This section is a brief summary of the results presented in this thesis. Measurements of toroidal rotation profiles in a source free tokamak have been made. The absence of neutral beams and the associated uncertainty they introduce to rotation measurements makes C–Mod the perfect tokamak for performing momentum transport experiments.

8.1.1 Background

Chapters 2 – 4 detail much of the background required for the experimental study in this thesis.

Chapter 2 sketched out most of the present theories pertaining to toroidal rotation in tokamak plasmas[14–48]. Neoclassical theory has been covered in the most detail because it was used for many of the calculations in later chapters. Other theories were touched upon, including revisited neoclassical theory and subneoclassical theory.

Time scales from these theories were compared to data in later chapters. Some theories of ICRF rotation were discussed, including Perkins' theory, Chang's RF drive theory and Hellsten's theory. Two theories of spontaneous rotation were discussed. Finally, some of the theory of ITBs was mentioned.

Chapter 3 reviewed most of the previous toroidal rotation measurements on Alcator and other tokamaks[17, 24, 51–73, 80–83, 86–92]. Most other measurements have been made using neutral beam injection, and have thus greatly perturbed the plasma's momentum.

Chapter 4 outlined the basic layout of the spectrometer array that was used to make these measurements. This chapter went through the basic physics of the measurement and detailed the hardware of the experimental setup. This chapter also linked into all of the appendices: atomic physics concerns were discussed in appendices A – C, and the attenuation of x–rays in both air and Be was discussed in appendix D.

8.1.2 Ohmic Discharges

Chapter 5 presented data taken during Ohmic discharges. During the most basic Ohmic L–modes the rotation data are found to yield a flat profile rotating slightly counter current ($\sim 8\ km/s$). Data taken during a density scan showed that the rotation velocity of the impurity ions followed the scaling $V_{tor} \propto 1/n_i$. It was consistent with the bulk ion velocity being zero and the impurity velocity relative to the bulk being neoclassical. Data taken during Ohmic H–modes were found to have flat rotation profiles in the co–current direction, with velocities of about $\sim 35\ km/s$. The rotation has been observed propagating in from the outer regions of the plasma to the core. These data were fitted using a simple diffusion model and the diffusion coefficient (D_{V_ϕ}) and the diffusion time scale (τ_{V_ϕ}) were calculated, based on this model. During the H–mode phase, the diffusion coefficient (D_H) was found to be $\sim 0.100\ m^2/s$ with a corresponding confinement time (τ_H) of about $0.076\ s$. After the H–mode to L–mode transition the diffusion coefficient (D_L) was found to be $\sim 0.250\ m^2/s$ with a corresponding confinement time (τ_L) of about $0.030\ s$. Values for τ_ϕ, τ_E and τ_{imp} can

be found tabulated in Table 8.1. It was concluded that transport is anomalous, with diffusivities about a factor of 50 over the expected neoclassical value. Finally, a link between magnetic geometry and toroidal rotation in Ohmic L–modes was presented.

8.1.3 ICRF Heated Discharges

Chapter 6 presented data taken during ICRF heated discharges. This chapter focused on two general profile shapes that had been seen during ICRF heated plasmas.

Flat rotation profiles were fit to a simple diffusion model. The agreement was quite good. The fit was made matching the terminal rotation velocity during ICRF H–mode and using the diffusion coefficient (D) as a free parameter, found to be $D \sim 0.100\ m^2/s$. Once the diffusion coefficient was set the momentum confinement time (τ) was determined, ($\tau \sim 0.076\ s$). The confinement times for various discharges were all found to be quite similar to that of the Ohmic H–mode case.

Peaked rotation profiles were also measured. These profiles were fitted using a slightly more complicated model that included both diffusion and convection. In this case the terminal rotation velocity was again matched, ($P = 63\ km/s$), and the diffusion coefficient and the convection velocity were taken to be free parameters, and were found to be $v_c \simeq 12\ m/s$ and $D_H \simeq 0.400\ m^2/s$. When the plasma goes back to L–mode the simple diffusion model solution is used again with $D_L \simeq 0.250\ m^2/s$. Again, the momentum confinement times were calculated and found to be similar to the simple diffusion case, ($\tau_H \sim 0.070$.) The rotation profile data taken during ELM–free discharges qualitatively agrees with the shape of rotation profiles from DIII-D, (§3.4.1,) despite the huge momentum input on DIII-D.

These values for L–mode, Ohmic EDA, ICRF EDA and ELM–free H–modes have been summarized in Table 8.1.

In all cases the results presented here are consistent to within a factor of 2 – 4 with those previously found, (see Chapter 3).

Shot Type	$D\ (m^2/s)$	$v_c\ (m/s)$	$\tau_\phi\ (s)$	$\tau_E\ (s)$	$\tau_{imp}\ (s)$
L–Mode	0.250	0.0	0.030	0.025	0.020
H–Mode (Ohmic)	0.100	0.0	0.076	~ 0.060	0.050
L–Mode (Ohmic)	0.250	0.0	0.030	0.033	0.020
EDA (ICRF)	0.050 – 0.100	0.0	0.152 – 0.076	0.036	0.050 – 0.200
L–Mode	0.200	0.0	0.038	0.025	0.020
ELM–Free (ICRF)	0.400	12	0.070	0.029	> 0.015
L–Mode	0.250	0.0	0.030	0.020	0.020

Table 8.1: Momentum confinement times for the simple models fit to data presented in Chapter 5 and 6.

8.1.4 ITB Discharges

Chapter 7 presented experimental data taken during ITB discharges. At the onset of the ITB phase of the discharge, the toroidal rotation was observed to decrease in magnitude and, if the ITB lasted long enough, reverse direction. Momentum diffusion time scales were again observed in the flat rotation profiles that proceeded the ITBs.

Calculations of the the radial electric field that would be required to generate the observed rotation were presented, as calculated from neoclassical theory. This electric field was used in a very basic estimation of the shearing frequency, (ω_E). The calculation revealed $\omega_E \geq 3.8 \times 10^4\ rad/s$.

8.2 Future Work

This thesis has by no means exhaustively investigated toroidal rotation profile measurements on Alcator C–Mod. In fact it has opened doors to many interesting topics that could be studied further.

8.2.1 DNB Comparison

A natural first setup beyond this thesis would be to compare the x–ray rotation measurements with some of the data from the CXRS system on C–Mod. Due to the high densities in C–Mod the CXRS system is only capable of measuring in to about

$r/a \simeq 0.5$, the present views of the spectrometer array view out to $r/a \simeq 0.6$. This region of overlap would allow for comparison of the data from the two diagnostics. The data sets from both the CXRS and the tangential x–ray array put together would allow for a much more complete profile measurement, perhaps better elucidating the physics mechanisms driving plasma rotation.

8.2.2 Additional Views

Additional tangential views close to the ITB foot on either side would help to reveal the true physics here. The existing three points, although a terrific start to this investigation, are limited in that they leave a large portion of the plasma as yet unmeasured.

At this point it seems that non–beam based spectroscopy is the only way to probe the core of the plasma due to the high density of C–Mod and the limited penetration depth of the DNB. If a more detailed study of toroidal rotation is to take place, some other spectroscopic means will need to be employed, or more space will need to be liberated for x–ray spectroscopic use.

The primary impediment to more tangential x–ray spectrometers at this point is simply space on the tokamak. A great deal of work was required to alter the torsion cylinder in order to accommodate the two new views that are the subject of this thesis. It is doubtful that more space could be made available, but it certainly would be helpful.

8.2.3 Ohmic ITBs

Although not discussed in this thesis there are data during Ohmic ITBs. A key to figuring out the ITB may very well lie in the Ohmic ITB. Ohmic ITBs are generated from Ohmic EDA plasmas. ITBs exhibit a very tight threshold for formation[17]. An ITB is generally formed with off axis ICRH, and it is believed that this power somehow induces the region of improved transport. But how does this relate to the Ohmic ITBs, with no ICRF at all? Relating the Ohmic power deposition profile to

the ICRH power deposition profile might give a hint as to the driving mechanism for the ITB. X–ray rotation measurements made during both ICRF and Ohmic ITBs will allow a measurement for comparison.

8.2.4 Detailed Theory

This diagnostic has collected a tremendous amount of data, (almost every shot of every day since its inception). These data have all been looked at very tersely in the process of generating rotation velocities out of the raw spectra. Much of the significant and indicative data have been included here. There is still, however, a great deal to be analyzed in detail, and these data, in conjunction with the simple models presented here, could lead to a very detailed theory of plasma rotation.

A theory that either quantifies or disproves the link between ICRF resonance location and rotation profile peak and magnitude presumably could be established using data already gathered in conjunction with some more data and RF modeling.

Rotation could be the key to linking Ohmic and ICRF heated ITBs. Presently, they seem to exhibit the same behavior, but no theory has yet been proposed to explain why on one hand ICRF is required yet in a different situation the (apparently) same result can be achieved in an Ohmic plasma.

These analyses could lead to new theories of rotation, momentum, and their behavior in a source free tokamak. There are at least three interesting regimes to be considered, Ohmic discharges, ICRF heated discharges and ITB discharges. The existing data quite possibly hold the key to some of the more interesting tokamak operating regimes.

Appendix A

Expected Line Intensities for He–Like Ar

This Appendix will go through the calculations for the expected line intensities of He–like Ar. Much of this appendix was taken from [12, 121, 122].

A.1 Line Intensities

The expected intensity for a given line emitted from a plasma will depend on the density of that charge state, the density of electrons, population density of the upper level, the branching ratio, the area of view (more properly the étendue: the product of the observation area and the solid angle) and the line of sight through the plasma. The density of the ion, (in this case some charge state of Ar calculated in appendix C,) depends on the temperature, which in turn depends on the radius in the plasma.

The line intensity (F_{ik}) will be the integral over the line of sight (dl) of the emissivity of the particular line (j_{ik}), where $i \rightarrow k$ is the transition producing said line.

$$F_{ik} = \int_l j_{ik} dl \tag{A.1}$$

The emissivity of a line transition from state i to state k ($i \rightarrow k$) is given by:

$$j_{ik} = n_e n_i A_{ik} \tag{A.2}$$

There are predominately in four lines of He–like Ar of interest in this thesis. The resonance line (**w**), the forbidden line (**z**), and two intercombination lines (**x** and **y**). The wavelengths and transitions of these four lines can be found in Table A.1

line	Transition	λ_0 (mÅ)	
w	1s2p $^1P_1 \rightarrow$ 1s^2 $^1S_0$	3949.2	resonance line
x	1s2p $^3P_2 \rightarrow$ 1s^2 $^1S_0$	3966.0	intercombination line
y	1s2p $^3P_1 \rightarrow$ 1s^2 $^1S_0$	3969.4	intercombination line
z	1s2s $^3S_1 \rightarrow$ 1s^2 $^1S_0$	3994.3	forbidden line

Table A.1: The transitions of interest for He–like Ar, in these measurements.

To calculate the expected line intensity, or count rate of the individual lines, the population processes and mechanisms that drive transitions from the lower levels to the higher levels must be understood. For each level being considered, an equation of the form:

$$\frac{1}{n_e}\frac{dn_k}{dt} = \sum n_l S_l - n_k \sum (S_k + \alpha_k) + \sum n_j \alpha_j. \tag{A.3}$$

describes the time dependent population, (density, n_k, n_l or n_j), of that level. S_i are the ionization coefficients and α_i are the recombination coefficients, for the state (i = k, l or j), where: k is the state in question, j is any state with higher energy than k and l is any state with lower energy than k. If the population processes are in a steady state ionization equilibrium Eq. A.3 reduces to:

$$n_k(S_k + \alpha_k) = \sum n_l S_l + \sum n_j \alpha_j \tag{A.4}$$

$$\Rightarrow n_k = \frac{\sum n_l S_l + \sum n_j \alpha_j}{(S_k + \alpha_k)}. \tag{A.5}$$

This is simply a particle balance, the left hand side represents everything leaving the state k and the right hand side represents everthing coming into the state k.

When all the population and depopulation processes have been taken into account, the densities of the upper levels that produce the four lines under consideration here, (**w**, **x**, **y** and **z**) can be stated in the form of Eq. A.5 as[12]:

$$n_w = \frac{(n_H n_e \alpha'_{c1'} + n_{He} n_e S'_{gm'} + n_{Li} n_e S'_{g'm'}) S_{m'1'} + (n_{He} S'_{g1'} + n_H \alpha'_{c1'})(A_{m'g} + n_e S_{m'1'})}{A_{m'g}(A_{1'g} + A_{1'm'}) + n_e (S_{1'm'} A_{m'g} + S_{m'1'} A_{1'g})} n_e \tag{A.6}$$

$$n_x = \frac{n_z S_{m2} + n_H \alpha'_{m2} + n_{He} S'_{g2}}{A_{2g} + A_{2m} + n_e S_{2m}} n_e \tag{A.7}$$

$$n_y = \frac{n_z S_{m1} + n_H \alpha'_{m1} + n_{He} S'_{g1}}{A_{1g} + A_{1m} + n_e S_{1m}} n_e \tag{A.8}$$

$$n_z = n_e \left(n_{He}(S'_{gm} + \sum_{k=0}^{2} S'_{gk}) + n_H(\alpha'_{cm} + \sum_{k=0}^{2} \alpha'_{ck}) + n_{Li} S_{g'm} - \frac{n_H \alpha'_{c1} + n_{He} S'_{g1}}{A_{1g} + A_{1m} + n_e S_{1m}} A_{1g} \right.$$
$$\left. - \frac{n_H \alpha'_{c2} + n_{He} S'_{g2}}{A_{2g} + A_{2m} + n_e S_{2m}} A_{2g} \right) \left(A_{mg} + \frac{n_e S_{m1}}{A_{1g} + A_{1m} + n_e S_{1m}} A_{1g} + \frac{n_e S_{m2}}{A_{2g} + A_{2m} + n_e S_{2m}} A_{2g} \right)^{-1} \tag{A.9}$$

Here A_{ij} are the radiative transition probabilities (given in Table B.3, of Appendix B), α'_{ij} is the sum of the recombination rates, both radiative and dielectronic, and S_{ij} are the rate coefficients for collisional excitation. The indicies of the transitions, g, g', 1, m, *etc.*, can be found listed in Table A.2[1]. A full description of the calculation of these quantities can be found in Appendix B. n_H, n_{He} and n_{Li} represent the densities of H–like, He–like and Li–like argon, respectively. In Appendix C, these densities are calculated as fractional abundances of the total argon density assuming coronal equilibrium.

Figure A-1 is a plot of the expected emissivity profiles for the four He–like Ar lines (**w**, **x**, **y** and **z**).

[1]A diagram of the energy levels has been included as Fig. B-1, in Appendix B, where these processes will be discussed in more detail.

Index Symbol	Spectroscopic Notation	
g	$1s^2\ {}^1S_0$	He – like Ground Level
g'	$1s^2 2s\ {}^2S_{\frac{1}{2}}$	Li – like Ground Level
c	continuum	All Levels $n > 2$, *i.e.* H – like
0	$1s2p\ {}^3P_0$	
1	$1s2p\ {}^3P_1$	**y** Intercombination Line†
2	$1s2p\ {}^3P_2$	**x** Intercombination Line†
$1'$	$1s2p\ {}^1P_1$	**w** Resonance Line†
m	$1s2s\ {}^3S_1$	**z** Forbidden Line†
m'	$1s2s\ {}^1S_0$	

Table A.2: Index notation for the $n = 2$ levels of He-like Ar ions. †: Implies the line comes from the transition from this level to the ground level, *e.g.* the transition $1' \rightarrow g$, would be **w**, the resonance line.

Figures A-2 and A-3 are plots of an expected He–like Ar spectrum, from the emissivities of the individual lines, integrated over the line of sight of a tangential views of the F–port ($r/a \simeq 0.3$) and K–port ($r/a \simeq 0.6$) spectrometers, respectively. The line shape was assumed to be Gaussian. It has also been assumed that the argon is in thermal equilibrium with the plasma, and thus the line width is related to the Ar ion temperature.

These spectra show the importance of recombination to the line intensities. At $r/a = 0.6$ (Fig. A-2) the forbidden line (**z**) is more intense than the resonance line (**w**), whereas at $r/a = 0.3$ (Fig. A-3) the resonance line (**w**) is the more intense of the two. Essentially population mechanisms of the upper states of the transitions are temperature dependent. Thus, in the regions where the temperature is lower, ($r/a = 0.6$ vs. $r/a = 0.3$) the **z** is relatively more intense, because recombination is the dominant population mechanism for this line. In regions where the temperature is higher, ($r/a = 0.3$ vs. $r/a = 0.6$) the **w** is more intense.

Fig. A-4 is the model prediction of a He – like Ar spectrum on axis, ($r/a = 0.0$). This simulated spectrum can also be compared with the spectrum in Fig. 4-3, a He – like Ar spectrum taken on axis. Excluding the effects of the satellites that were ignored in this model, good agreement is found between this model and the measured

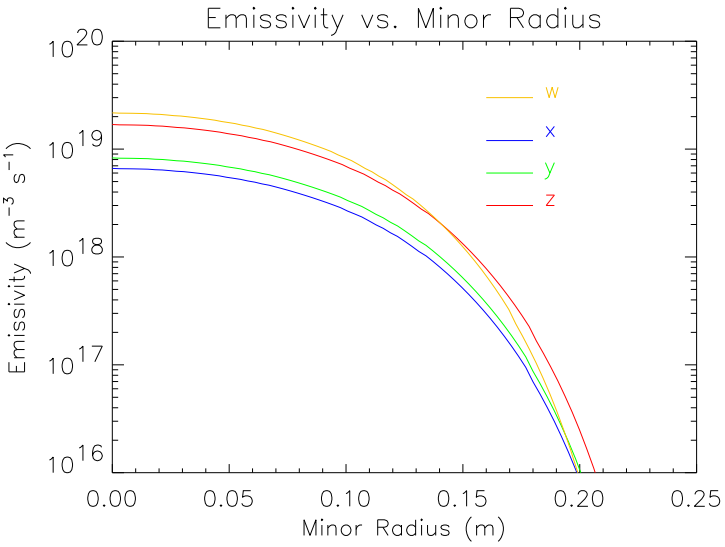

Figure A-1: He–like Ar emissivity profile vs. minor radius, based on the expected line intensities as calculated in this appendix. The figure includes only the four lines **w**, **x**, **y** and **z**.

spectrum.

The emissivity as a function of position along the line of sight for the He–like resonance line, (**w**,) and $L\alpha_1$ from the Lyman alpha doublet for H–like Ar, have been plotted in Fig. A-5. Some simple trigonometry gives a relation for the minor radial value as a function of the line of sight position:

$$r_s = \sqrt{\left(\sqrt{R_0^2 + \ell_s^2} - R_0\right)^2 + d_s^2} \tag{A.10}$$

Where: r_s is the minor radial value, of the distance of tangency point, as a function of the line of sight, (ℓ_s,) for spectrometer $s \in \{\text{C, F, K}\}$. R_0 is the major radius at tangency and d_s is the vertical displacement of the spectrometer s. Minor radius as a function of the line of sight has been plotted in Fig. A-6. Figure A-7 is a plot of the emissivity for the aforementioned lines as a function of minor radius, from this mapping.

Emissivities for the three lines were integrated over their respective lines of sight and used to determine the fraction of photons originating in any given region. The

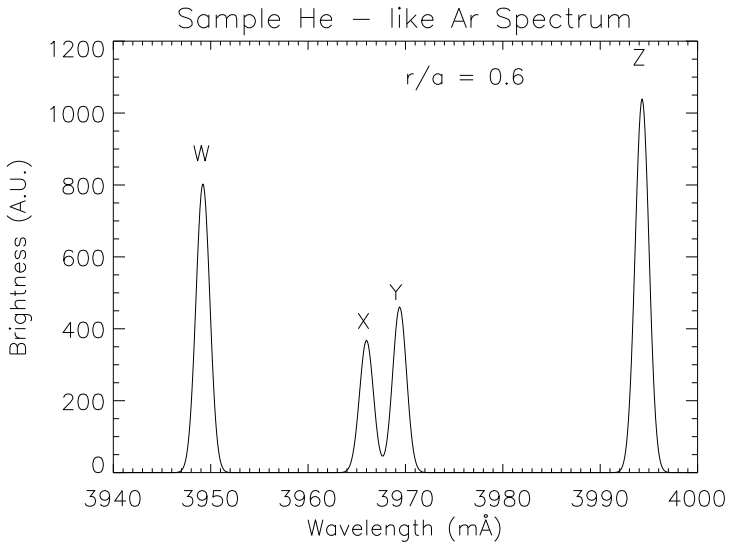

Figure A-2: A He – like Ar spectrum based on the expected line intensities as calculated in this appendix, for the spectrometer viewing at $(r/a) = 0.6$. This spectrum only includes the four lines we have previously mentioned, the **w**, **x**, **y** and **z**.

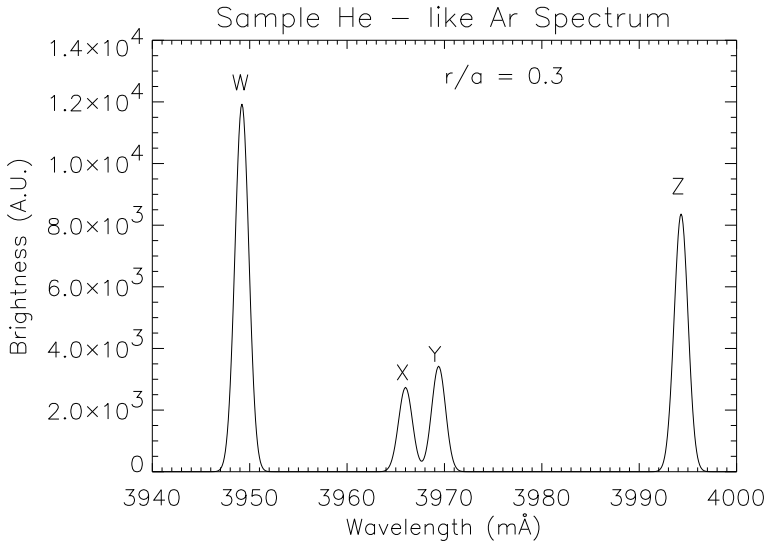

Figure A-3: A He – like Ar spectrum based on the expected line intensities as calculated in this appendix, for the spectrometer viewing at $(r/a) = 0.3$. This spectrum only includes the four lines we have previously mentioned, the **w**, **x**, **y** and **z**.

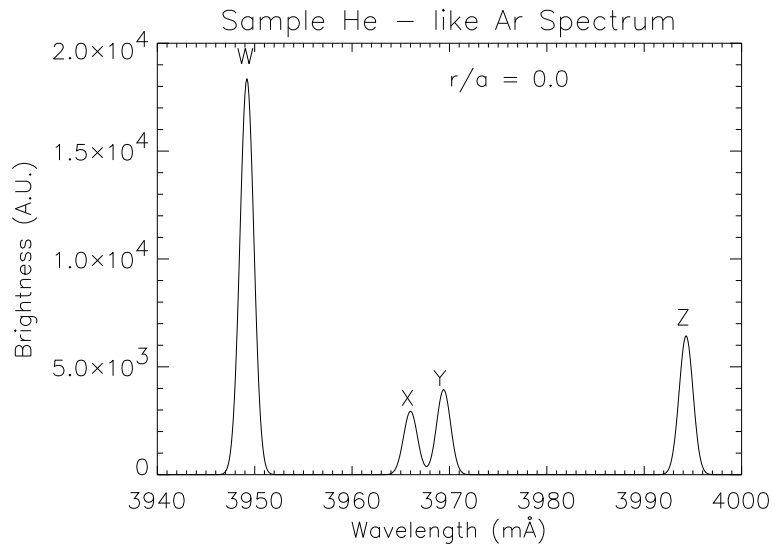

Figure A-4: A He – like Ar spectrum based on the expected line intensities as calculated in this appendix, for a (hypothetical) spectrometer viewing at $(r/a) = 0.0$. This spectrum only includes the four lines we have previously mentioned, the **w**, **x**, **y** and **z**, the satellite lines have not been included in the calculation.

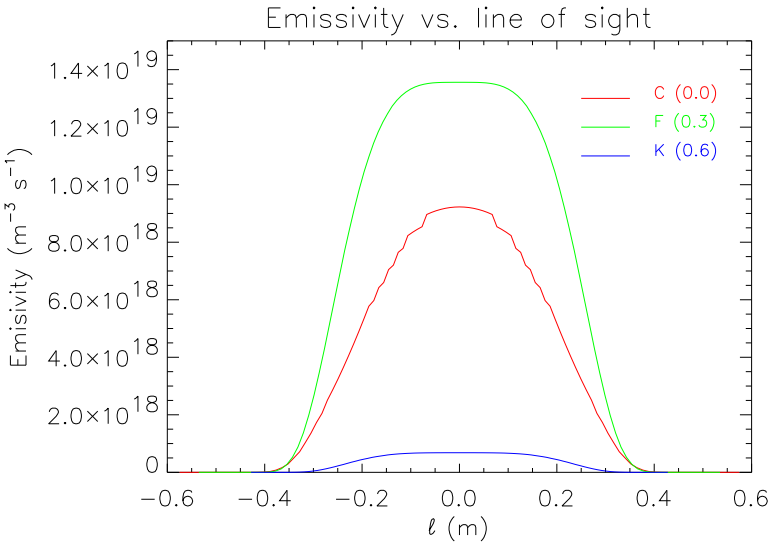

Figure A-5: Emissivity along the line of sight for the three spectrometers. The C–port spectrometer views H–like Ar, the F and K–port spectrometers view He–like Ar, (only the **w** line has been included here.) The zero of the line of sight is the point of minimum radius.

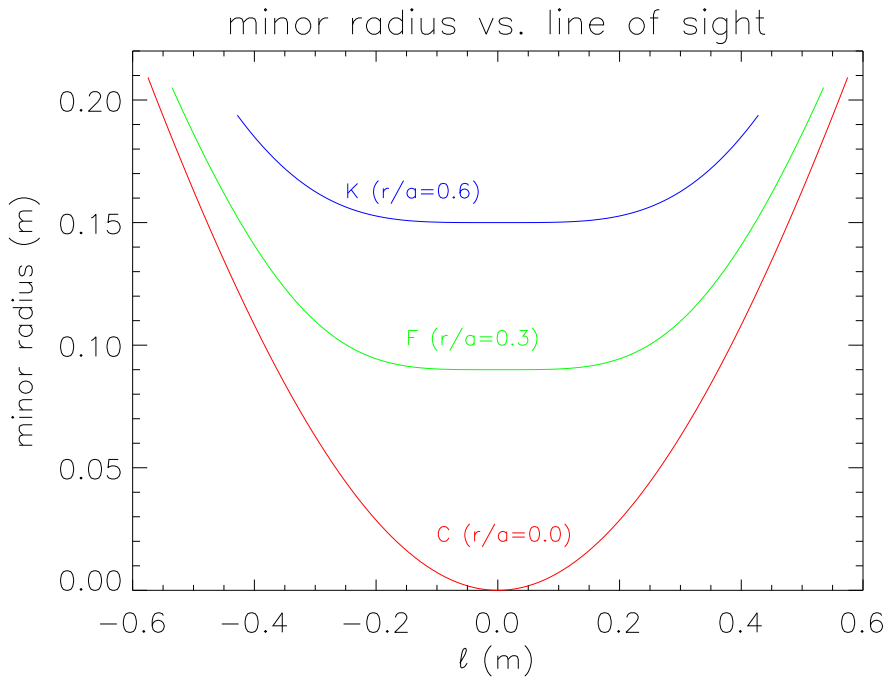

Figure A-6: The mapping from the line of sight to the corresponding minor radius. The minima in these curves correspond to the vertical displacement of the spectrometers, 0.0 *cm*, 9.0 *cm* and 15 *cm* for C, F and K, respectively.

bounding radii of the regions for fractions 0.75, 0.90 and 0.95 are indicated as vertical lines in Fig. A-7, for each of the three spectrometers. For the F–port spectrometer, 0.90 of all photons collected came from a region $\sim 2\ cm$ in width, ($\pm\ 1\ cm$).

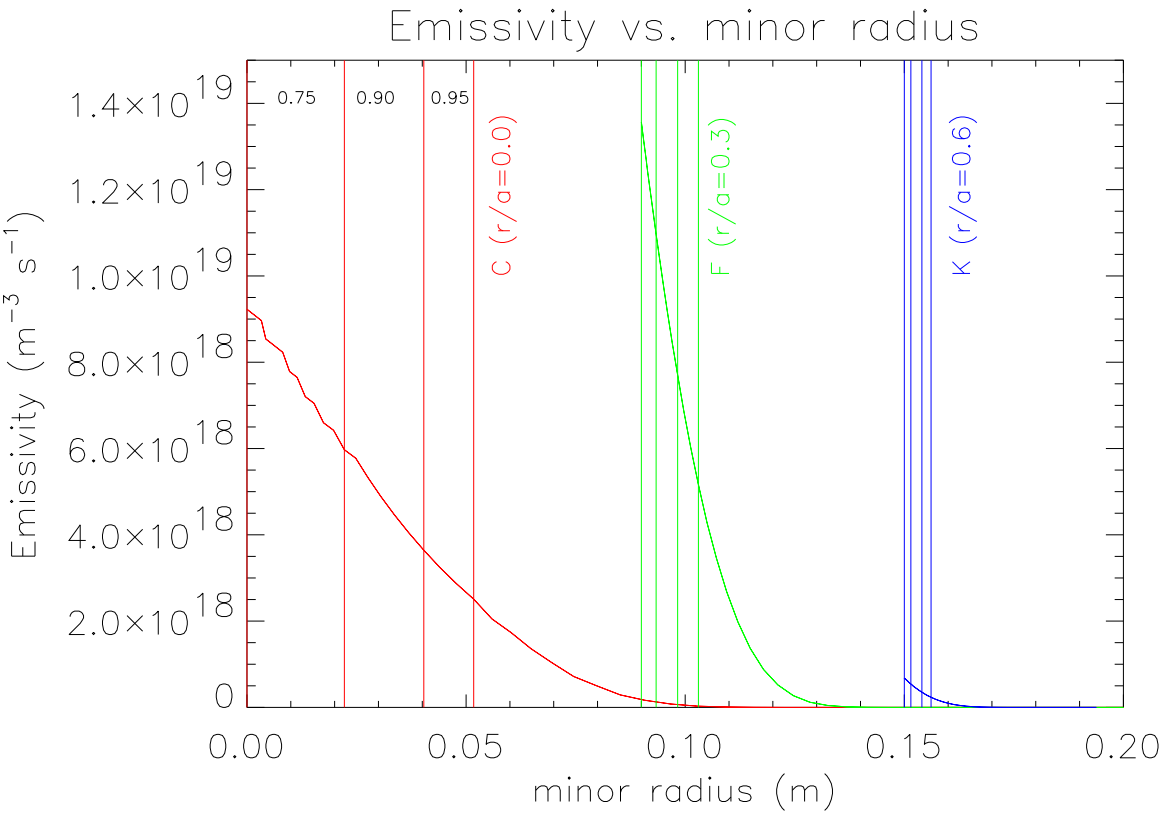

Figure A-7: By folding together the information in the preceding two figures, (Fig. A-5 and Fig. A-6,) the emissivity along the sight line can be mapped from the line of sight to the corresponding minor radial values. The emissivity has been integrated along the line of sight and from this the regions from which 0.75, 0.90 and 0.95 of the photons originate have been calculated. Vertical lines indicate the radii corresponding to the bounds of these regions.

(This page intentionally left blank.)

Appendix B

Rate Coefficients of Dominant Population Mechanisms

The rate coefficients determine the populations and the rate of transitions in and out of various charge states. The calculations in this appendix were performed following those of references [12, 121]. These calculations were made assuming He–like ions. Figure B-1 is an energy level diagram, showing the transitions and population processes of interest here, (also refer to Table A.2).

B.1 Collisional Excitation

The electron impact excitation rate coefficient from ground state g to excited state k, with transition energy E_{gk}, is given in[121], as:

$$S_{gk} = \left(\frac{8kT}{\pi m_e}\right)^{1/2} y^2 \frac{\pi a_0^2 E_H}{w_g E_{gk}} \int_1^\infty \Omega(U) e^{-yU} dU \tag{B.1}$$

evaluating the constants yields:

$$S_{gk} = 8.0 \times 10^{-14} \bar{\Omega}(y) T_e^{-1/2} e^{-y} \qquad (m^3 s^{-1}) \tag{B.2}$$

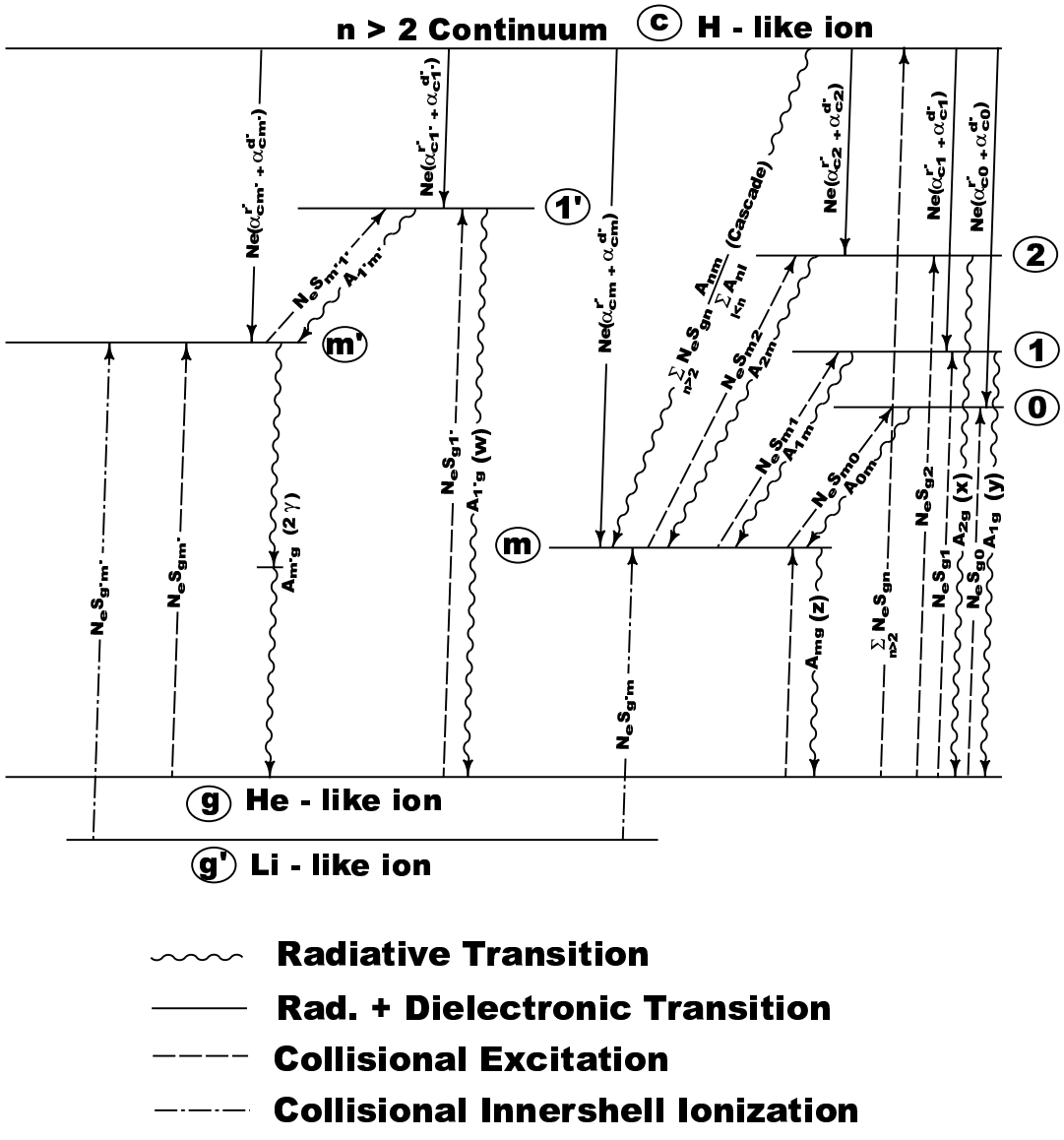

Figure B-1: Population Processes for $n = 2$ level of He–like Ar [121]. The figure includes only those relevant for the four lines **w** ($A_{1'g}$), **x** (A_{2g}), **y** (A_{1g}) and **z** (A_{mg}).

where:

$$\bar{\Omega}(y) = ye^{y}\int_{1}^{\infty}\Omega(U)e^{-yU}dU \tag{B.3}$$

and: y is E_{gk}/T_e; T_e is the electron temperature in eV; a_0 is the Bohr radius; m_e is the rest mass of the electron; E_H is the ionization energy of hydrogen (13.6 eV); w_g is the statistical weight of the initial level; $U = E/E_{gk}$ is the ratio of the energy of the impinging electron to the excitation energy; $\bar{\Omega}(y)$ is the collision strength ($\Omega(y)$) averaged over a Maxwellian distribution.

For principal quantum level 2, the excitation energy, E_{gk} is given as:

$$E_{gk} = \frac{3}{4}\cdot 13.6(Z - a_{gk})^2. \tag{B.4}$$

The screening numbers (a_{gk}) can be found in Table B.1.

$\bar{\Omega}(y)$ can be approximated by[121]:

$$\bar{\Omega}(y) = A + (By + Cy^2 + Dy^3 + E)f(y) + (C + D)y - Dy^2 \tag{B.5}$$

where $f(y)$ is defined as:

$$f(y) = e^{y}E_1(y) \tag{B.6}$$

$E_1(y)$ is the first exponential integral, defined as:

$$E_1(y) = \int_{1}^{\infty} z^{-1}e^{-yz}dz \tag{B.7}$$

$f(y)$ can be approximated, to within about 1 %, by:

$$f(y) = \ln(\frac{y+1}{y}) - \frac{[0.36 + 0.03(y + 0.01)^a]}{(y+1)^2} \tag{B.8}$$

where $a = 1/2$ if $y \geq 1$ and $a = -1/2$ if $y < 1$.

The coefficients A, B, C, D and E are taken from Table 1 in Ref. [123]. They are given in the form $A^* = Z_{gk}^2 A$, $B^* = Z_{gk}^2 B$, $C^* = Z_{gk}^2 C$, $D^* = Z_{gk}^2 D$ and $E^* =$

$Z_{gk}^2 E$. $Z_{gk} = Z - a_{gk}$ is the effective charge number of the ion, for the transition $g \rightarrow k$. (The screening numbers, a_{gk}, for argon are given in Table B.1.)

Element	Z	$a_{gm'}$	$a_{g1'}$	a_{gm}	$a_{g2} = a_{g1} = a_{g0}$
Ar	18	0.498	0.454	0.553	0.496

Table B.1: Screening numbers for excitation from the ground state of He-like Ar ions.

B.2 Cascade Effects

Contributions from higher ($n > 2$) excited levels following excitation from the ground state can occur. When these are taken into account, the total excitation coefficients are:

$$S'_{g1'} = 1.05 S_{g1'} \tag{B.9}$$

$$S'_{gm'} = 1.11 S_{gm'} \tag{B.10}$$

$$S'_{gk} = 1.065 S_{gk}, \qquad k = (0, 1, 2) \tag{B.11}$$

$$S'_{gm'} = S_{gm} + 0.4(S_{g2} + S_{g1} + S_{g0}) e^{-0.16\chi_z/T_e} \tag{B.12}$$

where χ_z is the ionization energy given by:

$$\chi_z = -13.6 \frac{(Z - a_i)^2}{n_z^2} eV \tag{B.13}$$

where: Z is the charge of the ion; n_z is the principal quantum number of the outer electron shell, ($n_z = 1$ for He–like ions); a_i is the effective screening number, ($a_i = 0.593$ for Ar).

B.3 Collisional Excitation and De–Excitation Between n = 2 Excited States

The rate coefficient for the collisional excitation $i \rightarrow k$ is given in Ref. [121] as:

$$S^e_{ik} = 9.28 \times 10^{-13} \frac{[a_{ik} + b_{ik} f(y_{ik})] e^{-y_{ik}}}{\sqrt{T_e}(Z-1)^2} \qquad (m^3 s^{-1}) \qquad \text{(B.14)}$$

where:

$$y_{ik} = \frac{E_{ik}}{T_e} = \frac{8.62 \times 10^{-5} c_{ik}}{T_e}. \qquad \text{(B.15)}$$

The function $f(y_{ik})$ is given by Eq. B.6; T_e is the electron temperature, (eV); E_{ik} is the energy of the transition; and the coefficients a_{ik}, b_{ik} and c_{ik} are given in Table B.2

The expression for the rate coefficients by proton impact excitation and α-particle impact excitation are taken from Ref. [121] as:

$$S^x_{ik} = A_x \exp(-B_x/T_x) S^e_{ik}(T_e = T_x) \qquad \text{(B.16)}$$

where x denotes either p for proton excitation, or α for α-particle excitation; T_p and T_α are the temperatures of the protons and α–particles, respectively. The coefficients A_x and B_x for both protons and α–particles are also listed in Table B.2

Z	$a_{m'1'}$	a_{m2}	a_{m1}	a_{m0}	$b_{m'1'}$	b_{m2}	b_{m1}	b_{m0}
18	4.6	5.7	2.2	-0.04	3.2	1.7	0.96	0.33
Z	$c_{m'1'}$	c_{m2}	c_{m1}	c_{m0}	A_p	B_p/Z	A_α	B_α/Z
18	1.748×10^5	2.567×10^5	2.251×10^5	2.176×10^5	4.80	94.8	3.03	128.9

Table B.2: Parameters for calculation of rate coefficients for collisional transitions between $n = 2$ levels of He–like Ar.

Thus, the total excitation rate is:

$$S_{ik} = S^e_{ik} + \frac{N_p}{N_e} S^p_{ik} + \frac{N_\alpha}{N_e} S^\alpha_{ik}. \tag{B.17}$$

For each of the excitation processes there is a corresponding de-excitation process. The rate coefficient for these processes are given as functions of the excitation rate coefficient:

$$S_{ki} = \left(\frac{w_i}{w_k}\right) S_{ik} \cdot \exp(E_{ik}/T_x) \tag{B.18}$$

where again: $x = e$, p or α; w_i and w_k are the statistical weights of levels i and k respectively; E_{ik} is the transition energy of the $i \rightarrow k$ transition. In Alcator the contributions due to αs and ps are approximately nothing.

B.4 Radiative Transitions

Rate coefficients A_{ik} for spontaneous transitions $i \rightarrow k$ are listed in Table B.3, (Table 7 from [121]).

Z	$A_{m'g}$	$A_{1'g}$	A_{mg}	A_{2g}	A_{1g}	$A_{1'm'}$	A_{2m}	A_{1m}	A_{0m}
18	$4.04{\cdot}10^8$	$1.10{\cdot}10^{14}$	$4.81{\cdot}10^6$	$3.14{\cdot}10^8$	$1.65{\cdot}10^{12}$	$9.50{\cdot}10^7$	$3.41{\cdot}10^8$	$2.66{\cdot}10^8$	$2.43{\cdot}10^8$

Table B.3: Radiative transition probabilities for $n = 2$ levels of He-like Ar. Table 7 from [121].

B.5 Radiative Recombination

The total rate coefficient for radiative recombination to level k is:

$$\alpha^{r'}_{ck} = \alpha^r_{ck} + \Delta\alpha^r_{ck} \tag{B.19}$$

where α^r_{ck} is the direct recombination rate and $\Delta\alpha^r_{ck}$ is the recombination rate by electrons cascading from higher levels ($n > 2$). The expressions for α^r_{ck} and $\Delta\alpha^r_{ck}$ as

given in Ref. [121] are, in units of $(m^3 s^{-1})$:

$$\alpha^r_{cm} = 1.4 \times 10^{-20} \frac{z^{1.8}}{T_e^{0.4}}$$
$$\Delta\alpha^r_{cm} = 3.6 \times 10^{-20} \frac{z^{2.2}}{T_e^{0.6}} \tag{B.20}$$

$$\alpha^r_{ck} = 5.1 \times 10^{-20} \left(\frac{w_k}{9}\right) \frac{z^{2.4}}{T_e^{0.7}}$$
$$\Delta\alpha^r_{ck} = 2.2 \times 10^{-20} \left(\frac{w_k}{9}\right) \frac{z^{2.8}}{T_e^{0.9}} \tag{B.21}$$

$$\alpha^r_{cm'} = 5.0 \times 10^{-21} \frac{z^2}{T_e^{0.5}}$$
$$\frac{\Delta\alpha^r_{cm'}}{\alpha^r_{cm'}} \simeq \frac{\Delta\alpha^r_{cm}}{\alpha^r_{cm}} \tag{B.22}$$

$$\alpha^r_{c1'} = 1.1 \times 10^{-20} \frac{z^{2.52}}{T_e^{0.76}}$$
$$\frac{\Delta\alpha^r_{c1'}}{\alpha^r_{c1'}} \simeq \frac{\Delta\alpha^r_{ck}}{\alpha^r_{ck}} \tag{B.23}$$

where k denotes one of the three P levels $2^3\mathrm{P}_k$. For Ar $w_k = 1$, 3, 5 for $k = 0$, 1, 2 respectively; $z = Z - 1$ and T_e in in eV.

B.6 Dielectronic Recombination

The rate coefficients for dielectronic recombination, for all $n = 2$ levels of He–like Ar, (taken from [121]) are:

$$\alpha^{d'}_{cm} = 5.17 \times 10^{-20} Z^4 T_e^{-3/2} \left[\frac{9}{1 + 7 \times 10^{-5} Z^4} \exp(-6.80(Z + 0.5)^2/T_e) \right.$$
$$\left. + \frac{27}{1 + 8 \times 10^{-5} Z^4} \exp(-8.78 Z^2/T_e) + \frac{380(1+p)^{-1}}{1 + 5 \times 10^{-3} Z^3} \exp(-10.2 Z^2/T_e) \right] \tag{B.24}$$

$$\alpha_{cm'}^{d'} = 5.17 \times 10^{-20} Z^4 T_e^{-3/2} \left[\frac{3}{1 + 3 \times 10^{-6} Z^4} \exp(-6.80(Z+0.5)^2/T_e) \right.$$

$$\left. + \frac{0.5}{1 + 2.2 \times 10^{-5} Z^4} \exp(-8.78 Z^2/T_e) + \frac{6.3}{1 + 5 \times 10^{-3} Z^3} \exp(-10.2 Z^2/T_e) \right] \tag{B.25}$$

$$\alpha_{ck}^{d'} = 5.17 \times 10^{-20} \left(\frac{w_k}{9} \right) Z^4 T_e^{-3/2} \left[\frac{18}{9.5} \exp(-6.80(Z+0.5)^2/T_e) \right.$$

$$\left. + \frac{54}{1 + 1.9 \times 10^{-4} Z^4} \exp(-8.78 Z^2/T_e) + \frac{380}{1 + 5 \times 10^{-3} Z^3} \frac{p}{1+p} \exp(-10.2 Z^2/T_e) \right] \tag{B.26}$$

$$\alpha_{c1'}^{d'} = 5.17 \times 10^{-20} Z^4 T_e^{-3/2} \left[\frac{12}{1 + 6 \times 10^{-6} Z^4} \exp(-6.80(Z+0.5)^2/T_e) \right.$$

$$\left. + \frac{18}{1 + 3 \times 10^{-5} Z^4} \exp(-8.78 Z^2/T_e) + \frac{69}{1 + 5 \times 10^{-3} Z^3} \exp(-10.2 Z^2/T_e) \right] \tag{B.27}$$

where: w_k is the statistical weight of the $2p$ triplet levels; and:

$$p \simeq 2.0 (Z-1)^{0.6} T_e^{-0.3}. \tag{B.28}$$

Appendix C

Calculation of the Fractional Abundance of Argon Charge States in Coronal Equilibrium

The basic assumptions of coronal equilibrium are: that all bound electrons are in the lowest energy state, all upward transitions are collisional ionizations, all downward transitions are radiative recombinations, and further, that these two transition processes balance each other. In the core of a tokamak, these assumptions describe the situation quite well, if transport effects are ignored. Ignoring transport effects is acceptable in H–mode, but not always in L–mode.

C.1 Coronal Equilibrium

To start, assume that Ar^{13+} is the lowest ionization stage[1]. If the plasma is in a state of ionization equilibrium, the fractional abundance does not vary with time, *i.e.*

$$\frac{1}{n_e}\frac{dn_z}{dt} = n_{z-1}S_{z-1} - n_z(S_z + \alpha_z) + n_{z+1}\alpha_{z+1} = 0 \qquad \text{(C.1)}$$

[1]This assumption will be shown to be sufficient later on in this appendix.

$$\Rightarrow n_z(S_z + \alpha_z) = n_{z-1}S_{z-1} + n_{z+1}\alpha_{z+1} \tag{C.2}$$

where $z = Z - i$, n_z is the density of the zth charge state, S_z is the ionization rate for the zth charge state, and α_z is the recombination rate for the zth charge state. For Ar ($Z = 18$), it is assumed that the lowest charge state of Ar in the plasma is Ar^{13+}. Using Eq. C.2 for charge states Ar^{13+} – Ar^{18+}, generates the set of equations:

$$n_{Ar^{18+}}\alpha_{Ar^{18+}} = n_{Ar^{17+}}S_{Ar^{17+}} \tag{C.3}$$

$$n_{Ar^{17+}}\alpha_{Ar^{17+}} + n_{Ar^{17+}}S_{Ar^{17+}} = n_{Ar^{18+}}\alpha_{Ar^{18+}} + n_{Ar^{16+}}S_{Ar^{16+}} \tag{C.4}$$

$$n_{Ar^{16+}}\alpha_{Ar^{16+}} + n_{Ar^{16+}}S_{Ar^{16+}} = n_{Ar^{17+}}\alpha_{Ar^{17+}} + n_{Ar^{15+}}S_{Ar^{15+}} \tag{C.5}$$

$$n_{Ar^{15+}}\alpha_{Ar^{15+}} + n_{Ar^{15+}}S_{Ar^{15+}} = n_{Ar^{16+}}\alpha_{Ar^{16+}} + n_{Ar^{14+}}S_{Ar^{14+}} \tag{C.6}$$

$$n_{Ar^{14+}}\alpha_{Ar^{14+}} + n_{Ar^{14+}}S_{Ar^{14+}} = n_{Ar^{15+}}\alpha_{Ar^{15+}} + n_{Ar^{13+}}S_{Ar^{13+}}. \tag{C.7}$$

The assumption that the lowest charge state is Ar^{13+}, gives the equation:

$$n_{Ar^{18+}} + n_{Ar^{17+}} + n_{Ar^{16+}} + n_{Ar^{15+}} + n_{Ar^{14+}} + n_{Ar^{13+}} = n_{Ar} \tag{C.8}$$

where n_{Ar} is the total density of Ar in the plasma.

This set of equations can then be solved for the fractional abundance ($n_{Ar^{z+}}/n_{Ar}$) of any given charge state of Ar. Copious algebra yields:

$$\frac{n_{Ar^{18+}}}{n_{Ar}} = \frac{1}{A} \tag{C.9}$$

$$\frac{n_{Ar^{17+}}}{n_{Ar}} = \frac{\frac{\alpha_{Ar^{18+}}}{S_{Ar^{17+}}}}{A} \tag{C.10}$$

$$\frac{n_{Ar^{16+}}}{n_{Ar}} = \frac{\frac{\alpha_{Ar^{18+}}\alpha_{Ar^{17+}}}{S_{Ar^{17+}}S_{Ar^{16+}}}}{A} \tag{C.11}$$

$$\frac{n_{Ar^{15+}}}{n_{Ar}} = \frac{\frac{\alpha_{Ar^{18+}}\alpha_{Ar^{17+}}\alpha_{Ar^{16+}}}{S_{Ar^{17+}}S_{Ar^{16+}}S_{Ar^{15+}}}}{A} \tag{C.12}$$

$$\frac{n_{Ar^{14+}}}{n_{Ar}} = \frac{\frac{\alpha_{Ar^{18+}}\alpha_{Ar^{17+}}\alpha_{Ar^{16+}}\alpha_{Ar^{15+}}}{S_{Ar^{17+}}S_{Ar^{16+}}S_{Ar^{15+}}S_{Ar^{14+}}}}{A} \tag{C.13}$$

$$\frac{n_{Ar^{13+}}}{n_{Ar}} = \frac{\frac{\alpha_{Ar^{18+}}\alpha_{Ar^{17+}}\alpha_{Ar^{16+}}\alpha_{Ar^{15+}}\alpha_{Ar^{14+}}}{S_{Ar^{17+}}S_{Ar^{16+}}S_{Ar^{15+}}S_{Ar^{14+}}S_{Ar^{13+}}}}{A} \tag{C.14}$$

where:

$$A = 1 + \frac{\alpha_{Ar^{18+}}}{S_{Ar^{17+}}} + \frac{\alpha_{Ar^{18+}}\alpha_{Ar^{17+}}}{S_{Ar^{17+}}S_{Ar^{16+}}} + \frac{\alpha_{Ar^{18+}}\alpha_{Ar^{17+}}\alpha_{Ar^{16+}}}{S_{Ar^{17+}}S_{Ar^{16+}}S_{Ar^{15+}}} + \frac{\alpha_{Ar^{18+}}\alpha_{Ar^{17+}}\alpha_{Ar^{16+}}\alpha_{Ar^{15+}}}{S_{Ar^{17+}}S_{Ar^{16+}}S_{Ar^{15+}}S_{Ar^{14+}}}$$

$$+\frac{\alpha_{Ar^{18+}}\alpha_{Ar^{17+}}\alpha_{Ar^{16+}}\alpha_{Ar^{15+}}\alpha_{Ar^{14+}}}{S_{Ar^{17+}}S_{Ar^{16+}}S_{Ar^{15+}}S_{Ar^{14+}}S_{Ar^{13+}}}. \tag{C.15}$$

C.2 Ionization Rates

The rate coefficients for ionization by electron impact are given by:

$$S_z = 3.01 \times 10^{-12} T_e^{-1/2} \zeta_z \chi_z^{-1} E_1(x_z) m^3 s^{-1} \tag{C.16}$$

taken from [124] where T_e is the electron temperature in eV; ζ_z is the total number of electrons in the outer shell with principal quantum number n_z; χ_z is given by:

$$\chi_z = 13.6 n_z^{-2} (Z - a_i)^2 eV. \tag{C.17}$$

where the coefficients a_i are listed in Table C.1, taken from [121].

The independent variable of the function $E_1(x_z)$ is:

i	1	2	3	4	5	6
z	17	16	15	14	13	12
ζ_z	1	2	1	2	3	4
n_z	1	1	2	2	2	2
a_i	-0.040	0.593	1.568	2.139	2.908	0.801
χ_z	4426 eV	4121 eV	918 eV	855 eV	774 eV	1006 eV

Table C.1: The screening numbers used in the computation of the ionization coefficients for Ar ($Z = 18$).

$$x_z = \chi_z / T_e = 13.6 n_z^{-2} (Z - a_i)^2 T_e^{-1} \tag{C.18}$$

where, again, T_e is in eV. $E_1(x)$ is the first exponential integral:

$$E_1(x) = \int_1^\infty z^{-1} e^{-xz} dz \tag{C.19}$$

which can be approximated, to within about 1 %, by:

$$E_1(x) = e^{-x} f(x) \tag{C.20}$$

where $f(x)$ is:

$$f(x) = ln(\frac{x+1}{x}) - \frac{[0.36 + 0.03(x + 0.01)^a]}{(x+1)^2} \tag{C.21}$$

where $a = 1/2$ if $x \geq 1$ and $a = -1/2$ if $x < 1$

Fig. C-1 is a plot of S_z as a function of temperature.

C.3 Recombination Rates

The recombination rate, α_z is made up of two parts, the radiative recombination rate (α_z^r) and the dielectronic recombination rate (α_z^d).

$$\alpha_z = \alpha_z^r + \alpha_z^d \tag{C.22}$$

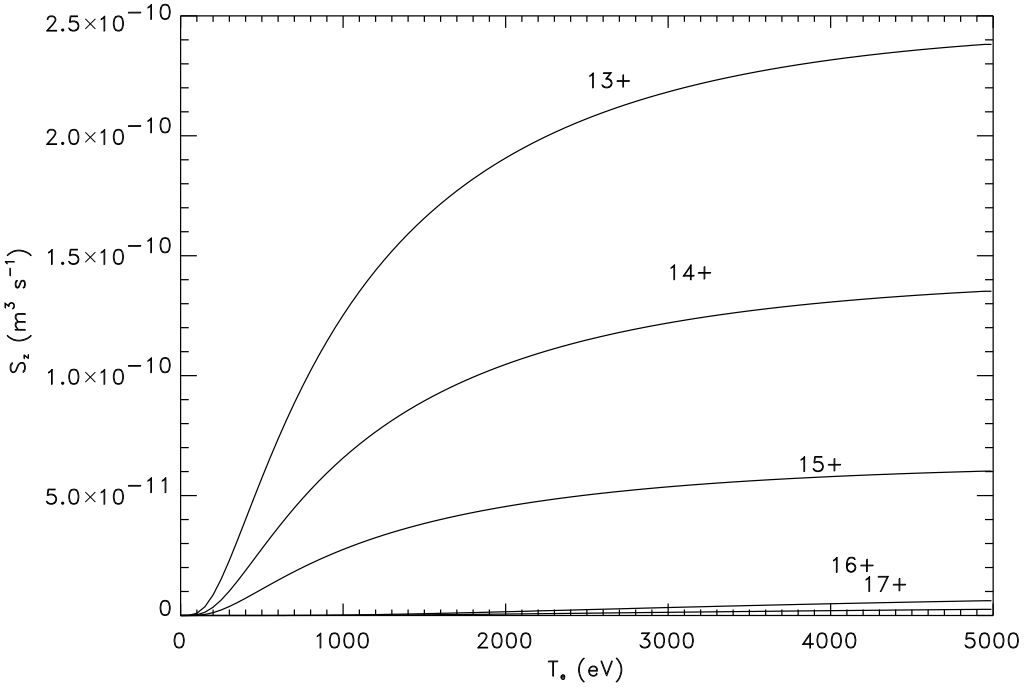

Figure C-1: The electron impact ionization rate (S_z) as a function of temperature, for various charge states of Ar.

The radiative recombination rate has two different regimes: first, for (Z $\rightarrow Z-1$) and ($Z-1 \rightarrow Z-2$) transitions, and second, for ($Z-2 \rightarrow Z-3$), ($Z-3 \rightarrow Z-4$) and ($Z-4 \rightarrow Z-5$) transitions.

For the first regime $z = 18$, 17; the recombination rate given by, (following [125]):

$$\alpha_z^r = 3.85 \times 10^{-19}(Z-i)^{2.4} T_e^{-0.7}. \tag{C.23}$$

For the second regime $z = 16$, 15, 14; the recombination rate is given by, (following [126]):

$$\alpha_z^r = 1.92 \times 10^{-19}(Z-i)^2 n_{z-1}^{-1} x_{z-1} f(x_{z-1}) g_{z-1} \tag{C.24}$$

where: $Z - i = z$ is the charge state, n_z is the principal quantum number of the outer–most electron, x_z is the same as was given in Eq. C.18, $f(x)$ is the same

function as was given in Eq. C.21, and g_z is a numerical factor which accounts for recombination to excited levels given by:

$$g_z \simeq 1 + 0.37 n_z + 0.25 x_z^{0.43} n_z^{1.36}. \tag{C.25}$$

Fig. C-2 is a plot of α_z^r as a function of temperature.

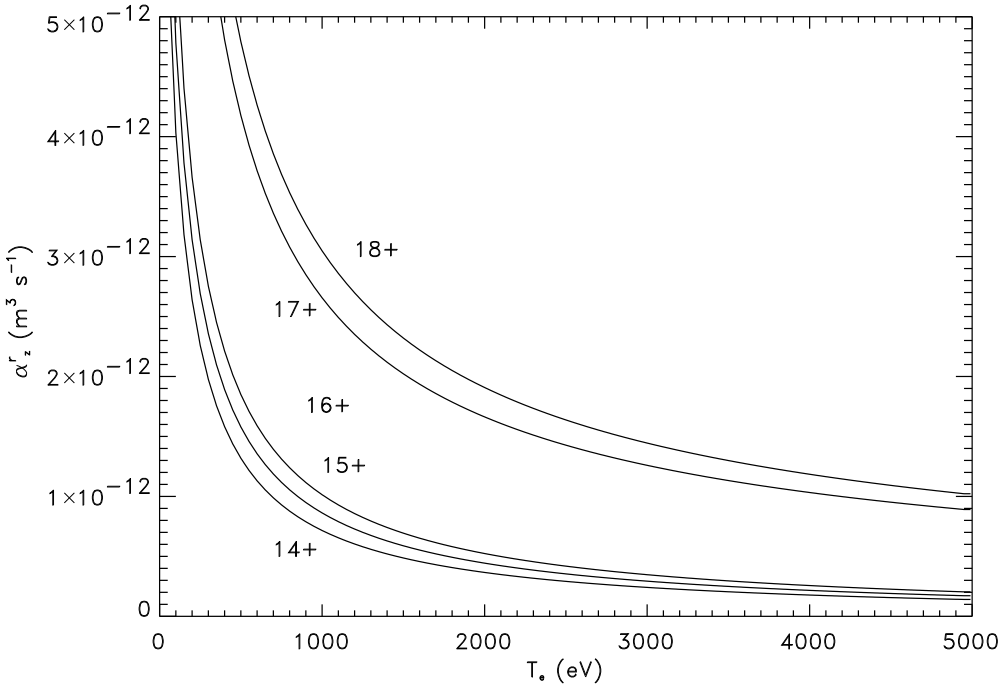

Figure C-2: The radiative recombination rate (α_z^r) as a function of temperature, for various charge states of Ar.

The dielectronic recombination rate is given by the expression, from [121]:

$$\alpha_z^d = 7.99 \times 10^{-16} T_e^{-3/2} \sum_{i=1,2} \alpha_i Z^{\beta_i} \exp[-0.86 \gamma_i z^{\delta_i} / T_e] \tag{C.26}$$

where the coefficients $\alpha_i, \beta_i, \gamma_i$ and δ_i are listed in Table C.2, taken from [121]. The rate coefficients $\alpha_{18}^d \equiv 0$. In Fig. C-3 α_z^d is plotted as a function of temperature.

Finally, Figs. C-4 and C-5 are plots of the fractional abundances as a function of electron temperature, linear and log–log scales respectively. In C-Mod temperatures

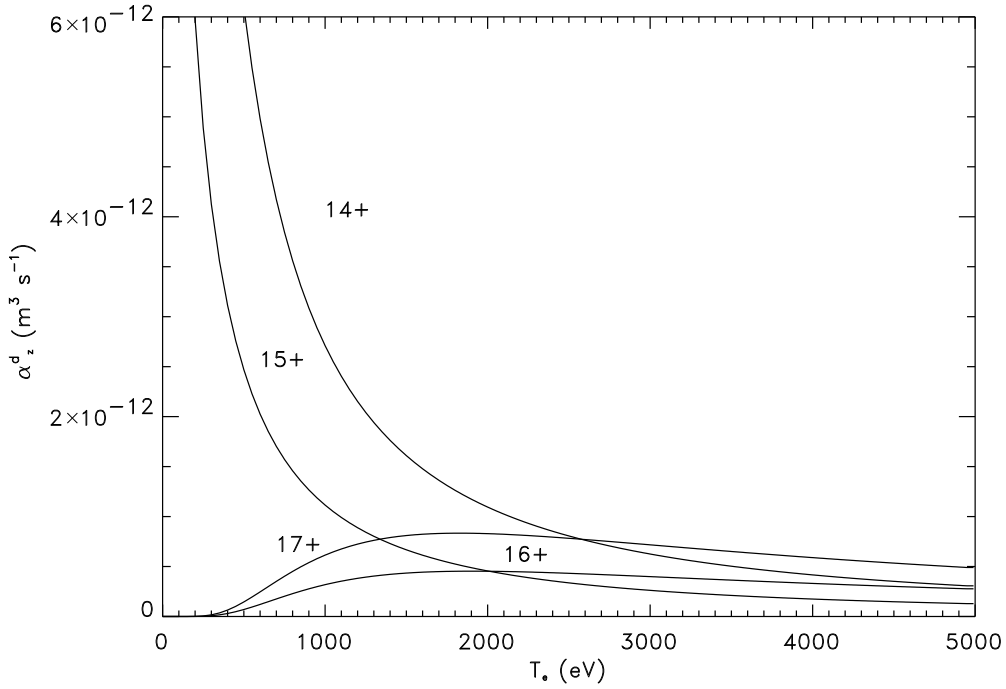

Figure C-3: The dielectronic recombination rate (α_z^d) as a function of temperature, for various charge states of Ar.

below about 500 eV correspond to the edge of the plasma. Hence, neglecting all the charge states below Ar^{13+} in the calculation of the fractional abundances of the Ar in the plasma was justified.

It should be noted that during H–mode, the impurity confinement time is long, thus the Ar has a chance to reach both thermal equilibrium with the surrounding bulk ion species and ionizational equilibrium. However, during L–mode the impurity confinement time is often short, in this case the Ar does not always have time to reach

z	α_1	β_1	γ_1	δ_1	α_2	β_2	γ_2	δ_2
Z - 1	0.32	2.183	35	1.652	0.82	2.272	30	1.643
Z - 2	10.5	0.963	45	1.584	16	1.216	37	1.591
Z - 3	0.8	2.362	6.8	1.625	1.5	1.03	3.5	0.795
Z - 4	6.0	1.807	7.8	1.597	5.8	0.975	8.7	0.685

Table C.2: The dielectronic recombination rate parameters for Ar, for Eq. C.26.

ionization equilibrium before being transported somewhere else in the plasma. This can lead to Ar ionization states that are inconsistent with the predictions of coronal equilibrium. Were we to use this spectrometer array to measure plasma parameters radially further out these effects could play a significant role. However for our regions of interest this is not a concern.

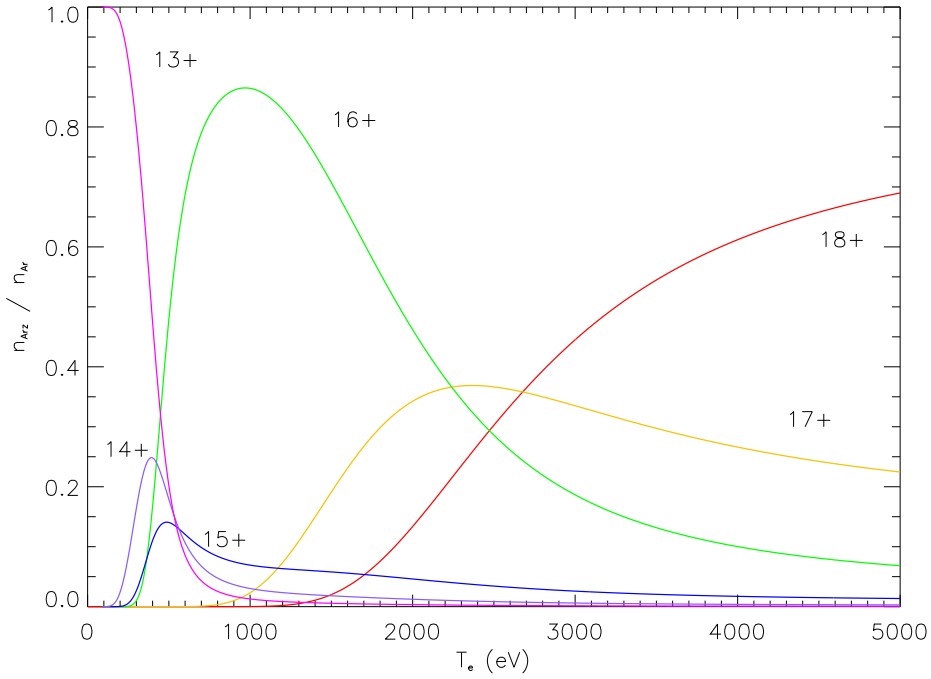

Figure C-4: The fractional abundance of various Ar charge states as a function of temperature. Notice above about 500 eV $\sim$ all the Ar ions are stripped to Ar^{14+} or higher.

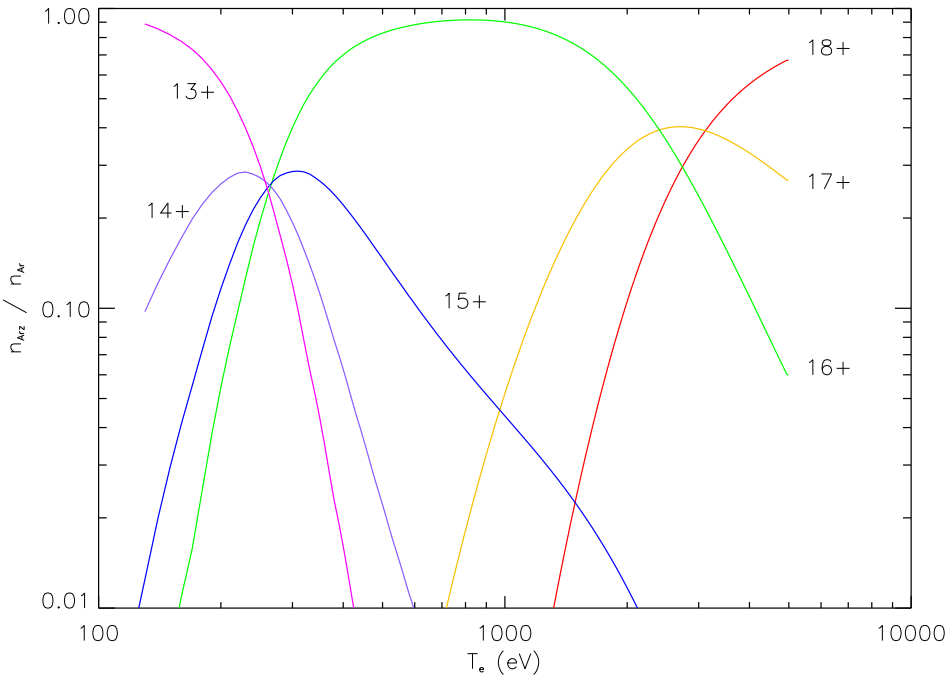

Figure C-5: The fractional abundance of various Ar charge states as a function of temperature, log – log plot. This is the same information as C-4.

(This page not intentionally left blank.)

Appendix D

X–Ray Attenuation

Data pertaining to the attenuation of x–rays in air and in Be will be presented in this Appendix. The fraction of incident photons that makes it through a material with mass attenuation coefficient μ_i is given as:

$$\frac{I}{I_0} = e^{-\mu_i \rho d} \tag{D.1}$$

I the photons count after traveling distance d, I_0 the incident photon count and ρ the material density.

There are three different processes that dominate the attenuation in three different regions. In the low energy region, attenuation is dominated by the photo electric effect, the middle energy region, is dominated by Compton scattering and the high energy region is dominated by pair creation. The total linear mass attenuation coefficient μ_i for any given material is the sum of attenuation by these three processes[127, 128].

D.1 Attenuation in Air

The attenuation of incident x–rays due to the air gap and the finite pressure in the spectrometer is negligible. A plot of the mass attenuation coefficient (μ_{Air}) vs. energy has been reproduced here (Fig. D-1), to justify this assumption. Table D.1 lists the

wavelengths and energies of the relevant lines of He–like Ar for reference.

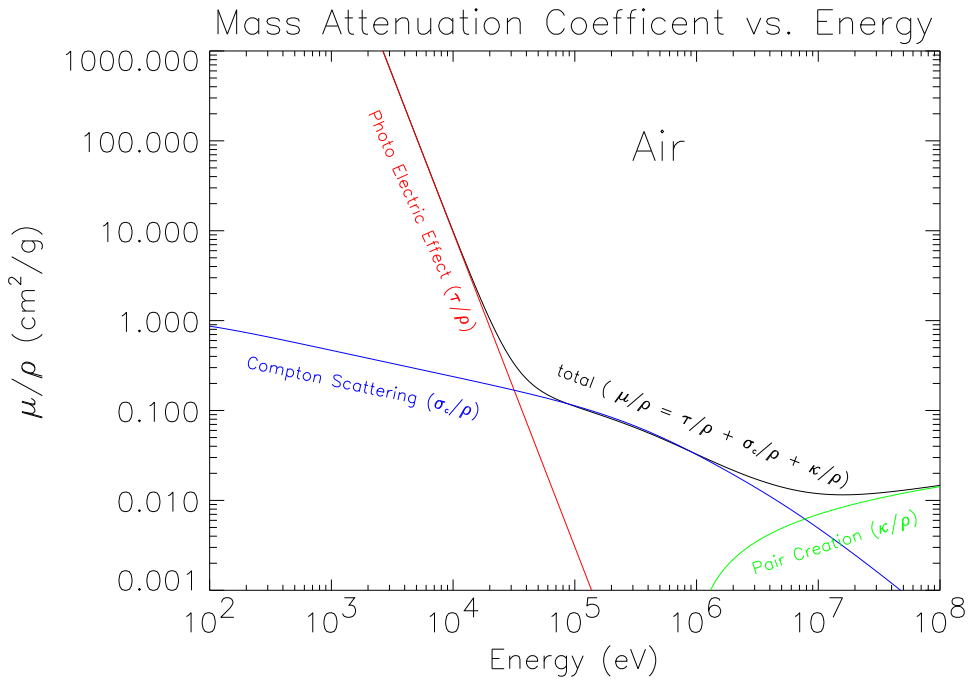

Figure D-1: A plot of the mass attenuation coefficient of air (μ_{Air}) as a function of energy. The region of interest for x–ray photons in this thesis is the low energy end, dominated by the photo electric effect. Table D.1 lists the energies of the four previously mentioned Ar^{16+} lines **w**, **x**, **y** and **z**

Figure D-2 shows x–ray attenuation vs. pressure in air. The air gap (760 Torr) between the spectrometer and the machine is about 1 cm, this attenuates less than 20 % of all incident photons. The arms of the spectrometers pumped out to pressures of order 100 mTorr. The attenuation in the arms is insignificant.

D.2 Attenuation in Be

For completeness we have also included the mass attenuation coefficient of Be (μ_{Be}) as a function of energy (Fig. D-3). The Be windows are so thin (0.002 in) that even if the attenuation per unit length was significant, the attenuation would not amount to much, (< 0.003). Beryllium has one of the smallest x–ray attenuation coefficients

line	λ_0 (mÅ)	Energy (keV)	
w	3949.2	4.1122	resonance line
x	3966.0	4.0948	intercombination line
y	3969.4	4.0913	intercombination line
z	3994.3	4.0658	forbidden line

Table D.1: The transitions of interest for He–like Ar, in these measurements. The energy range for these lines is 4.0 – 4.2 keV.

of any material[95]. This is one more reason why it is so great for UHV and x–ray windows.

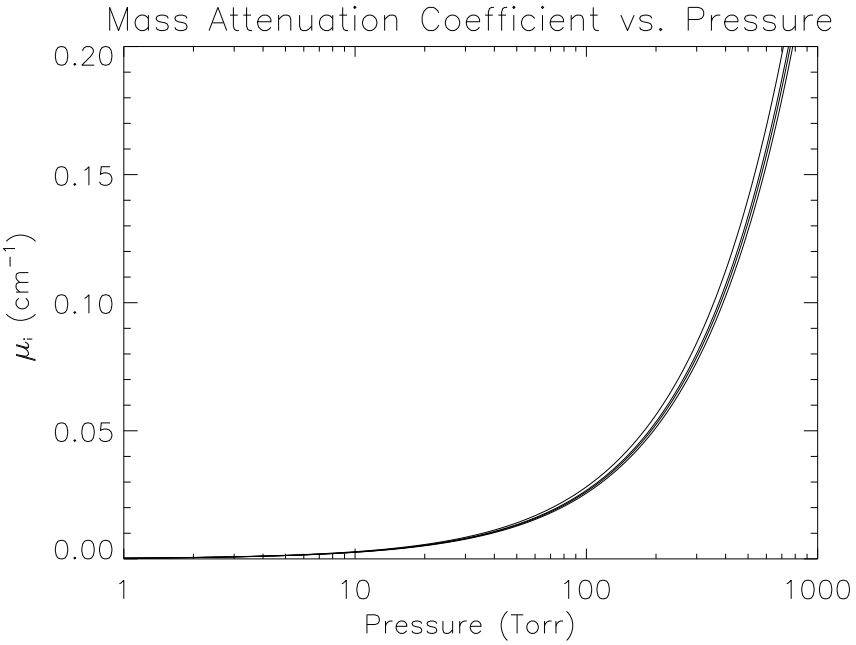

Figure D-2: A plot of the mass attenuation coefficient per unit length (cm), the exponent of Eq. D.1. This is valid in the spectrometer and the air gap between the Be windows of the spectrometer and the tangential port. Below about 1 Torr the attenuation is approximately nothing.

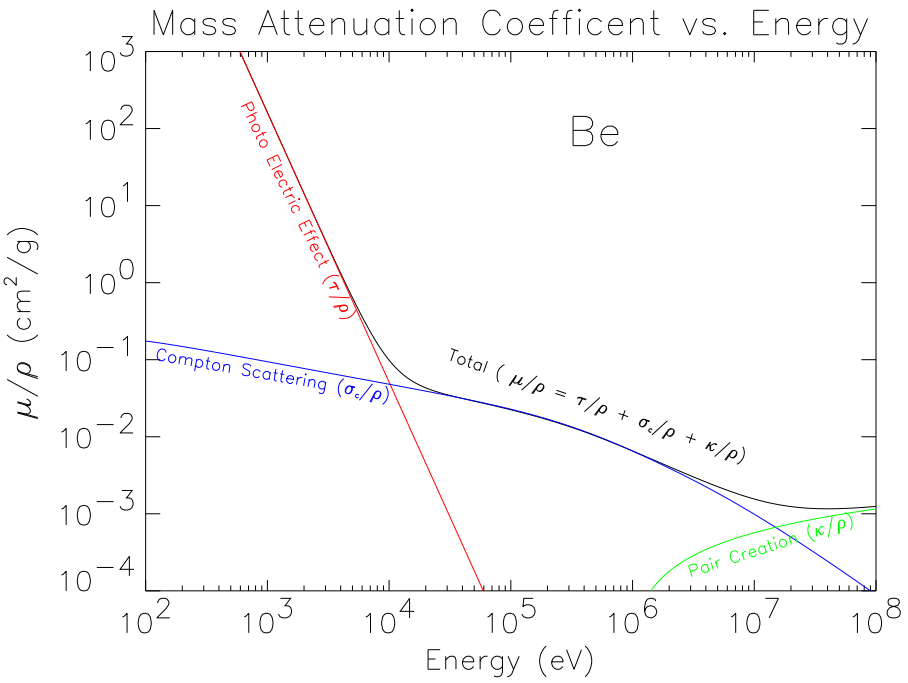

Figure D-3: A plot of the mass attenuation coefficient of Be (μ_{Be}) as a function of incident photon energy.

Bibliography

[1] Hutchinson, I. H. *Physics of Plasmas* **1**, 2753 August (1994).

[2] Burrell, K. H. et al. *H–Mode and VH–Mode Confinement Improvement in DIII–D : Investigation of Turbulance, Local Transport and Active Control of the Shear in the $E \times B$ Flow.* In *Proceedings of the 15^{th} International Confrence, Seville 1994*, number 1, 221 (IAEA, Vienna, 1995).

[3] Fiore, C. L., Rice, J. E., Bonoli, P. T., et al. *Phys. Plasmas* **8**, 2023 (2001).

[4] Wesson, J. *Tokamaks.* Oxford Science Publications, London, (1997).

[5] Freidberg, J. P. *Ideal Magnetohydrodynamics.* Plenum Press, Reading, Massachusetts, (1987).

[6] Chen, F. F. *Introduction to Plasma Physics and Fusion.* Plenum Press, Reading, Massachusetts, (1992).

[7] Greenwald, M. *Fusion Plasmas*, volume 1 of *Wiley Encyclopedia of Electrical and Electronics Engineering*, 45. John Wiley & Sons, Inc., New York (1999).

[8] Hutchinson, I. H. *Principles of Plasma Diagnostics.* Cambridge University Press, London, (1992).

[9] Huddelstone, R. H. and Leonard, S. L., editors. *Plasma Diagnostic Techniques.* Academic Press, New York, New York, (1965).

[10] Auciello, O. and Flamm, D. L., editors. *Plasma Diagnostics.* Two Volumes. Academic Press, Boston, Massachusetts, (1989).

[11] Reardon, J. C. *RF Edge Physics on the Alcator C-Mod Tokamak*. PhD dissertation, Massachusetts Institute of Technology, Department of Physics, June (1999).

[12] Wang, Y. *A Study of Impurity screening in Alcator C-Mod Plasmas*. PhD dissertation, Massachusetts Institute of Technology, Department of Physics, June (1996).

[13] Rost, J. C. *Fast Ion Tails during Radio Frequency Heating on the Alcator C-Mod Tokamak*. PhD dissertation, Massachusetts Institute of Technology, Department of Physics, June (1998).

[14] Hinton, F. L. and Hazeltine, R. D. *Rev. Mod. Phys.* **42**, 239 (1976).

[15] Hirshman, S. P. and Sigmar, D. J. *Nuclear Fusion* **21**, 1079 (1981).

[16] Kim, Y. B., Diamond, P. H., and Groebner, R. J. *Phys. Fluids B* **3**, 2050 (1991).

[17] Rice, J. E. et al. *Nuclear Fusion* **39**, 1175 (1999).

[18] Rogister, A. *Phys. Plasmas* **1**, 619 (1994).

[19] Rogister, A. *Phys. Plasmas* **6**, 200 (1998).

[20] Chang, C. S. et al. *Phys. Plasmas* **6**, 1969 (1999).

[21] Perkins, F. W. et al. In *Controlled Fusion and Plasma Physics (Proc. 27th Eur. Phys. Conf. Budapest, 2000)*, (2001).

[22] White, R. B. and Chance, M. S. *Phys. of Fluids* **27**, 2455 (1984).

[23] White, R. B. *Phys. of Fluids B* **2**, 845 (1990).

[24] Rice, J. E. et al. *Nuclear Fusion* **41**, 277 (2001).

[25] Chang, C. S., Bonoli, P. T., Rice, J. E., and Greenwald, M. J. *Phys. Plasmas* **7**, 1089 (2000).

[26] Hellsten, T. et al. *Self-Consistent Calculations of the Power Deposition and Velocity Distribution During ICRH Including Finite Orbit Widths, Spatial RF-Induced Drift and Diffusion.* In *Proc. 17th Int. Conf. Yokohama, 1998*, 13 (IAEA, Vienna, 1998).

[27] Carlsson, J. et al. in Proc. of Theory of Fusion Plsamas, Varenna, (1994).

[28] Villard, L. et al. *J. Comp. Phys.* **4**, 95 (1986).

[29] Villard, L. et al. *Nuclear Fusion* **35**, 1173 (1995).

[30] Hutchinson, I. H. et al. *Phys. Rev. Letters* **84**(15), 3330 (2000).

[31] Coppi, B. J. *Nuclear Fusion* **42**, 1 (2002).

[32] Coppi, B. J. *Angular Momentum "Generation": Theory and Recent Experiments.* As yet unpublished, (2002).

[33] Shaing, K. *Phys. Rev. Letters* **86**(4), 640 (2001).

[34] Connor, J. W., Fukuda, T., Garbet, X., Gormezano, C., Mukhovatov, V., Wakatani, M., et al. *A Review of Internal Transport Barrier Physics for Steady State opperation of Tokamaks (Version R 16/10/02).* As yet unpublished (submitted to Nuclear Fusion), (2002).

[35] Staebler, G. M. *Reference [8] from [36].*

[36] Staebler, G. M. *Plasma Phys. Control. Fusion* **40**, 569 (1998).

[37] Itoh, S. I. and Itoh, K. *Phys. Rev. Letters* **60**, 2276 (1988).

[38] Shaing, K. and Crume, E. *Phys. Rev. Letters* **63**, 2369 (1989).

[39] Shaing, K. C., Lee, G. S., Carreras, B. A., Houlberg, W. A., and Crume, E. C. *Plasma Physics and Controled Nuclear Fusion Research 1989.* In *Proc. 12th Int. Conf. Nice, 1989*, number 2, 13 (IAEA, Vienna, 1989).

[40] Itoh, S. I., Itoh, K., Fukuyama, A., and Yagi, M. *Phys. Rev. Letters* **72**, 1200 (1994).

[41] Drake, J. F., Lau, Y. T., Guzdar, P. N., Hassam, A. B., Novakovski, S. V., Rodgers, B., and Zeiler, A. *Phys. Rev. Letters* **77**, 494 (1996).

[42] Beer, M. A., Hammett, G. W., Rewoldt, G., Synakowski, E. J., and Zarnstorff, M. C. *Phys. Plasmas* **4**, 1792 (1997).

[43] Bickerton, R. J. et al. *Nature Phys. Science* **229**, 110 (1971).

[44] Ide, S. et al. *Phys. of Plasmas* **7**, 1927 (2000).

[45] Hahm, T. S. and Burrell, K. H. *Phys. of Plasmas* **2**, 1648 (1995).

[46] Biglari, H. et al. *Phys. of Fluids B* **2**, 1 (1990).

[47] Hassam, A. B. *Comments on Plasma Phys. and Controlled Fusion* **14**, 275 (1991).

[48] Kadomtsev, B. B. and Pogutse, O. P. *Zh. Eksp. Teor. Fiz.* **51**, 1172 (1966).

[49] Meagher, J. R. and Markley, H. J. *Practical Analysis of Ultra High Frequency.* RCA Service Company Inc., Camden, New Jersey, (1943).

[50] von Wurmb, B. *The Philosophical Magazine* **1**, 337 (1798).

[51] Rice, J. E., Marmar, E. S., Källne, E., and Källne, J. *Phys. Rev. A* **35**, 3033 (1987).

[52] Rice, J. E. and Marmar, E. S. *Rev. Sci Instrum.* **61**, 2753 (1990).

[53] Rice, J. E. et al. *Nuclear Fusion* **38**, 75 (1998).

[54] Hawkes, N. C. and Peacock, N. J. *Nuclear Fusion* **25**(8), 971 (1985).

[55] Brau, K., Bitter, M., et al. *Nuclear Fusion* **23**(12), 1643 (1983).

[56] Bitter, M. et al. *Physical Review A* **32**(5), 3011 (1985).

[57] Bartiromo, R. et al. *Rev. Sci. Instr.* **60**(2), 237 (1989).

[58] Eriksson, L. G. et al. *Plasma Phys. Control. Fusion* **34**(5), 863 (1992).

[59] Eriksson, L. G. et al. *Plasma Phys. Control. Fusion* **39**, 27 (1997).

[60] Bell, M. G. *Nuclear Fusion* **19**(1), 33 (1979).

[61] Suckewer, S. et al. *Nuclear Fusion* **21**(10), 1301 (1981).

[62] Kostek, C. A. and Marshall, T. C. *Plasma Physics* **25**(4), 421 (1983).

[63] Yamamoto, S. et al. *Transport Studies in the JFT–2 Tokamak*. In *Proceedings of the 9th International Confrence, Baltimore 1983*, number 1, 221 (IAEA, Vienna, 1996).

[64] Bugarya, V. I. et al. *Nuclear Fusion* **25**(12), 1707 (1985).

[65] Isler, R. C. et al. *Phys. Rev. A* **24**, 2701 (1981).

[66] Isler, R. C. and Murray, L. E. *Appl. Phys. Lett.* **42**, 355 (1983).

[67] Groebner, R. J. et al. *Appl. Phys. Letters* **43**, 920 (1983).

[68] Carolan, P. G. et al. *Phys. Rev. A* **35**, 3454 (1987).

[69] Burrell, K. H. et al. *Nuclear Fusion* **28**(1), 3 (1988).

[70] Seraydarian, R. P. et al. *Rev. Sci. Instrum.* **57**, 155 (1985).

[71] Fonck, R. J. et al. *Phys. Rev. A* **29**, 3288 (1984).

[72] Ida, K. and Hidekuma, S. *Rev. Sci. Instr.* **60**(5), 867 (1989).

[73] Isler, R. C. *Phys. Rev. Letters* **38**, 1359 (1977).

[74] Paul, S. F. and Fonck, R. J. *Rev. Sci. Instrum.* **61**(11), 3496 (1990).

[75] Kim, Y. J. et al. *Rev. Sci. Instrum.* **61**(10), 3046 (1990).

[76] Liboff, R. *Introductory Quantum Mechanics*. Addison Wesley Publishing Co., Reading, Ma., (1993).

[77] Bethe, H. A. and Salpeter, E. E. *Quantum Mechanics of One – and Two – Electron Atoms*. Springer, Berlin, (1957).

[78] Burrell, K. H., Lao, L. L., Politzer, P., and West, W. P. *Rev. Sci. Instrum.* **61**(11), 1 (1990).

[79] Burrell, K. H. et al. *Phys. Plasmas* **4**(5), 1499 (1997).

[80] Seraydarian, R. P. and Burrell, K. H. *Rev. Sci. Instrum.* **57**, 2012 (1986).

[81] Wong, S. K. *Phys. of Fluids* **30**, 818 (1987).

[82] Hinton, F. L. and Wong, S. K. *Phys. of Fluids* **28**, 3088 (1985).

[83] Wong, S. K. and Hinton, F. L. *Phys. Rev. Letters* **52**, 827 (1984).

[84] deGrassie, J. S. et al. *Nuc. Fusion* **43**, 142 (2003).

[85] Chan, V. S. et al. *Nucl. Fusion* **40**(6), 1137 (2000).

[86] Weisen, H. et al. *Nuclear Fusion* **29**(12), 2187 (1989).

[87] Scott, S. D. et al. *Phys. Rev. Letters* **64**(5), 531 (1990).

[88] Kallenbach, A. et al. *Plasma Phys. Control. Fusion* **33**(6), 595 (1991).

[89] Koide, Y. et al. *Spontaneous Plasma Rotation of Near–Perpendicular Neutral Beam Injectionand Lower Hybrid Current Drive Plasmas in JT–60U.* In *Proceedings of the 14th International Confrence, Wŭrzburg, 1992*, number 1, 777 (IAEA, Vienna, 1993).

[90] Nagashima, K., Koide, Y., and Shirai, H. *Nuclear Fusion* **34**(3), 449 (1994).

[91] Asakura, N., Fonck, R. J., Jaehnig, K. P., Kaye, S. M., LeBlanc, B., and Okabayshi, M. *Nuclear Fusion* **33**(8), 1165 (1993).

[92] Isler, R. C. et al. *Nuclear Fusion* **26**(4), 391 (1986).

[93] von Hámos, L. *Annalen der Physik.* **5**, 716 (1933).

[94] Rice, J. E., Wang, Y., et al. *Rev. Sci Instrum* **66**, 752 (1995).

[95] *Beryllium Literature from Brush Wellman Engineered Materials.* Commercial Publication, (2002).

[96] Paulers, A. and Shchornak, G. Plenum Publishing Corp., (1983).

[97] Källne, E., Källne, J., Marmar, E. S., and Rice, J. E. *Phys. Scr.* **31**, 551 (1985).

[98] Morris, C. L. et al. *Nuc. Instr. Meth.* , 141 (1978).

[99] Lee, D. M. et al. *Nuc. Instr. Meth.* **109**, 421 (1973).

[100] Grove, R. et al. *Nuc. Instr. Meth.* **89**, 257 (1970).

[101] Lao, L. L., John, H. S., Stambaugh, R. D., Kellman, A., and Pfeiffer, W. *Nuclear Fusion* **25**, 1611 (1985).

[102] Lao, L. L., John, H. S., Stambaugh, R. D., and Pfeiffer, W. *Nuclear Fusion* **25**, 1421 (1985).

[103] Lao, L. L., Ferron, J. R., Groebner, R. J., Howl, W., John, H. S., Strait, E. J., and Taylor, T. S. *Nuclear Fusion* **30**, 1035 (1990).

[104] Lao, L. L. and Jensen, T. H. *Nuclear Fusion* **31**, 1909 (1991).

[105] Marmar, E. S. et al. *Phys. Rev. A* **33**(1), 774 (1986).

[106] Horowitz and Hill. *The Art of Electronics.* Plenum Press, Reading, Massachusetts, (1997).

[107] Rice, J. E. et al. *Nuclear Fusion* **37**, 421 (1997).

[108] Rice, J. E. et al. *Phys. of Plasmas* **7**, 1825 (2000).

[109] Logan, J. D. *Applied Partial Differential Equations*. Springer, New York, (1998).

[110] Hutchinson, I. H. Private Exchange of Scathing Memoranda, February (2003).

[111] *http://www.webelements.com/webelements/elements/text/Al*. World Wide Web, (2003).

[112] Bevington, P. R. and Robinson, D. K. *Data Reduction and Error Analysis for the Physical Sciences*. McGraw Hill, New York, (1992).

[113] Takase, Y. et al. *Phys. of Plasmas* **4**(5), 1647 (1997).

[114] Abramowitz, M. and Stegun, I. A. *Handbook of Mathematical Functions*. Dover Publications, New York, New York, (1970).

[115] Fussmann, G. *Nuc. Fusion* **26**(8), 983 (1986).

[116] Seguin, F. H., Petrasso, R., and Marmar, E. S. *Phys. Rev. Letters* **51**(6), 455 (1983).

[117] Granetz, R. S., Hutchinson, I. H., Gerolamo, J., Pina, W., and Tsui, C. *Rev. Sci. Instr.* **61**(10), 2967 (1990).

[118] Catto, P. J. et al. *Phys. of Plasmas* **8**(7), 3334 (2001).

[119] Ernst, D. *Mechanism for Internal Transport Barrier Control in Alcator C-Mod*. APS Presentation, $44th$ meeting of the DPP, November (2002).

[120] *Darin Ernst*. Private Comunication, (2003).

[121] Mewe, R. and Schrijver, J. *Astron. Astrophys.* **65**, 99 (1978).

[122] Mewe, R. *Astron. Astrophys.* **20**, 215 (1972).

[123] Mewe, R., Schrijver, J., and Sylwester, J. *Astron. Astrophys.* **67**, 55 (1980).

[124] Lotz, W. *Z. Phys.* **232**, 101 (1970).

[125] von Elwert, G. *Z. Naturforsch.* **7a**, 432 (1952).

[126] Seaton, M. *Monthly Notices of the Royal Astronomical Society* **119**, 81 (1959).

[127] Crane, K. S. *Introductory Nuclear Physics*. John Wiley and Sons, New York, New York, (1988).

[128] Price, W. J. *Nuclear Radiation Detection*. McGraw-Hill Book Company, New York, New York, (1964).

[129] Jackson, J. D. *Classical Electromagnetics*. John Wiley and Sons, NY, NY, (1975).

[130] Kong, J. A. *Electromagnetic Wave Theory*. EMW Publishing, Cambridge, Massachusetts, (1999).

(This page intentionally left blank.)

Index